

Ludwig-Maximilians-Universität München

**Simulating Galactic Winds
With The NIRVANA Grid Code:
How To Launch Galactic Outflows**



PhD Thesis of the Faculty of Physics
of the Ludwig-Maximilians-Universität München

presented by
Wolfgang von Glasow
from München, Germany

Submitted May 21st, 2012

First evaluator: Dr. habil. Martin G. H. Krause
Second evaluator: Prof. Dr. Andreas M. Burkert

Day of oral defense: July 6th, 2012

*Dedicated to my father,
Friedemann von Glasow,
to whom time was not given
to witness the completion of this work.*

Contents

Abstract	5
1 Preface/Introduction	7
1.1 Observations of galactic winds	7
1.2 Theoretical work on galactic winds	10
1.3 Aim of this work	13
1.4 Units and constants	14
2 Theory	15
2.1 Disc dynamics and external potentials	15
2.1.1 Gravitational instability of rotating systems	16
2.1.2 Jeans instability	20
2.1.3 Rotational velocity	23
2.1.4 Dark matter halo models	28
2.2 Fluid mechanics	30
2.2.1 Basic equations	30
2.2.2 Interstellar shocks	34
2.2.3 The drivers of interstellar shocks	39
3 Methods	45
3.1 Numerical hydrodynamics	45

CONTENTS

3.2	The NIRVANA code	47
3.3	Simulations on the SGI ALTIX computer	47
3.4	Stellar feedback	48
3.4.1	Locally triggered star formation	49
3.4.2	Star formation by the Kennicutt-Schmidt law	50
3.5	Blast wave implementation	51
3.6	Boundary and initial conditions	54
3.7	Basic setup	56
4	Galactic winds with a logarithmic halo density profile	59
4.1	Preconsiderations	59
4.1.1	Multiphase interstellar medium	59
4.1.2	Global kinetic energy	60
4.1.3	Resolution	61
4.2	Setup and initial conditions	61
4.2.1	Halo setup	61
4.2.2	Disc setup	62
4.3	Test models	64
4.3.1	Thermal and kinetic energy injection	64
4.3.2	Kinetic energy injection only	66
4.4	Implications	69
5	Galactic winds with a converging halo density profile	71
5.1	Preconsiderations	71
5.1.1	Resolution	71
5.2	Setup and initial conditions	72
5.2.1	Halo setup	73
5.2.2	Disc setup	75

5.3	Clustering of SN events	76
5.4	The disc density profile	83
5.5	Implications	86
6	Galactic winds in a NFW halo	89
6.1	Preconsiderations	89
6.1.1	Buoyancy of supernova bubbles	90
6.1.2	Resolution	92
6.2	Setup and initial conditions	92
6.2.1	Halo setup	92
6.2.2	Disc setup	95
6.3	Pressure-driven winds	98
6.3.1	Mass outflow	102
6.3.2	Energy outflow	103
6.4	Kinetic energy-driven winds	105
6.5	Buoyancy	109
6.6	Bubble size	110
6.6.1	Star formation	112
6.6.2	Mass and energy flux	114
6.6.3	Halo pressure	114
6.7	Implications	120
7	Discussion	121
7.1	Methodic accuracy	121
7.2	Disc and halo mass	122
7.3	Supernova injection mechanisms	122
7.4	Wind drivers	123
8	Conclusions and outlook	127

CONTENTS

9.1 Global setup conditions and implementations	129
Appendix	129

Abstract

We perform hydrodynamical simulations of a young galactic disc embedded in a hot gaseous halo. We take into account the (static) gravitational potentials due to a dark matter halo, a stellar bulge and a disc of stars and gas. Two different implementations for star formation are compared. These are one approach based on the local Jeans mass, and another by a local Kennicutt-Schmidt law. Supernovae are triggered randomly and have predetermined event sizes of several tens to hundreds. Three different setup configurations of the disc-halo system are tested, while we improve the setup parameters step by step. We further investigate different halo gas pressures and energy injection methods.

Many of our simulated galaxies, but not all, develop bipolar outflows. We characterise the strength of the outflow by mass and energy outflow rates, and investigate the effect of changes to the details of the model. We find that supernovae are more effective if comprised into larger superbubbles. The weight of the halo gas is able to quench galactic outflows. Buoyancy, though having a measurable effect, and clearly helpful to get superbubbles out of the disc, is too weak to drive the wind by itself. Thermal energy is found to be the dominant wind driver in our simulations. Overall, we find rather low mass and energy outflow rates which do not exceed the star formation rate and about ten percent of the energy injection rate, respectively. The latter finding potentially disagrees with observations and might thus point to a missing element in our simulations.

Chapter 1

Preface/Introduction

1.1 Observations of galactic winds

Disc galaxies at high redshifts form hierarcically in the center of dark matter (DM) haloes. These haloes exist in a wide range of masses, however, one would theoretically expect more DM haloes than observed. In addition to this so-called halo occupation, observations reveal a baryon fraction below the cosmic average value, which is commonly known as the “missing baryons”-problem. The largest amount of baryons can be found in haloes within a range of 10^{10} to $10^{12} M_{\odot}$, which leads to the assumption that for lower masses baryonic matter is ejected in significant amounts to prohibit the gas from accumulating and settling into a disc. One mechanism capable of transporting mass from the host galaxy into the intergalactic medium, especially powerful in low-mass galaxies, are galactic winds.

Galactic winds are found in nearby starburst galaxies [for a review see Veilleux, Cecil and Bland-Hawthorn, 2005]. Enhanced star formation in the central areas of galactic discs triggers supernova (SN) explosions of massive stars. This increases the level of internal as well as turbulent energy in these areas. The dynamical equilibrium between the disc and the surrounding hot halo is therefore disturbed, which results in an outflow of the interstellar medium (ISM) perpendicular to the disc.

Phenomenologically, the stars form in clusters. The SN feedback quickly evacuates these sites by forming hot bubbles. The star formation is hence quickly terminated [Förster Schreiber et al., 2003], the bubbles overlap and form the wind. The outflowing ISM forms filaments that are observed in optical emission lines, but also in soft X-rays (Figure 1.1).

At high redshift, Lyman break galaxies (LBG) show Lyman- α absorption, typically



Figure 1.1: Messier 82. *X-ray:* blue; *optical:* green and orange; *infrared:* red. M82 is a nearby starburst galaxy with a galactic wind. The stellar disc is shown here in green, the multiphase outflow is seen in X-ray and other bands. *Source:* Chandra homepage.

blue-shifted with respect to the emission by a few hundred km s^{-1} [Steidel et al., 2003]. Where the line profile is observed with sufficient signal-to-noise, clear shell signatures are detected: The absorption is blue-shifted with respect to systemic tracers, and the re-emission from the receding shell is seen red-shifted by the same velocity [Pettini et al., 2002]. Lyman break galaxies are probably an order of magnitude smaller than the more massive galaxies detected by the Spectroscopic Imaging survey in the Near-infrared with SINFONI (SINS). They form stars dominantly in a steady mode, tens of solar masses per year [Pettini et al., 2001, Shapley et al., 2003]. The shells are unambiguous evidence for galactic winds. They are expected to arise in hot galaxy haloes, when the leading bow shock has a low Mach number. Hence, shells with velocities of a few hundred km s^{-1} are evidence for a hot halo with a temperature of about 10^6 K. For such low Mach number shocks, the post-shock gas cools faster than the pre-shock gas. The under-pressured cold

gas is then compressed in a thin shell. One would expect such shells to be destroyed after a while by surrounding gas streams or the Rayleigh-Taylor (RT) instability:

$$t_{\text{RT}} = 1.5 \text{ Myr} \left(\frac{R}{\text{kpc}} \right)^{3/2} \left(\frac{M_{\text{gal}}}{10^{11} M_{\odot}} \right)^{-1/2}, \quad (1.1)$$

where R is the shell radius and M_{gal} the gravitating mass within that radius. The shell's deceleration is expected to protect small shells ($\simeq 1$ kpc), only. The ubiquity of the absorption lines then points at constant re-formation of the shells. At redshifts above two, galaxies with much higher star formation rates are observed. The SINS-sample [Genzel et al., 2008] contains massive (few $10^{10} M_{\odot}$ gas) disc galaxies. The observed H α emission suggests star formation rates of about a hundred solar masses per year. This massive star formation leads to a high level of turbulence ($\simeq 50 - 80 \text{ km s}^{-1}$), observed via integral field spectroscopy. These gas discs are thick (1 kpc) and might be related to the old stellar disc of the Milky Way. In analogy to the low redshift case, even stronger winds are expected. Similar results have been found by other groups [Law et al., 2007, Bournaud et al., 2008, van Starckenburg et al., 2008, Kassin et al., 2007]. While also mergers may in principle induce high levels of turbulence, these observational results point to a high fraction of relaxed systems yet with a high level of turbulence. Wind shells have been inferred for Ly α blobs [Ohyaama et al., 2003]. Another piece of the puzzle are high redshift radio galaxies. These galaxies show very bright Ly α emission, which make a detection of the receding shell impossible. However, they also show blue-shifted absorption at very similar velocities as in the LBG case [van Ojik et al., 1997, Wilman et al., 2004]. In a careful evaluation of the available models, Krause [2005] has argued for a galactic wind origin of these absorption systems. The main reason against a relation to the jet is that the shell would have to emit strong Ly α , rather than causing absorption, which is not observed. When the jets grow to the scale of the shells, they destroy them via the RT instability. The model predicts therefore a critical scale, which is indeed observed, and determined to 50 kpc [van Ojik et al., 1997]. The model also requires that the starburst episode precedes the jet episode by about 100 Myr, consistent with starburst-AGN delays observed elsewhere [e.g. Davies et al., 2007]. Radio galaxies are the most massive galaxies at their redshift, and hence, their parent population could well be the SINS galaxies described above. The driving power for the radio galaxy wind shells is about one SN per year, requiring a star formation rate of order hundred solar masses per year, which is also consistent with the massive SINS galaxies. Shapiro et al. [2009] observed rapidly star-forming galaxies at $z = 2$, finding a broad high-velocity component with a fitted line width of $\text{FWHM} > 1500 \text{ km s}^{-1}$ or 500 km s^{-1} , dependent

on modelling as a single Gaussian or as broad wings on the $H\alpha$ and $[N II]$ features, respectively. It is argued that if this emission arises due to starburst-driven galactic winds the mass outflow rate should be slightly higher than the SFR. Nevertheless, it yet remains to be clearly determined if the broad line emission is due to galactic winds or the active supermassive black hole in the galactic center. Sharp and Bland-Hawthorn [2010] have observed various different types of driving mechanisms: Starburst-driven winds are found to be delayed by at least 10 Myr after the onset of star formation; Sharp and Bland-Hawthorn [2010] propose a series of events leading to the onset of a wind which is not supposed to occur before large fractions of dense gas clouds have evaporated by UV irradiation. It is further stated that winds can arise due to processes related to the Active Galactic Nucleus (AGN), however, the data currently available do not allow exact statements about the main energy sources responsible for the wind in this case.

1.2 Theoretical work on galactic winds

The centers of nearby starburst galaxies are now reasonably well understood. 3D hydrodynamics simulations reproduced the outflow of the multiphase ISM, observed in emission lines and X-rays [Cooper et al., 2008]. In particular, Cooper et al. [2008, 2009] simulated wind formation in clumpy, nonisotropic discs by continuous energy injection proportional to the gas density. They have shown that the wind is driven by a series of SN bubbles following the path of least resistance in order to flow freely into the halo. Within such a flow, dense clouds within the disc break up by Kelvin-Helmholtz instability and form filaments. On the small scale, wind asymmetries or collimation are likely to arise from an inhomogeneous ISM. In addition, 3D simulations have been performed by Cooper et al. [2009], in which galactic wind interaction with a radiative cloud is further investigated with the aim of specifying possible survival mechanisms of the latter. In contrast to adiabatic clouds, radiative clouds are not destroyed quickly, but rather break up into several dense cloudlets, drawn along by the flow to form filamentary structures. The number of fragments is strongly affected by numerical resolution. Razoumov [2009] studied the multiphase ISM in protogalactic clumps, modelling the formation of winds from the latter while undergoing a starburst. Star formation in their simulations is based on both local density and a Jeans mass criterion. They find that during SF episodes the neutral gas outflows have velocity widths of several 100 km s^{-1} . It is lined out that the outflows are only efficient when clouds colder than $T = 300 \text{ K}$ and denser than $100 M_{\odot} \text{ pc}^3$, are resolved at grid resolution of 12 pc. It is shown that

a 24 pc resolution is necessary for the first signs of multiphase ISM to occur, however, with star formation being suppressed by a series of effects: higher resolution results in an increase of cold, dense star-forming clumps, whereas the density in individual clumps is found to be higher than in models of low resolution. In turn, the high star formation rate results in a larger volume filling factor of hot gas, which ultimately determines the amount of energy provided to the wind.

Energy is injected into the ISM, mainly by SN explosions, as described by Fujita et al. [2009], who modelled the effects of repeated SN explosions driving supershells in the central disc region at a resolution of < 0.2 pc. The shells cool quickly and become RT unstable. Observed wide NaI absorption lines are suggested to arise from these multiple fragmented shells traveling at different velocities. They conclude that the cool gas kinematics seen in NaI absorption can be explained by an energy-driven bubble causing RT instability without invoking further physics. Though, a number of other drivers has been investigated so far; including e.g. starbursts and supersonic turbulence. Nath and Silk [2009] propose a model of starburst-driven galactic outflows that arise due to both radiation and thermal pressure. An expanding shell of gas and dust is assumed to form by radiative pressure from massive stellar populations at first; when the most massive of these stars turn into SNe, a second inner shell of SN ejecta will soon collide with the outer shell resulting in fragmentation of the latter due to RT instability. The remaining fragments are shown to be an explanation for various phenomena observed recently in Lyman break systems. Scannapieco and Brügger [2010] performed 3D AMR simulations of dwarf galaxy outflows driven by supersonic turbulence. The energy from SNe is directly deposited into the large-scale turbulent motion. Shell interactions around individual OB associations lead to the formation of chaotic H α structures, including numerous smaller SN bubbles. Outflows then develop from overlap of a series of the latter, rather than from a single large superbubble. The overpressure within such an overlap region then pushes out its way into the IGM causing a blow-out, where RT instability of the surrounding bubble only plays a minor role.

Energy injection drives turbulence [Wada and Norman, 2007]; much of the turbulent energy is dissipated radiatively within the galaxy [Dubois and Teyssier, 2008], some, in detail unknown fraction is available for "kinematic dissipation". For the latter, two classes of hydrodynamic models are available: a supersonic wind [e.g. Cooper et al., 2008, Dubois and Teyssier, 2008], and a subsonic convection zone [Kritsuk, Plewa and Müller, 2001; Dubois and Teyssier, 2008]. Supersonic winds are headed by bow shocks in the surrounding medium. Whenever the Mach number is only slightly supersonic, the postshock gas may cool first, and form a possibly low metallicity absorption system

[Dyson, Falle and Perry, 1980]. Such a wind shell is typically stabilised against the RT instability by its own deceleration, but for a few kpc only. External events, like a jet impact [Krause, 2005], or a density decline steeper than r^{-2} [Ferrara and Ricotti, 2006], at the latest, will shatter the shell. The fragments can be partly molecular and are likely to form stars [Krause, 2005, and references therein]. The remaining hot gas overtakes the fragments, which may be pulled back into the galaxy. Now another bow shock may form, if the outflow is energetic enough. Otherwise, a convection zone forms [Kritsuk et al., 2001]. The occurrence of a supersonic wind is governed by the ratio of energy injection to mass injection into the system [Gaibler, Camenzind and Krause, 2005]. The latter includes both, mass injection due to inflows and stellar evolution. If the critical value is not reached, a subsonic convection zone may still form. In the galaxy evolution context, this is often called "galactic fountain". The multi-phase turbulence in these convection zones produces additional radiative dissipation. Some energy might be radiated as sound waves. Dissipation of the sound waves heats the surrounding halo. Thus, a convection zone in the galaxy evolution context may be regarded as an antenna, which efficiently extracts energy from the system. All the parts of a galactic convection zone have been well studied in NGC 1275, the central galaxy of the Perseus cluster, where, however, the main power source is likely the active nucleus [Conselice, Gallagher and Wyse, 2001, Fabian et al., 2006, 2008]. No further observations of radiated sound waves apart from the Perseus cluster are known yet, whereas in the latter the sound waves are likely correlated to the active galactic nucleus (AGN) [Conselice et al., 2001]. The existence of galactic outflow-related sound waves in other galaxies is therefore highly speculative, but generally possible. The sound waves within and surrounding the convection zones may well steepen into weak shocks, and also form absorption systems, if the halo is not too hot (i.e. the cooling time is not too long). Dubois and Teyssier [2008] have proposed a wind solution for lower mass galaxies, like LBG's, and a convective solution for more massive systems, like the massive SINS galaxies, if the star formation history is more quiescent. However, this result depends very much on the ratio between mass injection and SN rate. A small system may live with a convective halo, if it manages to sustain higher gas inflow rates. A more massive system may have strong winds, if the inflow is stopped for some time, e.g. triggered by the energetic outburst of an active galactic nucleus.

1.3 Aim of this work

The aim of this project is to simulate the evolution of the disc-halo interaction for high-redshift galaxies with a grid-based hydrodynamics code in 3D. Both wind and convective solutions shall be investigated. We aim to follow the evolution of the systems for several 100 Myr. In contrast to previous work, we propose a systematic parameter study. As initial conditions, we would take realistic forming galaxies from a cosmological hydrodynamics simulation.

This work will in particular address the question how to channel the required amount of energy into a galactic outflow, so that the latter can grow strong enough to escape from the galactic disc. Our work is therefore at the interface between more ISM centred work [e.g. de Avillez and Breitschwerdt, 2004, 2005] and papers that use the effect of winds with described properties in their simulations [e.g. Springel and Hernquist, 2003]. We focus on Lyman break galaxies. Winds in these objects have recently been simulated by Dubois and Teyssier [2008] and Powell et al. [2011]. Dubois and Teyssier [2008] model their galaxies as cooling and collapsing Navarro-Frenk-White (NFW) spheres, and focus on the onset of a galactic wind against the ram pressure of the in-falling halo material. They find that galactic winds arise only in low mass systems with comparatively small ram pressure, whereas larger ones will typically exhibit galactic fountains instead. Powell et al. [2011] study high-redshift galaxies ($z > 9$) which are still in a phase of strong accretion by filamentary inflow of cold matter. They investigate if galactic winds may significantly alter the mass accretion rate of young galaxies in order to inhibit their further growth. They conclude that, though in these violently star-forming systems strong winds will develop, the accretion rate will not be affected, and hence there will be enough gas supply for long-lasting, intense star formation.

However, none of the numerical models made so far succeeded in producing a wind carrying a total energy corresponding to the observations within the order of magnitude. A variety of different prescriptions for the cooling approach have been proposed; e.g. the storage of energy within turbulence, as is used by Scannapieco and Brügger [2010]. Here, we study a situation similar to Dubois and Teyssier [2008]: We study an isolated disc within a low density halo, using a fixed potential with a dark matter component according to Navarro, Frenk and White [1997]. This work primarily aims at a general understanding of the physics behind the development of galactic outflows. We will therefore perform systematic parameter studies while focusing on the injection of energy. One point of our interest is the effect of the size of superbubbles on the wind efficiency. In order to be able to study this, we do not use single SNe like Powell et al. [2011]. Instead, we inject superbubbles with a controlled and systematically varied number of

SNe per bubble.

1.4 Units and constants

As is customary in most astronomical publications, we applied the CGS unit system in this work. Exempt from the latter however are units of length and units of time, if not stated otherwise. The typical length scale found in galactic wind structures and used herein is the kiloparsec ($1 \text{ kpc} = 1000 \text{ pc} = 3.086 \times 10^{21} \text{ cm}$). The typical time scale related to outflow processes is 10^6 years, or one “mega-year” ($1 \text{ Myr} = 3.156 \times 10^{13} \text{ s}$). These units immediately imply a typical velocity of $1 \text{ kpc Myr}^{-1} = 9.8 \times 10^7 \text{ cm s}^{-1}$. Light speed in units of this typical velocity is $c = 307 \text{ kpc Myr}^{-1}$. The Hubble constant used herein is $72 \text{ km s}^{-1} \text{ Mpc}^{-1}$.

Chapter 2

Theory

In this chapter several core concepts of hydrodynamics will be introduced, which form the theoretical foundation of the presented work. In section 2.1 we will give a brief introduction to the dynamics, global and local stability of gaseous discs, and explain different models for DM haloes; both issues constitute the vantage point for our later numerical setup. Section 2.2 briefly reviews the physics of shock fronts, their temporal evolution and their propagation in the ISM. Shock fronts are commonly triggered by supernovae, which are the key ingredient to our later simulations. Section 2.3 comprises the basics to physically describe the evolution of hydrodynamic systems, which will be applied in the simulation code in slightly modified form.

2.1 Disc dynamics and external potentials

To set up a rotating gas disc numerically, and maintain a certain level of stability, we need to understand how stability is defined physically, and what factors contribute to it. The next subsection deals with global disc stability, defined by the Toomre criterion [Toomre, 1964]. Globally unstable discs will evolve structures like e.g. spiral arms, and exhibit a more clumpy density profile. Stability also plays a role on local scales, and can be described by the Jeans criterion. Instability on local scales is responsible for the collapse of molecular clouds and hence star formation, and needs to be understood for the development of our numerical model disc.

2.1.1 Gravitational instability of rotating systems

The uniformly rotating sheet

This summary largely follows the approach of Binney and Tremaine [1987], initially assuming an infinitely thin disc or sheet of zero thickness, constant surface density Σ_0 and constant angular velocity $\vec{\Omega} = \Omega \cdot \hat{e}_z$. The sheet is situated in the x - y -plane and considered uniform in x - and y -direction. Rotational flattening modifies the Poisson equation of the system, which will be given a reservoir of kinetic energy it can tap into to feed unstable modes. Considering the frame to rotate with the unperturbed sheet at $\vec{\Omega}$ in order to simplify our analysis, the continuity equation, Euler equation and Poisson equation read:

$$\frac{\partial \Sigma}{\partial t} + \vec{\nabla} \cdot (\Sigma \vec{v}) = 0, \quad (2.1)$$

$$\frac{\partial \vec{v}}{\partial t} + (\vec{v} \cdot \vec{\nabla}) \vec{v} = -\frac{\vec{\nabla} p}{\Sigma} - \vec{\nabla} \Phi - 2\vec{\Omega} \times \vec{v} + \Omega^2(x\hat{e}_x + y\hat{e}_y), \quad (2.2)$$

$$\nabla^2 \Phi = 4\pi G \Sigma \delta(z), \quad (2.3)$$

with $\delta(z)$ being the Dirac delta function. It is worth noting that equations (2.1) and (2.2) are defined only in the x - y -plane, whereas equation (2.3) needs to hold in three-dimensional space as well. Rewriting $\frac{d\vec{v}}{dt} = \frac{\partial \vec{v}}{\partial t} + (\vec{v} \cdot \vec{\nabla}) \vec{v}$ yields the above Euler equation (2.2) where the next-to-last term is the Coriolis force, and the last term is the centrifugal force.

Let the perturbed potential Φ be of the form

$$\Phi(\vec{x}, t) = \Phi_0(\vec{x}) + \epsilon \Phi_1(\vec{x}, t), \quad (2.4)$$

where $\epsilon \ll 1$. In the absence of perturbation, equation (2.1) has a trivial solution, equation (2.2) reduces to

$$\vec{\nabla} \Phi_0 = \Omega^2(x\hat{e}_x + y\hat{e}_y), \quad (2.5)$$

and equation (2.3) to

$$\nabla^2\Phi_0 = 4\pi G\Sigma_0\delta(z). \quad (2.6)$$

It is assumed that the opposing gravitational force balances the centrifugal force, as described by the ‘‘Jeans swindle’’.

We now assume a small perturbation $\Sigma(x, y, t) = \Sigma_0 + \epsilon\Sigma_1(x, y, t)$, $\vec{v}(x, y, t) = \epsilon\vec{v}_1(x, y, t)$ with $\epsilon \ll 1$. Dropping all terms nonlinear in ϵ , our equations read:

$$\frac{\partial\Sigma_1}{\partial t} + \Sigma_0\vec{\nabla}\vec{v}_1 = 0, \quad (2.7)$$

$$\frac{\partial\vec{v}_1}{\partial t} = -\frac{c_s^2}{\Sigma_0}\vec{\nabla}\Sigma_1 - \vec{\nabla}\Phi_1 - 2\vec{\Omega} \times \vec{v}_1, \quad (2.8)$$

$$\nabla^2\Phi_1 = 4\pi G\Sigma_1\delta(z), \quad (2.9)$$

with c_s being the sonic speed, defined as

$$c_s^2 = \left[\frac{dp(\Sigma)}{d\Sigma} \right]_{\Sigma_0}. \quad (2.10)$$

This set of equations can now be solved by writing $\Sigma_1(x, y, t) = \Sigma_a \cdot \exp[i(\vec{k} \cdot \vec{x} - \omega t)]$, $\vec{v}_1(x, y, t) = (v_{ax}\hat{e}_x + v_{ay}\hat{e}_y) \cdot \exp[i(\vec{k} \cdot \vec{x} - \omega t)]$, and $\Phi_1(x, y, z = 0, t) = \Phi_a \cdot \exp[i(\vec{k} \cdot \vec{x} - \omega t)]$. The x -axis can be chosen parallel to \vec{k} ; if we now consider Poisson’s equation (2.9), we have $\nabla^2\Phi_1 = 0$ for $z \neq 0$, but $\Phi_1(x, y, z = 0, t) = \Phi_a \cdot \exp[i(\vec{k} \cdot \vec{x} - \omega t)]$ when $z = 0$. The only continuous function approaching zero far from the sheet and satisfying both constraints is

$$\Phi_1(x, y, z = 0, t) = \Phi_a \cdot e^{i(\vec{k} \cdot \vec{x} - \omega t) - |kz|}. \quad (2.11)$$

In order to relate Φ_a to Σ_a , equation (2.9) is integrated from $z = -\zeta$ to $z = \zeta$, where ζ is a positive constant; then the limit of the integral is calculated by letting ζ approach zero:

$$\lim_{\zeta \rightarrow 0} \int_{-\zeta}^{\zeta} \frac{\partial^2\Phi_1}{\partial z^2} dz = \left[\lim_{\zeta \rightarrow 0} \frac{\partial\Phi_1}{\partial z} \right]_{-\zeta}^{\zeta} = 4\pi G\Sigma_1 \int_{-\zeta}^{\zeta} \delta(z) dz = 4\pi G\Sigma_1. \quad (2.12)$$

Therefore,

$$-2|k|\Phi_a = 4\pi G\Sigma_a, \quad (2.13)$$

or

$$\Phi_1(x, y, z, t) = -\frac{2\pi G\Sigma_a}{|k|} \cdot \exp\left[i(\vec{k} \cdot \vec{x} - \omega t) - |kz|\right]. \quad (2.14)$$

Inserting the expressions for Σ_1 , v_1 and Φ_1 in equations (2.7), (2.8) and (2.9) yields homogeneous equations in Σ_a , v_{ax} and v_{ay} . Any nontrivial solutions can occur only when

$$\omega^2 = 4\Omega^2 - 2\pi G\Sigma_0|k| + k^2 c_s^2 \quad (2.15)$$

is fulfilled. (2.15) is the dispersion relation for the uniformly rotating sheet, where Ω is its pattern speed. Note that, if the latter is zero, the so-called Toomre criterion (compare below) is not fulfilled. The sheet is now stable if $\omega^2 \geq 0$ and unstable if $\omega^2 < 0$.

We will now investigate the case of a nonrotating sheet. With the above criteria for ω^2 and $\Omega = 0$, (2.15) reads $c_s^2 k^2 - 2\pi G\Sigma_0|k| < 0$ for an unstable sheet. Besides, this would match the Jeans criterion (compare below), meaning that $|k| < k_J = 2\pi G\Sigma_0/c_s^2$, with k_J being the Jeans wavenumber. In other terms, as $\lambda = 2\pi/k$, any non-rotating sheet will be gravitationally unstable at high wavelengths. Though, there is a major difference to the Jeans instability: For an infinite and homogeneous sheet having a sound speed $c_s = 0$, the instability would grow exponentially with $\exp(\gamma t)$. Here, the growth rate of the perturbation would be $\gamma^2 = -\omega^2 = 4\pi G\rho_0$. For a sheet with zero sound speed and zero angular speed, the growth rate would be $\gamma^2 = 2\pi G\Sigma_0|k|$. This further implies that a decreasing perturbation wavelength γ will lead to a more extreme instability. In turn, as $\lambda = 2\pi/|k| \rightarrow 0$, the growth rate γ will rise to infinity.

A violent instability at short wavelengths would still persist if we assumed a rotating sheet. At zero sound speed, the dispersion relation (2.15) demands instability of perturbations with wavenumber $|k| > 2\Omega^2/\pi G\Sigma_0$. Their growth rate would then be $\gamma^2 = -\omega^2 = 2\pi G\Sigma_0|k| - 4\Omega^2$, again being divergent as λ approaches zero, which means that neither pressure nor rotation cannot suppress this phenomenon alone.

However, though rotation and pressure alone fail to stabilize the sheet, respectively, both together can do. The rotating sheet with zero sound speed is unstable at small wavelengths, whereas a nonrotating sheet with a given nonzero sound speed is unstable

at large wavelengths. Under presence of both effects, the right side of (2.15) is quadratic in k , with the minimum of that curve being at $|k| = \pi G \Sigma_0 / c_s^2 = \frac{1}{2} k_J$. As long as the minimum is positive, the sheet will be stable at all wavelengths. The condition for this,

$$\frac{c_s \Omega}{G \Sigma_0} \geq \frac{\pi}{2} = 1.5708, \quad (2.16)$$

is also known as Toomre's stability criterion. A simple physical interpretation to the same has been given by Toomre [1964]:

A circular area of radius ΔR is assumed, at random position within the sheet. Reducing its radius by $1 - \alpha$ with $\alpha \ll 1$ will evoke a pressure perturbation $p_1 \approx \alpha p_0 \approx \alpha c_s^2 \Sigma_0$. The pressure force per unit mass is given by $\vec{F}_p = -\nabla p / \Sigma$, resulting in an additional outward pressure force of order $|\vec{F}_{p1}| \approx \alpha c_s^2 / \Delta R$, where $\vec{F}_p = -\vec{\nabla} p / \Sigma$ is the pressure force per unit mass. The decrease in radius will further give rise to an additional inward gravitation force, $|\vec{F}_{G1}| \approx GM\alpha / (\Delta R)^2$. The sheet is considered stable if $|\vec{F}_{p1}| > |\vec{F}_{G1}|$, and all other perturbing effects are neglected.

For reasons of simplicity, it was assumed in this analysis that the sheet is infinitely thin. However, there are models for three-dimensional structures, e.g. a uniformly rotating isothermal disc, whose vertical structure is given by the equation of state. An analytical calculation of the stability of these systems was made by Goldreich and Lynden-Bell [1965], who found a stability criterion of

$$\frac{c_s \Omega}{G \Sigma_0} \geq 1.06. \quad (2.17)$$

Conclusively, some notable properties of the uniformly rotating sheet can be lined out: On the one hand, we find that cold sheets are highly unstable. On the other hand, a sound speed c_s satisfying the stability criterion (2.16) will be sufficient to stabilize the sheet.

Local stability of differentially rotating discs

From the previous results, a more handy parameter for instability can now be derived. In order to do so, the model needs to be expanded from the uniformly rotating sheet to the more practical case of a differentially rotating disc. For this purpose, we have a look at a particle in an elliptical orbit and allow the frame to rotate at pattern speed Ω . The particle will now, in good approximation, describe an epicycle motion within the

frame, with an epicycle frequency κ .

In particular, the stability criterion for a uniformly rotating sheet is a special case where $\kappa = 2\Omega$. For a differentially rotating disc, it further has to be considered that c_s , κ and Σ are all functions of radius. This in turn implies that any stability parameter is locally determined, and, likewise, is a function of radius.

We investigate the case of a gas disc with differential rotation. The dispersion relation (2.15) can be generalized to

$$\omega^2 = \kappa^2 - 2\pi G\Sigma|k| + k^2 c_s^2. \quad (2.18)$$

In analogy to the situation described above, the disc turns out to be unstable for $\omega^2 < 0$, as the perturbation is growing exponentially due to ω being a nonreal number and the amplitude being $\exp(-i\omega t)$. Thence, the line of neutral stability is

$$\kappa^2 - 2\pi G\Sigma|k| + k^2 c_s^2 = 0. \quad (2.19)$$

Furthermore, stability against all axisymmetric perturbations would require that equation (2.19) has no solution for positive $|k|$ -values. Solving this quadratic equation finally results in a dimensionless stability parameter Q for the gas disc:

$$Q \equiv \frac{c_s \kappa}{\pi G \Sigma} > 1. \quad (2.20)$$

The number Q is known as **Toomre's stability parameter**. It is worth noting here that a very similar criterion for stellar discs can be obtained from (2.20) by simply replacing the sound speed c_s by the stellar velocity dispersion σ_R , and π by 3.36, respectively [Binney and Tremaine, 1987]. The temperature of a disc can generally be measured via Toomre's Q : "Hot" discs show high velocity dispersions resulting in high Q values, whereas "cool" discs with low velocity dispersions are violently unstable as Q approaches zero, as stated previously.

2.1.2 Jeans instability

The second form of instability, which is to be discussed herein, is the Jeans instability, which is based on the consideration that a gravitating homogeneous medium is at equilibrium. Generally, a static equilibrium state for any infinite homogeneous gravitating system can impossibly exist. As this constraint needs to be bypassed, we have to make

use of the so-called “Jeans swindle”, which has been developed in the course of the studies by Jeans [1902]:

Mathematically, the difficulty is that if the density ρ_0 and pressure p_0 of the medium are constant, and the mean velocity $\vec{v}_0 = 0$, Euler’s equation will lead to

$$\vec{\nabla}\Phi_0 = 0, \quad (2.21)$$

whereas Poisson’s equation, however, demands that

$$\nabla^2\Phi_0 = 4\pi G\rho_0. \quad (2.22)$$

Unless the density ρ_0 equals zero, these two requirements are inconsistent. This inconsistency can nevertheless be overcome by the ad-hoc assumption that the unperturbed potential is zero and henceforth Poisson’s equation only describes the relation between the perturbed density and the perturbed potential. The swindle however lacks a formal justification, and its consistency needs to be checked for every single case, respectively, yet it is justified for some applications. Examples can be found in Binney and Tremaine [1987].

Physical basis of the Jeans instability

We consider a sphere of radius r at some point within an infinite homogeneous and motionless fluid of density ρ_0 and pressure p_0 . Compressing the volume V of the sphere to $V(1 - \alpha)$, $\alpha \ll 1$ will trigger a density and pressure perturbation of $\rho_1 \simeq \alpha\rho_0$ and $p_1 \simeq (dp/d\rho)_0\alpha\rho_0 = \alpha c_s^2\rho_0$. The resulting outward pressure force \vec{F}_{p1} , in addition to the already present pressure force per unit mass, $\vec{F}_p = -\vec{\nabla}p/\rho$, is of magnitude $|\vec{F}_{p1}| = |\vec{\nabla}p_1/\rho_0| \simeq p_1/(\rho_0 r) \simeq \alpha c_s^2/r$, with $\vec{\nabla} \rightarrow 1/r$. Simultaneously, the increase in density causes an additional inward gravitational force $\vec{F}_{G1} = -\vec{\nabla}\Phi_1$. Within the order of magnitude, $|\vec{F}_{G1}| \simeq GM\alpha/r^2 \simeq GM\rho_0 r\alpha$. Instability will occur as soon as the net force $\vec{F}_{p1} + \vec{F}_{G1}$ is directed inwards, meaning $|\vec{F}_{G1}| > |\vec{F}_{p1}|$, or, approximately,

$$\boxed{GM\rho_0 r\alpha > \alpha c_s^2/r.} \quad (2.23)$$

Thus, any perturbation with a scale longer than $r \simeq c_s/\sqrt{G\rho_0}$ is unstable.

The Jeans instability for a fluid

Applying the Jeans swindle, the linearised fluid equations [Binney and Tremaine, 1987] at equilibrium state (i.e. $\rho_0 = \text{const}$, $\vec{v}_0 = 0$) transform into

$$\frac{\partial \rho_1}{\partial t} + \rho_0 \vec{\nabla} \cdot \vec{v}_1 = 0 \quad (2.24)$$

$$\frac{\partial \vec{v}_1}{\partial t} = -\vec{\nabla} h_1 - \vec{\nabla} \Phi_1 \quad (2.25)$$

$$\nabla^2 \Phi_1 = 4\pi G \rho_1 \quad (2.26)$$

$$h_1 = c_s^2 \rho_1 / \rho_0. \quad (2.27)$$

By differentiating equation (2.24) by time, calculating the divergence of equation (2.25), and eliminating \vec{v}_1 , Φ_1 and h_1 , the equations above can be reduced to

$$\frac{\partial^2 \rho_1}{\partial t^2} - c_s^2 \nabla^2 \rho_1 - 4\pi G \rho_0 \rho_1 = 0. \quad (2.28)$$

Due to homogeneity, the coefficients of the partial derivatives in equation (2.28) are independent of position and time, e.g. $c_s = \text{const}$. Granted the dispersion relation

$$\omega^2 = c_s^2 k^2 - 4\pi G \rho_0 \quad (2.29)$$

is fulfilled by ω and $k = |\vec{k}|$, a trial solution of the form

$$\rho_1(\vec{x}, t) = C e^{i(\vec{k} \cdot \vec{x} - \omega t)} \quad (2.30)$$

is required to easily solve equation (2.28). Considering a small density ρ_0 or wavelength $\lambda = 2\pi/k$ equation (2.29) reduces to the dispersion relation of a sound wave: $\omega^2 = c_s^2 k^2$. If $\omega^2 < 0$, we obtain solutions which are exponentially growing or decaying. Their time dependence can be expressed by $e^{\pm\gamma t}$, with $\omega^2 = -\gamma^2$. If the solution is growing, the system will be unstable. This is the case if

$$\boxed{k^2 < k_J^2 \equiv \frac{4\pi G \rho_0}{c_s^2}} \quad (2.31)$$

k_J here is called the **Jeans wavenumber** for the fluid. To the latter, the **Jeans length** $\lambda_J = 2\pi/k_J$ is related; it marks the upper boundary for λ if the solution shall be stable. One can further define a **Jeans mass** M_J as the mass which is comprised within a sphere of diameter λ_J :

$$M_J = \frac{4\pi}{3}\rho_0 \left(\frac{1}{2}\lambda_J\right)^3 = \frac{1}{6}\pi\rho_0 \left(\frac{\pi c_s^2}{G\rho_0}\right)^{3/2}. \quad (2.32)$$

Analogically, if this Jeans mass is overgone within the given sphere of diameter λ_J , the solution will be unstable.

The Jeans mass will play a crucial role later on in the presented work. We will introduce two different star formation recipes for use in the numerical models; one of these will be based on a Jeans mass criterion to locally determine the possibility of star formation and hence supernova feedback.

2.1.3 Rotational velocity

The correct calculation of rotational velocities in a galactic disc system is imperative for later simulation setup. Keplerian rotation represents the most fundamental form of orbital motion, which can be applied to any particle orbiting around a considerably larger point mass. However, gas particles within the disc orbit the galactic centre at a velocity which differs from Keplerian orbit velocity in three major aspects: Firstly, we consider the disc mass to be spread out within a cutoff radius R . Particles on circular orbit at a distance $R' < R$ from the centre will feel a centripetal force from the cumulative mass $M_{\text{cum}} = 2\pi \int_0^{R'} \rho r dr$ within R' , modifying Keplerian rotational velocity to

$$\boxed{v_{\text{rot}}(R') = \sqrt{\frac{GM_{\text{cum}}(R')}{R'}}}. \quad (2.33)$$

Furthermore, we need to consider the pressure forces within the gas disc as well as the disc geometry of the gas, which significantly alters the shape of the potential, and hence v_{rot} .

A more detailed prescription for the derivation of the pressure correction term can be obtained from Stahler and Palla [2005]. In hydrostatic equilibrium, the pressure force in

a HI disc balances the vector force per unit mass, $\nabla\Phi_G$, due to the galactic gravitational potential Φ_G :

$$-\frac{1}{\rho_g}\nabla p_g - \nabla\Phi_G = 0 \quad (2.34)$$

where p_g and ρ_g are the pressure and mass density, respectively, of the atomic gas. Granted that $\gamma = 1$, these two quantities are related by

$$p_g = \rho_g\sigma_g^2, \quad (2.35)$$

with σ_g^2 being the internal random motion of the medium. The radial component of equation (2.34) reads

$$\frac{1}{\Sigma_g}\frac{\partial\tilde{p}_g}{\partial R} = -\frac{\partial\Phi_G}{\partial R}. \quad (2.36)$$

with p_g reducing to $\tilde{p}_g = \Sigma_g\sigma_g^2$. All other directions than the radial one, \hat{R} , have been discarded, thus projecting the volume density into the $x - y$ plane. Based on the assumption that the gas disc follows a radially exponential density distribution, as is the case for the bulk of our presented models, \tilde{p}_g can be rewritten as

$$\tilde{p}_g(R) = \Sigma_g(R)\sigma_g^2 = \Sigma_g(0)e^{-R/R_e}\sigma_g^2. \quad (2.37)$$

Assuming a constant σ_g , the derivative can then be calculated to

$$\frac{\partial\tilde{p}_g(R)}{\partial R} = -\frac{\Sigma_g(0)}{R_e}e^{-R/R_e}\sigma_g^2. \quad (2.38)$$

Additionally, equation (2.34) needs to be modified by a centrifugal term, in order to have the gravitational force balance the pressure force as well as the centrifugal force. With a Keplerian potential $\Phi_G(R) = -GM/R$,

$$\frac{v_{\text{rot}}^2}{R} = \frac{GM}{R^2} + \frac{1}{\Sigma_g}\frac{\partial\tilde{p}_g(R)}{\partial R} = \frac{GM}{R^2} - \frac{\sigma_g^2}{R_e}, \quad (2.39)$$

and therefore

$$\boxed{v_{\text{rot}} = \sqrt{\frac{GM}{R} - \frac{\sigma_g^2 R}{R_e}}}, \quad (2.40)$$

which yields a general solution for a Keplerian potential corrected by pressure effects.

Note in the case of equation (2.39) that the potential Φ_G can in fact be of any form, and does not necessarily have to be Keplerian [for a thorough discussion, see Binney and Tremaine, 1987].

To obtain the potential, Laplace's equation needs to be solved in cylindrical coordinates. Presuming axisymmetry of the system,

$$\frac{1}{R} \frac{\partial}{\partial R} \left(R \frac{\partial \Phi}{\partial R} \right) + \frac{\partial^2 \Phi}{\partial z^2} = 0, \quad (2.41)$$

where the disc is infinitely thin in approximation. This equation simplifies to a set of two first-order differential equations by separating the variables:

$$\Phi = J(R)Z(z) \quad (2.42)$$

Thus,

$$\frac{1}{J(R)R} \frac{d}{dR} \left(R \frac{dJ}{dR} \right) = -\frac{1}{Z(z)} \frac{d^2 Z}{dz^2} = -k^2 \quad (2.43)$$

where $k = \text{const.}$ This set is solved via

$$Z(z) = Z_0 e^{-k|z|} J_0(kR) = J_0(kR), \quad (2.44)$$

where $J_0(kR)$ is the 0th-order cylindrical Bessel function and $Z_0 = \text{const.}$ The boundary conditions are constrained by $\Phi \rightarrow 0$ for $z \rightarrow \infty$ or $R \rightarrow \infty$, as well as $\Phi(z=0)$ remaining finite. Therefore, with k chosen randomly,

$$\Phi_k(R, z) = Z_0 e^{-k|z|} J_0(kR) \quad (2.45)$$

is the solution to the Laplace equation. Keep in mind here, that due to the presence of a mass distribution of almost zero thickness, which is axisymmetric and spatially

finite, k may only assume certain values such that the surface mass density of the sheet determines the potential difference between two points just above and just below the sheet. The relation between the mass surface density and the potential difference can be achieved via Gauss' theorem. Integration of Poisson's equation over a small box-shaped volume surrounding the sheet, where \vec{d}^2S is the normal vector on its surface, yields

$$\int \vec{\nabla}^2 \Phi_k d^3x = 4\pi G \int \rho d^3x, \quad (2.46)$$

and so

$$\int \vec{\nabla} \Phi_k d^2S = 4\pi G \int (\rho dz) d^2S. \quad (2.47)$$

When integrating over all surface elements, any elements non-parallel to the sheet will cancel out. Hence, equation (2.47) reduces to

$$\left(\frac{\partial \Phi_+}{\partial z} - \frac{\partial \Phi_-}{\partial z} \right) d^2S = 4\pi G \Sigma_k d^2S, \quad (2.48)$$

where $\Sigma_k = \int \rho dz$ is the previously defined mass surface density. With

$$\frac{\partial \Phi_{\pm}}{\partial z} = \lim_{z \rightarrow 0} \frac{\partial \Phi_k}{\partial z} = \mp k J_0(kR), \quad (2.49)$$

whereupon z is converging to zero, we obtain the surface density for the solution $\Phi_k(z, R)$,

$$\Sigma_k(R) = -\frac{k}{2\pi G} J_0(kR). \quad (2.50)$$

Further, it is possible to find the potential for any arbitrary very thin mass distribution by exploiting the linearity of Poisson's equation in Φ and ρ . In this case, the general solution reads

$$\Sigma(R) = \int_0^{\infty} S(k) \Sigma_k(R) dk, \quad (2.51)$$

so the potential calculates to

$$\Phi(R, z) = \int_0^{\infty} S(k) \Phi_k(R, z) dk. \quad (2.52)$$

Assuming $\Sigma(R)$ to be given, inserting equation (2.50) into (2.51) yields

$$\Sigma(R) = -\frac{1}{2\pi G} \int_0^{\infty} S(k) J_0(kR) k dk. \quad (2.53)$$

Inversely, since this integral equals a Hankel transformation:

$$S(k) = -2\pi G \int_0^{\infty} J_0(kR) \Sigma(R) R dR. \quad (2.54)$$

The potential Φ and the rotational velocity $v_{\text{rot}}^2 = R \frac{\partial \Phi}{\partial R}$ can now be fixed by applying our postulated exponential profile $\Sigma(R) = \Sigma_0 \cdot \exp(-R/R_e)$, involving the modified Bessel functions I_0, I_1, K_0, K_1 :

$$R \frac{\partial \Phi}{\partial R} = v_{\text{rot}}^2(R) = 4\pi G \Sigma_0 R_e y^2 (I_0(y) K_0(y) - I_1(y) K_1(y)) \quad (2.55)$$

where $y = \frac{1}{2} \frac{R}{R_e}$.

The complete solution regarding pressure forces and the shape of the disc potential now reads

$$v_{\text{rot}} = \left(R \frac{\partial \Phi_{\text{g}}}{\partial R} + R \frac{\partial \Phi_{*}}{\partial R} + R \frac{\partial \Phi_{\text{DM}}}{\partial R} - \frac{\sigma_{\text{g}}^2 R}{R_e} \right)^{1/2}, \quad (2.56)$$

where the negative term is the pressure correction. Note here that the potentials for DM and baryonic matter each have to be calculated separately. Thus,

$$v_{\text{rot}} = \left(4\pi G (\Sigma_{\text{g}}(0) + \Sigma_{*}(0)) R_e y^2 (I_0(y) K_0(y) - I_1(y) K_1(y)) + \frac{G M_{\text{DM,cum}}}{R} - \frac{\sigma_{\text{g}}^2 R}{R_e} \right)^{1/2}, \quad (2.57)$$

while assuming spherical symmetry of the DM halo.

Larger values of gas particle random motion σ_g will generally lead to a faster decline of v_{rot} in the outer disc parts. For low values of σ_g , as is typical in present-day galaxies, the pressure effect is negligible. However, in turbulent, gas-rich proto-galaxies at $z > 2$ the pressure gradient has to be taken into account.

2.1.4 Dark matter halo models

Various prescriptions for DM halo models have been proposed [e.g. Hernquist, 1990, Flynn, Sommer-Larsen and Christensen, 1996, Navarro, Frenk and White, 1996]. In hydrodynamic simulations, all of these can well be applied for a number of specific problems. However, if the typical length scale of the problem is beyond the size of the (baryonic) galaxy hosted by the DM halo, the results may vary significantly for different DM halo models.

Halo model by Flynn, Sommer-Larsen and Christensen [1996]

One of the models, proposed by Flynn et al. [1996], is of major interest due to its simplicity, but also because it is generally adapted to data known from the Milky Way. It describes the potential of the dark halo by invoking a convergence value v_H for the rotational velocity at large radii $r \gg r_0$ comparative to the core radius r_0 . By assuming spherical symmetry, the potential has the form

$$\Phi_{\text{FSC}} = \frac{v_H^2}{2} \ln \left(\left(\frac{r}{\text{kpc}} \right)^2 + \left(\frac{r_0}{\text{kpc}} \right)^2 \right). \quad (2.58)$$

Flynn et al. [1996] assume a convergence value for the rotational velocity $v_H = 220 \text{ km s}^{-1}$ at large radii and a core radius $r_0 = 8.5 \text{ kpc}$ in their model. As a result, the rotational velocity is within a 10 per cent range of v_H at radii larger than $\sim 25 \text{ kpc}$. If the dark halo potential is further modified by both disc and bulge potentials, the change in rotational velocity will be insignificant already at a mere 10 kpc.

We assume that the initial halo gas is in hydrostatic equilibrium, and isothermal, suggesting a radially exponential gas distribution:

$$\rho_g(r, \theta) = \rho_{\text{crit,g}} \exp \left(-\Phi_{\text{tot}}(r, \theta) \frac{0.59 M_{\text{P}}}{k_{\text{B}} T} \right) \quad (2.59)$$

where M_{P} is the proton mass, and

$$\Phi_{\text{tot}}(r, \theta) = \Phi_{\text{disc}}(r, \theta) + \Phi_{\text{cent}}(r) + \Phi_{\text{H}}(r). \quad (2.60)$$

where the dark halo potential will begin to dominate at larger radii. The other two potential components are due to the disc and the central bulge, respectively, and will be explained in Chapter 3. Note that the density in the inner parts of the halo remains within reasonable bounds due to our simulation domain being cut off close to the centre. Since the halo shall be isothermal, we can vary T thus that the density ρ_{g} at the inner edge is no higher than typical disc density values, which are of order $10^{-24} \text{ g cm}^{-3}$. Knowing the resulting temperature T_{halo} , we can obtain the baryonic hot halo mass by integrating the now well-defined baryonic density profile. With the halo density ρ_{g} given for all radii, the halo pressure p can be obtained from the ideal gas equation

$$p = n_{\text{b}} k_{\text{B}} T_{\text{halo}}, \quad (2.61)$$

where $n_{\text{b}} = 2\rho_{\text{g}}/M_{\text{P}}$, due to ionisation. The initial equilibrium state for the halo will only hold as long as the temperature is kept constant.

The task of constructing an isothermal halo in hydrostatic equilibrium is encumbered by the condition that its density should converge against a certain background value as described in 2.1.1. A halo potential of the form described by equation (2.58) given by a constant rotational velocity v_{rot} for large r entails the fact that the halo pressure will not converge. This means first of all that shock fronts could theoretically proceed to infinity as due to the resistant pressure decreasing strongly with r they will accelerate forever. Furthermore, the density would have to drop adequately in order to maintain a constant temperature all over the halo, and would soon reach unreasonable values below the cosmic background (compare Figure 6.2). However, since our simulation boxes do not stretch beyond 20 kpc, these issues may not necessarily be problematic, and the halo model would qualify for simulations within a limited radial range.

Navarro-Frenk-White (NFW) halo

A more common cold dark matter halo model has been provided by Navarro et al. [1996]. They describe the equilibrium dark matter density profile by the well-known equation

$$\rho(r) = \rho_{\text{crit}} \frac{\delta_0}{\left(\frac{r}{r_{\text{s}}}\right) \left(1 + \frac{r}{r_{\text{s}}}\right)^2}, \quad (2.62)$$

where r_s is a scale radius, δ_0 is a characteristic overdensity, and ρ_{crit} is the critical background density. They conclude in their work that the profile can be fitted to haloes of any mass without free shape parameters, however, the profile is shallower than isothermal in the inner regions, and steeper than isothermal in the outer ones. Commonly, the rotation curve resulting from this halo model is in good agreement to the observed rotation curves of disc galaxies.

The NFW model for cold dark matter haloes has been used by Hayashi et al. [2007] to derive the shape of its potential,

$$\Phi_{\text{NFW}} = -\frac{G M_{200}}{r_s f(c_{200})} \frac{\ln(1 + r/r_s)}{r/r_s}, \quad (2.63)$$

where the function $f(u) = \ln(1 + u) - u/(1 + u)$, and the concentration parameter $c_{200} = r_{200}/r_s$ calculates from the radius r_{200} of a sphere of mean density equal to $200 \rho_{\text{crit}}$. M_{200} is the total mass enclosed in this sphere.

We will address these two halo models more closely in the respective setup sections in Chapter 4. Therein we will make use of concrete examples in order to set up the respective simulations, and ultimately line out the most significant differences between the two.

2.2 Fluid mechanics

2.2.1 Basic equations

Fluid and stellar systems often show similar behaviour, and furthermore, gas dynamics are important to understand the formation and evolution of galaxies. For these reasons, the basic principles of fluid mechanics, which are the theoretical foundation for our studies of galaxy dynamics, shall be briefly reviewed here. For a more detailed outline, see Landau and Lifshitz [1959].

Characterising the state of a fluid requires knowledge of its density $\rho(\vec{x}, t)$, its pressure $p(\vec{x}, t)$ and the velocity field $\vec{v}(\vec{x}, t)$. It may further be characterised by functions like the temperature $T(\vec{x}, t)$ and the entropy index $S(\vec{x}, t)$; in the underlying work these

two quantities will be of major importance at a later point. We assume a stationary, closed volume V , with a boundary surface A . It shall contain a fluid of mass $M(t) = \int_V \rho(\vec{x}, t) d^3\vec{x}$, which changes in time by $dM/dt = \int_V (\partial\rho/\partial t) d^3\vec{x}$. A mass of $\rho\vec{v} \cdot d^2\vec{A}$ will cross the area element d^2A per unit time, where $d^2\vec{A}$ is a surface-normal vector pointing outwards, with magnitude d^2A . Hence, $dM/dt = - \int_A \rho\vec{v} \cdot d^2\vec{A}$, so

$$\int_V \frac{\partial\rho}{\partial t} d^3\vec{x} + \int_A \rho\vec{v} \cdot d^2\vec{A} = 0. \quad (2.64)$$

With the divergence theorem,

$$\int_V \left[\frac{\partial\rho}{\partial t} + \vec{\nabla} \cdot (\rho\vec{v}) \right] d^3\vec{x} = 0, \quad (2.65)$$

and keeping in mind that this result is true for every volume, one can derive the **continuity equation**:

$$\frac{\partial\rho}{\partial t} + \vec{\nabla} \cdot (\rho\vec{v}) = 0. \quad (2.66)$$

In an inviscid fluid, the volume is exposed to a total pressure force of $-\int_A p d^2\vec{A}$. If some external force, like the one from a gravitational potential $\Phi(\vec{v}, t)$ applies, Newton's second law reads

$$M \frac{d\vec{v}}{dt} = - \int_A p d^2\vec{A} - M \vec{\nabla} \Phi. \quad (2.67)$$

The latter must hold for every small volume V , and in accordance to the divergence theorem $\int_A p d^2\vec{A} = \int_V \vec{\nabla} p d^3\vec{x}$,

$$\rho \frac{d\vec{v}}{dt} = -\vec{\nabla} p - \rho \vec{\nabla} \Phi. \quad (2.68)$$

Now, $d\vec{v}/dt$ must be related to the velocity field $\vec{v}(\vec{x}t)$. For any given particle, the velocity change $d\vec{v}$ per time interval dt is the sum of the velocity change at a given point in space, $(\partial\vec{v}/\partial t)dt$, and the velocity difference between two points at a separation of $d\vec{x} = \vec{v}dt$ at the same moment. With the latter change being $(\partial\vec{v}/\partial x_i)dx_i = (d\vec{x} \cdot \vec{\nabla})\vec{v}$,

$$\frac{d\vec{v}}{dt} = \frac{\partial\vec{v}}{\partial t} + (\vec{v} \cdot \vec{\nabla})\vec{v}. \quad (2.69)$$

The combination of equations (2.68) and (2.69) leads to **Euler's equation**:

$$\frac{\partial \vec{v}}{\partial t} + (\vec{v} \cdot \vec{\nabla}) \vec{v} = -\frac{1}{\rho} \vec{\nabla} p - \vec{\nabla} \Phi. \quad (2.70)$$

To determine the changes in energy within a given stationary volume, we write the energy of the fluid per unit volume as

$$\frac{\rho v^2}{2} + \rho e_{\text{int}}, \quad (2.71)$$

in which the first term is the kinetic energy, and the second is the internal energy, with e_{int} being the internal energy per unit mass. The change in energy follows from the partial derivative,

$$\frac{\partial}{\partial t} \left(\frac{\rho v^2}{2} + \rho e_{\text{int}} \right). \quad (2.72)$$

For its calculation we write

$$\frac{\partial}{\partial t} \left(\frac{\rho v^2}{2} \right) = \frac{v^2}{2} \frac{\partial \rho}{\partial t} + \rho \vec{v} \frac{\partial \vec{v}}{\partial t}, \quad (2.73)$$

or, using the continuity equation (2.66) and a non-gravitational form of Euler's equation (2.70),

$$\frac{\partial}{\partial t} \left(\frac{\rho v^2}{2} \right) = -\frac{v^2}{2} \nabla \cdot (\rho \vec{v}) - \vec{v} \nabla p - \rho \vec{v} (\vec{v} \nabla) \vec{v}. \quad (2.74)$$

The expression $\vec{v} (\vec{v} \nabla) \vec{v}$ is substituted by $(\vec{v}/2) \nabla v^2$. The pressure gradient can be substituted according to the thermodynamic relation $dw = T ds + (1/\rho) dp$ by $\rho \nabla w - \rho T \nabla s$, thus obtaining

$$\frac{\partial}{\partial t} \left(\frac{\rho v^2}{2} \right) = -\frac{v^2}{2} \nabla \cdot (\rho \vec{v}) - \rho \vec{v} \nabla \left(\frac{v^2}{2} + w \right) + \rho T \vec{v} \nabla s, \quad (2.75)$$

where w is the specific enthalpy, and s the specific entropy. We now use the thermodynamic relation

$$de_{\text{int}} = T ds - p dV = T ds + \frac{p}{\rho^2} d\rho \quad (2.76)$$

to rewrite the derivative $(\partial/\partial t)\rho e_{\text{int}}$. Since the sum of $e_{\text{int}} + (p/\rho) = e_{\text{int}} + pV$ is just the specific enthalpy w , we find

$$d(\rho e_{\text{int}}) = e_{\text{int}} d\rho + \rho de_{\text{int}} = w d\rho + \rho T ds, \quad (2.77)$$

and hence

$$\frac{\partial(\rho e_{\text{int}})}{\partial t} = w \frac{\partial \rho}{\partial t} + \rho T \frac{\partial s}{\partial t} = -w \nabla \cdot (\rho \vec{v}) - \rho T \vec{v} \nabla s. \quad (2.78)$$

Hereby we have invoked the adiabatic equation $(\partial s/\partial t) + \vec{v} \nabla s = 0$. By collecting terms, we obtain the change in energy,

$$\frac{\partial}{\partial t} \left(\frac{\rho v^2}{2} + \rho e_{\text{int}} \right) = - \left(\frac{v^2}{2} + w \right) \nabla \cdot (\rho \vec{v}) - \rho \vec{v} \nabla \left(\frac{v^2}{2} + w \right), \quad (2.79)$$

or, finally,

$$\frac{\partial}{\partial t} \left(\frac{\rho v^2}{2} + \rho e_{\text{int}} \right) = - \nabla \cdot \left(\rho \vec{v} \left(\frac{v^2}{2} + w \right) \right). \quad (2.80)$$

By introducing the sum of specific internal and kinetic energies $e = (v^2/2) + e_{\text{int}}$ as the total specific energy and eliminating w , the **equation of energy conservation** can be written as

$$\frac{\partial \rho e}{\partial t} + \nabla \cdot (\rho e \vec{v}) + \nabla \cdot (p \vec{v}) = 0. \quad (2.81)$$

Lastly, an **equation of state** is needed to bring pressure and density into relation, e.g. $p = p(\rho, s)$ or $p = p(\rho, T)$; these have to be combined with an auxiliary equation, which determines s or T . For fluid systems, it is sufficient to apply the barotropic equation of state, $p = p(\rho)$, where the density uniquely determines the pressure. One may then rewrite the specific enthalpy as

$$w(\rho) = \int_0^{\rho} \frac{dp}{\rho} = \int_0^{\rho} \frac{dp(\rho)}{d\rho} \frac{d\rho}{\rho}, \quad (2.82)$$

with which, in a barotropic fluid, Euler's equation (2.70) simplifies to

$$\frac{\partial \vec{v}}{\partial t} + (\vec{v} \cdot \vec{\nabla}) \vec{v} = -\vec{\nabla} (w + \Phi). \quad (2.83)$$

The models presented in this work however are based on the assumption of an ideal gas, for which the pressure is determined by

$$pV = nk_{\text{B}}T, \quad (2.84)$$

where n is the number density of gas particles, and k_{B} is the Boltzmann constant. It may also be expressed using the adiabatic index γ by writing

$$p = (\gamma - 1)e, \quad (2.85)$$

where e is the energy per unit mass, or specific energy.

The three vector components of Euler's equation, the continuity equation (2.66) and equation (2.81) constitute a complete description for the evolution of pressure p , density ρ , and the three components of the velocity \vec{v} .

2.2.2 Interstellar shocks

We shall now have a closer look at the physics regarding one of the key ingredients in our later simulations. The different types of interstellar shocks and their origin as well as the Rankine-Hugoniot jump condition have been summarised in more detail by Dopita and Sutherland [2003]. Their descriptions also include magnetic fields, which we will widely neglect here, as their incorporation is beyond the scope of this work.

The Rankine-Hugoniot jump condition

A complete description of non-gravitational steady flows can now be provided by the continuity equation (2.66), Euler's equation (2.70), the equation of energy conservation (2.81), and further the magnetic energyflux conservation equation,

$$\frac{d}{dx} (Bv) = 0. \quad (2.86)$$

Their integration yields the relationship between any two regions of the flow. Note that here we are dealing with continuous flows. The standard hydrodynamic equations imply

continuous differentiability of a function. Any flow discontinuities (i.e. shocks) however are non-continuous solutions. These can be found by transforming the equations into the inertial system of the shock wave, so time derivatives will no longer be of relevance. We consider one starting point in the flow, described by the variables v_0 , p_0 , ρ_0 , and magnetic field B_0 , and further one later point in the flow with these variables changed to v_1 , p_1 , ρ_1 , and B_1 , respectively. By eliminating the internal energy term from the energy equation, using $U = p/(\gamma - 1)$ as equation of state, the **Rankine-Hugoniot jump condition** can be written in terms of the difference between the fluid variables at points 0 and 1, respectively,

$$\begin{aligned} [\rho v]_0^1 &= 0, \\ [Bv]_0^1 &= 0, \\ \left[p + \rho v^2 + \frac{B^2}{8\pi} \right]_0^1 &= 0, \\ \left[\frac{\rho v^3}{2} + \frac{\gamma}{\gamma-1} p v + \frac{B^2 v}{4\pi} + F \right]_0^1 &= 0. \end{aligned} \tag{2.87}$$

It is imperative for the flow discontinuity to be stationary in the frame of reference in which the jump conditions are evaluated. These conditions can then be used to obtain the flow variables and magnetic field at any other point in the flow, under the circumstances that the initial conditions are known and the energy loss term is calculable.

In the present work only flows without magnetic fields are investigated. We consider a radiation-free change, where the flow variables change suddenly in the shock, and hence $[F]_0^1 = 0$. The Rankine-Hugoniot jump conditions then simplify to

$$\begin{aligned} [\rho v]_0^1 &= 0, \\ [p + \rho v^2]_0^1 &= 0, \\ \left[\frac{v^2}{2} + \frac{\gamma}{\gamma-1} \frac{p}{\rho} \right]_0^1 &= 0. \end{aligned} \tag{2.88}$$

Radiationless shocks

The continuity condition guarantees that $\rho_1 = \rho_0 v_0/v_1$, and so the momentum condition yields $p_1 = p_0 + \rho_0 v_0(v_0 - v_1)$. Both can be substituted into the energy condition, and terms collected, so

$$\left(\frac{\gamma+1}{\gamma-1}\right) v_1^2 - \left(\frac{2\gamma}{\gamma-1}\right) \left(\frac{p_0 + \rho_0 v_0^2}{\rho_0 v_0}\right) v_1 + \left(\frac{2\gamma}{\gamma-1} \frac{p_0}{\rho_0} + v_0^2\right) = 0. \quad (2.89)$$

Eliminating p_0 and dividing by v_0^2 leads to a dimensionless equation

$$\left(\frac{\gamma+1}{\gamma-1}\right) \beta^2 - \frac{2}{\gamma-1} \left(\left(\frac{c_0}{v_0}\right)^2 + \gamma\right) \beta + \left(\frac{2}{\gamma-1} \left(\frac{c_0}{v_0}\right)^2 + 1\right) = 0, \quad (2.90)$$

with $\beta = (v_1/v_0)$. Defining the Mach number \mathcal{M} by the ratio of flow speed to sound speed, equation (2.90) simplifies to

$$\left(\frac{\gamma+1}{\gamma-1}\right) \beta^2 - \frac{2}{\gamma-1} (\mathcal{M}^{-2} + \gamma) \beta + \left(\frac{2\mathcal{M}^{-2}}{\gamma-1} + 1\right) = 0. \quad (2.91)$$

The \mathcal{M}^{-2} terms become negligible for sufficiently fast flows. Hence, in a monatomic gas with $\gamma = 5/3$, the solutions

$$v_1 = v_0 \quad (2.92)$$

and

$$v_1 = \frac{v_0}{4} \quad (2.93)$$

are possible. The first solution resembles the trivial case where nothing happens in the flow. The second or *strong shock* solution bears the implication that the monatomic gas cannot be compressed by a factor larger than 4 while passing through the shock. With the initial gas pressure being negligible compared to the ram pressure, and $v_0 \equiv v_s$ due to the fact that the shock is stationary in the frame of reference, the full strong shock solution to the postshock variables reads

$$\begin{aligned}
 v_1 &= \frac{v_s}{4}, \\
 \rho_1 &= 4\rho_0, \\
 p_1 &= \frac{3\rho_0 v_s^2}{4}.
 \end{aligned}
 \tag{2.94}$$

As energy is conserved, and kinetic flow energy is decreased by passing through the shock, the thermal energy of the plasma increases correspondingly. Following the shock, the internal energy of the gas is

$$\epsilon_{\text{int}} = \frac{3p_1}{2\rho_1} = \frac{9}{32} v_s^2,
 \tag{2.95}$$

which is just the same as the rest frame kinetic energy of the postshock gas. Writing the equation of state as $p/\rho = kT/\mu m_{\text{H}}$, we can calculate the postshock temperature from (2.95):

$$T_1 = \frac{3\mu m_{\text{H}} v_s^2}{16k}.
 \tag{2.96}$$

The highly increased temperature of the postshock plasma will lead to a comfortably subsonic velocity of the postshock flow. Hence, its ram pressure becomes unimportant, so the subsequent flow can be well approximated by isobaric cooling.

Isothermal shocks

Shock-heated gas will immediately begin to radiate and cool, requiring the use of the complete Rankine-Hugoniot conditions to solve the subsequent flow parameters. A fully cooled gas that has returned to its original temperature represents a useful limiting case. This is given e.g. when cosmic-ray heating or photoionisation heating maintain the initial and final temperatures. This case is called an *isothermal shock*; the sound speed $c_s^2 = p/\rho$ before and after the shock are the same, which can be used in place of the energy conservation condition:

$$\begin{aligned}
[\rho v]_0^1 &= 0, \\
[p + \rho v^2]_0^1 &= 0, \\
\left[\frac{p}{\rho}\right]_0^1 &= 0.
\end{aligned} \tag{2.97}$$

With the equation of state in an isothermal plasma being $p = \rho \cdot \text{const}$, effectively, $\gamma = 1$ at points 0 and 1 in the pre- and postshock plasma. We can now solve (2.98) in terms of the Mach number of the preshock flow, and obtain the quadratic equation

$$\left(\frac{v_1}{v_s}\right)^2 - (\mathcal{M}^{-2} + 1) \left(\frac{v_1}{v_s}\right) + \mathcal{M}^{-2} = 0. \tag{2.98}$$

Its solutions read

$$\begin{aligned}
v_1 &= v_s, \\
v_1 &= \mathcal{M}^{-2} v_s,
\end{aligned} \tag{2.99}$$

whereas the first one is trivial and the second one is the shock solution, as in the radiationless shock case. \mathcal{M}^2 is the maximum value for compression in an isothermal shock, which becomes clear from the shock solution and using the equation of continuity. In the absence of magnetic fields, the total shock luminosity calculates to

$$\dot{E} = \frac{\rho_0 v_s^3}{2} (1 - \mathcal{M}^{-2}). \tag{2.100}$$

This equation can be used to relate the total shock luminosity to other shock parameters in astrophysical applications.

2.2.3 The drivers of interstellar shocks

Supernova explosions

Upon their first interaction with the ISM of density ρ_0 , supernova ejecta drive a shock at velocity v_s , which is determined by the fastest moving ejecta with density $\rho(R, t)$ and velocity $v(R, t)$. Interstellar material is swept into a shell, slowing down the blast wave shortly thereafter, which in turn causes a reverse shock to propagate through the freely expanding ejecta. Thereby, kinetic energy is converted into thermal energy. The surface separating the hot shocked ISM and the hot shocked ejecta is called contact discontinuity.

Eventually, the mass of the shocked ISM will exceed the ejecta mass by far, and all of the ejecta will be shocked to high temperature, as the reverse shock has passed down to the explosion centre. At that point, the *Sedov-Taylor phase* of the blast wave evolution begins. At radius R , we can denote the specific thermal and kinetic energy behind the strong adiabatic blast-wave shock in accordance to equation (2.95);

$$\epsilon_{\text{int}} = \epsilon_{\text{kin}} = \frac{9}{32} \dot{R}^2, \quad (2.101)$$

with $v_s = dR/dt = \dot{R}$. Due to the blast wave speed decreasing with time, the specific internal energy of the hot gas bubble undergoes a change with radius. This among other changes vary in a self-similar way with respect to R however, and hence the total energy E_0 in the hot gas bubble, is

$$E_0 = \phi \frac{4\pi}{3} R^3 \rho_0 (\epsilon_{\text{int}} + \epsilon_{\text{kin}}) = \phi \frac{3\pi}{4} \rho_0 R^3 \dot{R}^2, \quad (2.102)$$

where ϕ is a structure parameter of order unity, accounting for the distribution of specific energy within the bubble. Neglecting radiative losses, E_0 is equal to the energy injected by the supernova. When $t \rightarrow 0$, and so $R \rightarrow 0$, this equation of motion for the bubble is solved by

$$R = \left(\frac{25}{3\pi\phi} \right)^{1/5} \left(\frac{E_0}{\rho_0} \right)^{1/5} t^{2/5}. \quad (2.103)$$

Hence, the instantaneous blast wave velocity $v_s(t)$ during the Sedov-Taylor phase is

$$v_s = \frac{2}{5} \left(\frac{25}{3\pi\phi} \right)^{1/5} \left(\frac{E_0}{\rho_0} \right)^{1/5} t^{-3/5}. \quad (2.104)$$

In fact, the size of a supernova remnant at a given time is only determined by the energy of the explosion E_0 and the density ρ_0 of the surrounding medium. The equation can be rewritten to express $v_s(r)$ as

$$v_s = \frac{4}{5} \left(\frac{2}{15\pi\phi} \right)^{1/2} \left(\frac{E_0}{\rho_0} \right)^{1/2} r^{-3/2}. \quad (2.105)$$

The end of the Sedov-Taylor phase is reached when the cooling timescale of the shocked plasma becomes shorter than the dynamical expansion time, and thus radiative losses become important. The $p dV$ work from the expanding hot bubble interior on the interstellar medium is subsequently radiated away, which changes the energy equation to

$$\dot{E} = -P \cdot 4\pi R^2 \dot{R}. \quad (2.106)$$

The adiabatic equation of state yields

$$E = \frac{4\pi}{3(\gamma - 1)} R^3 P, \quad (2.107)$$

with E being the instantaneous energy content of the bubble. Combining with the equations of mass and momentum conservation leads to

$$M = \frac{4\pi}{3} R^3 \rho_0, \quad (2.108)$$

and

$$\frac{d(M \dot{R})}{dt} = 4\pi R^2 P. \quad (2.109)$$

With these equations the intermediate evolution of the shell can be solved; $R \propto t^{2/7}$.

The final or *snow plow* phase of evolution is reached when the remnant keeps expanding only through the momentum of the dense shell, after the stored thermal energy has been

entirely radiated away. The momentum stored within supernova ejecta at late times can be ignored, leaving

$$M_0 v_0 = \frac{4\pi}{3} R^3 \rho_0 \dot{R}, \quad (2.110)$$

as the equation of momentum conservation, where M_0 is the ejecta mass thrown out in the supernova explosion at a mean velocity v_0 . This equation can be solved by

$$R = \left(\frac{3 M_0 v_0}{\pi \rho_0} \right)^{1/4} t^{1/4}. \quad (2.111)$$

Close to the end of this phase, the expansion velocity drops beneath the sonic speed of the ISM, and the remaining energy of the supernova decays through turbulent cascade.

Stellar wind bubbles

Stellar atmospheres scatter radiation from the central star; a process by which the momentum L_\star/c is transferred to the atmospheric gas, giving rise to an outflowing wind. If the wind attains a terminal velocity v_w and a mass flux rate \dot{M}_w , then

$$\dot{M}_w v_w = \frac{\eta L_\star}{c}. \quad (2.112)$$

The factor η accounts for multiple scattering of single photons, which increases the total momentum that can be deposited. This process is limited by the amount of energy produced by the star, so

$$\frac{1}{2} \dot{M}_w v_w^2 < L_\star. \quad (2.113)$$

It follows from (2.112) and (2.113) that $\eta < 2c/v_w$. Assuming a typical η value of 3–4, and an outflow velocity a factor $1 \lesssim \epsilon \lesssim 3$ times the escape velocity at the base of the outflow,

$$v_w = \epsilon \left(\frac{G M_\star}{r_\star} \right)^{1/2} \sim 1000 - 4000 \text{ km s}^{-1}. \quad (2.114)$$

The wind is in free expansion first, but is eventually affected by the interaction with the surrounding ISM of density ρ_0 , at which time it passes through an adiabatic shock at

an inner radius R_{in} . This shock is comparable to the reverse shock in early supernovae; it is thermalized and feeds into thick and hot gas masses, which actually provide the piston to inflate the stellar wind bubble. With the sound-crossing time scale in the hot plasma being much shorter than the dynamical bubble expansion time scale, the pressure p between the inner shock and outer shock is approximately constant. The rate of change in momentum per unit area of the stellar wind across the inner shock yields the pressure in the hot plasma,

$$p = \frac{3 \dot{M}_w v_w}{16 \pi R_{\text{in}}^2}. \quad (2.115)$$

By the relatively low expansion velocity of the bubble it is guaranteed that the outer shock is radiative and remains at a temperature of $\sim 10,000$ K, the same as the preshock gas, which is ionised by photons from the central star. The shocked interstellar gas can hence be assumed to form a thin shell at the outer bubble radius. The respective momentum conservation equation reads

$$\frac{d}{dt} \left(\frac{4\pi}{3} \rho_0 R^3 \dot{R} \right) = 4\pi R^2 p, \quad (2.116)$$

or, equivalently,

$$\frac{p}{\rho_0} = \dot{R}^2 + \frac{1}{3} \ddot{R} R. \quad (2.117)$$

Assuming a constant fraction $\phi = 1 - (R_{\text{in}}/R)^3$ of the total volume to be occupied by the hot gas, and the energy input $\dot{E}_w = \dot{M}_w v_w^2/2$ by the stellar wind being equal to the sum of the rate of change of thermal energy in the hot gas plus the rate of $p dV$ work performed on the interstellar gas, we obtain the energy conservation equation,

$$\dot{E}_w = \frac{d}{dt} \left(\frac{3p}{2} \frac{4\pi\phi}{3} R^3 \right) + p \frac{d}{dt} \left(\frac{4\pi}{3} R^3 \right). \quad (2.118)$$

Eliminating the variable of pressure from (2.117) and (2.118) leads to the equation of motion for the shell. Under the assumption that its solution is a power law,

$$R = \Theta t^\beta \quad (2.119)$$

having the correct boundary conditions, $R \rightarrow 0$ as $t \rightarrow 0$, one can conclude by substituting for R and its derivatives in t in the equation of motion, that $\beta = 3/5$. Hence,

$$\Theta = \left(\frac{125}{\pi (70\phi + 84)} \right)^{1/5} \left(\frac{\dot{E}_w}{\rho_0} \right)^{1/5}, \quad (2.120)$$

and finally,

$$R = \left(\frac{125}{\pi (70\phi + 84)} \right)^{1/5} \left(\frac{\dot{E}_w}{\rho_0} \right)^{1/5} t^{3/5}. \quad (2.121)$$

Chapter 3

Methods

This section shall give a brief overview about the technical aspects of our studies. We will describe the most important methods used therein and, if non-trivial, justify them physically. This includes cooling restrictions, SN triggering and their feedback mechanism.

3.1 Numerical hydrodynamics

In the previous chapter, we introduced a set of equations which suffices to describe the most important quantities of a gas mass in a dynamic system. In theory, these systems can be simulated by means of numerical codes that divide into two common categories: Smoothed Particle Hydrodynamics (SPH) codes feature distinct particles which represent a gas mass of certain spatial extent and density, and whose speed and location are clearly specified. However, there are situations when this type of code reaches the limits of its capabilities. One example has been the simulation of Kelvin-Helmholtz instabilities, until an approach for a solution was provided by Junk et al. [2010]. Hydrodynamic grid codes represent a viable alternative, which has been used for this reason to conduct the simulations presented in this work. Grid codes divide the simulation domain into distinct grid cells, each filled with a portion of gas at specified density, pressure and temperature, and moving at a certain speed.

To describe the hydrodynamic processes mathematically, the code makes use of a set of equations similar to the one presented in Section 2.3. As above, this includes a continuity equation comparable to (2.66),

$$\frac{\partial \rho}{\partial t} + \frac{\partial \rho u_j}{\partial x_j} = 0, \quad (3.1)$$

where u_j and x_j are the vector components of velocity and location, respectively. The first term is to be seen as a change in mass per time in a given volume, while the second accounts for inflowing and outflowing mass across the volume-bounding surface. Note that this equation guarantees a conservation of the overall mass. Euler's equation (2.70) modifies to

$$\frac{\partial \rho u_i}{\partial t} + \frac{\partial \rho u_i u_j}{\partial x_j} + \frac{\partial p}{\partial x_i} = 0, \quad (3.2)$$

as in our setup configuration, the potential component will be applied externally. The first part of equation (3.2) physically represents a force, and taken by its own would be e.g. a wave packet running through at constant momentum. The second part is also called "advection term". Advection terms generally describe quantities that are carried along in the direction u_j of movement, which in this case is the momentum. The third term describes the total pressure onto the volume-bounding surface. In its entirety, equation (3.2) conserves momentum. Lastly, to complete the set, we implement an equation of energy conservation, which is essentially equation (2.81),

$$\frac{\partial \rho e}{\partial t} + \frac{\partial \rho e u_j}{\partial x_j} + \frac{\partial p u_j}{\partial x_j} = 0, \quad (3.3)$$

with e being the energy per unit mass. As in equation (3.2), the first term accounts for changes in energy density per time. The second is an advection term describing interactions between neighbouring cells due to their respective energies. The last term represents processes of adiabatic expansion.

As can be seen from this set of equations, the basic idea of numerical simulations with hydrodynamic grid codes is the conservation of the three quantities mass, momentum and energy. It is worth noting here, that equation (3.3) specifically conserves internal energy, whereas kinetic energy might in some cases undergo a slight decrease when transferred from one cell to another. It is hence recommendable to adapt the geometry of the grid to the shape of the problem that is to be investigated.

3.2 The NIRVANA code

We perform 3D simulations with the magnetohydrodynamics code NIRVANA [Ziegler and Yorke, 1997] on a spherical grid. We have parallelised the code making use of the Message Passing Interface (MPI) library. Our simulations run for typically 48 hours on 6 SGI Altix processors. The gas evolution is calculated by solving the continuity, energy and Euler equations. A constant background gravitational potential accounts for the stellar and gaseous disc components, a bulge and the dark matter halo. The radiative cooling function used here is the equilibrium cooling curve described by Sutherland and Dopita [1993]. It accounts for the overall metallicity which is assumed to be equal to the solar metallicity, and operates only within a temperature range between a lower limit of 10^4 K and an upper limit of about 10^6 K, with the exact value depending on the respective halo equilibrium temperature: For some of our models, the only effect of the upper cutoff is to prevent cooling in freshly injected SN shells. This is required to establish a more realistic SN remnant, before the shell cools and the remnant enters the snow plow phase (see Section 3.4 for more details). We also use the upper cutoff to entirely inhibit cooling of the halo in some simulations. We do this to account for the unknown halo metallicity, which has a strong impact on radiative cooling. In this way, we cover the limiting cases of strong and negligible cooling of the halo.

3.3 Simulations on the SGI ALTIX computer

The code has been slightly redesigned to run on an SGI ALTIX 3700 Bx2 machine. Since the code is parallelised, we can make use of several of the 128 CPUs available on ALTIX. However, NIRVANA parallelises the y - and z -dimension of the simulation box by splitting them up into fragments of equal size; each fragment will then be processed by one rank. In order to keep the results mathematically correct, each box fragment is extended by two layers of “boundary cells” in the split-up dimension, which results in a four-cell wide overlap region of any two adjacent CPU simulation domains. If periodic boundary conditions are chosen, one single layer of boundary cells comprises three cells instead of two. These boundary cells can be altered by their respective master rank only, so it has to be ensured that during every time step the boundary data for other ranks is updated, which is done via the MPI routines in the NIRVANA code.

Table 3.1: Test runs for optimum computing time.

CPUs (y -dir.)	2	3	4	5	6	7	8	2	3	4
Cells (y -dir.)	100	99	100	100	96	98	96	100	99	100
CPUs (z -dir.)	1	1	1	1	1	1	1	2	2	2
Cells (z -dir.)	10	10	10	10	10	10	10	10	10	10
Run time (s)	274	194	160	127	108	98	93	162	119	88

Test runs

Higher number of CPUs however require more time-intense MPI routine calls per time step, which will mitigate the gain from parallelisation at some point. In order to find the optimum CPU number, we have performed several test runs displayed in Table 3.1. Each of these runs is done in a $600 \times y \times z$ simulation box, and comprises 100 time steps. The exact number of cells in y - and z -direction must be an integer multiple of the processor number, where $y \approx 100$ and $z = 10$.

As can be seen, parallelising the z -direction complicates matters in terms of MPI programming at minimal gain. The computing time for 2×2 and 2×3 processors is even higher than for 1×4 and 1×6 , respectively. For more than 6 processors the time decrease diminishes clearly, as every additional CPU increases the number of boundary cells by four, and the higher number of MPI routine calls becomes noticeable. We thus carried out the following simulations mostly with a number of six CPUs, parallelizing only in y -direction. With the chosen number of ranks, our simulations run for typically 48 hours.

3.4 Stellar feedback

Star formation is triggered randomly for each single cell as soon as certain criteria are met, and SNe occur immediately in an amount related to the mass of stars produced. In the progress of this work, two approaches have been made to implement realistic star formation rates to our models. The first approach is based on the Jeans criterion which has been outlined in Chapter 2, and the SN probability for one cell is solely bound to local criteria regarding this cell. The second approach implies the validity of a Kennicutt-Schmidt star formation law for our model galaxy, where global and local

key parameters are used to determine the supernova probability. Independently of the approach, SNe appear instantly in certain amounts at one time in one cell, henceforth referred to as a “SN event”, as the resolution of single SN is not feasible in this context.

3.4.1 Locally triggered star formation

Principally all star formation criteria in this approach are, directly or indirectly, dependent on each cell’s volume density ρ_{cell} . Firstly, cells of density $\rho_{\text{cell}} < 10^{-24} \text{g/cm}^3$ are discarded as being generally too rarefied to allow for star formation to set in at all. This value is empirically determined, and was found to yield a globally reasonable star formation rate for our system, if applied. Secondly, the cell mass m_{cell} is required to be higher than the Jeans mass

$$m_{\text{jeans}} = \frac{\pi}{6} \rho_{\text{cell}} \left(\pi \frac{\gamma p_{\text{cell}}}{100 \rho_{\text{cell}}} \frac{1}{G \rho_{\text{cell}}} \right)^{3/2}, \quad (3.4)$$

where $\gamma = 5/3$, and $p_{\text{cell}} = 2/3 e_{\text{cell}}$ the cell’s internal pressure. In most cases, if the first criterion is not fulfilled, the second will be neither. Thirdly, as we infer the number of SNe from the ejected cell mass $m_{\text{ex}} \simeq m_{\text{cell}}$, the velocity of the SN shock front can be fixed by spreading the ejected mass equally on the neighbour cells and providing the surroundings with a velocity corresponding to the kinetic energy released by the SNe. As bubbles resulting from less than about ten SNe will be of no significant effect, v_{ex} shall be required to exceed 30 km s^{-1} .

Whenever a cell qualifies for star formation by all three criteria, part of the cell mass will be permanently locked in low-mass stars, while SN progenitor stars are assumed to be instantly converted into SNe. Generally, for every 100 solar masses of gas converted into stars, one canonical SN, each releasing an energy yield of 10^{51} erg , will occur. The probability for a SN event, $P_{\text{SN,loc}}$ will be calculated, and in every time step SN events will trigger randomly. Knowing the cell density ρ_{cell} , its volume V_{cell} , and the length of the respective time step δt , the probability function reads

$$P_{\text{SN,loc}} = \frac{\rho_{\text{cell}} V_{\text{cell}}}{100 M_{\odot}} \cdot \epsilon_{\text{SF}} \cdot \frac{\delta t}{t_{\text{dyn}}}. \quad (3.5)$$

The overall star formation efficiency ϵ_{SF} shall have 0.3 as a default value. The dynamical time scale

$$t_{\text{dyn}} = \left(\frac{(dx)^2 + (dy)^2 + (dz)^2}{\gamma \frac{(\gamma-1) e_{\text{cell}}}{\rho_{\text{cell}}}} \right)^{1/2}, \quad (3.6)$$

with $\gamma = 5/3$, e_{cell} being the cell's internal energy, and dx , dy , and dz being the cell dimensions, represents the time which is required for the gas to produce stars. The mass of the cell, $\rho_{\text{cell}} V_{\text{cell}}$ will determine the event size. A negligible amount of the former remains within the cell after the event, whereas almost the entire cell mass is converted into stars, which themselves will return seven per 100 solar masses of gas through stellar winds and 18 per 100 solar masses by SN ejection. Hence, ~ 25 per cent of the cell mass will be ejected and evenly distributed to the neighbour cells, while ~ 75 per cent are locked into stars and SN remnants (see Section 3.5 below for details).

3.4.2 Star formation by the Kennicutt-Schmidt law

Star formation criteria include a local surface density exceeding the critical value $\Sigma_{\text{crit}} = 10 M_{\odot} \text{pc}^{-2}$ required for star formation to set in [Kennicutt, 1998]. Before calculating the local surface density, a volume density criterion applies for each cell to ensure that it is part of a region dense enough to produce stars, which is, in particular, the disc. Cells having a density less than $2 \times 10^{-24} \text{g cm}^{-3}$ are considered to be either halo cells or too rarefied for star formation to set in. In a few special cases, large high-density gas regions can be found far away from the disc. We are to assume then that our model galaxy is essentially breaking up as a consequence of too strong feedback. In consequence, once the disc has lost integrity, the Kennicutt-Schmidt law might no longer apply. To avoid perturbations from this effect, the column from which the surface density is calculated, comprising only the aforementioned disc cells, shall be no higher than one fourth of the total θ -range of the simulation domain, or 0.21π . This value chosen here, however, is not a critical parameter. Finally, in order to allow the system some relaxation after setup, SNe shall not occur before 1 Myr.

Just like in the local model, we regard only SNe type II, since star forming galaxies are observationally dominated by this type. Given the Salpeter IMF for the stellar mass distribution, we can easily calculate that of $100 M_{\odot}$ of gas locked up in stars, one type II SN progenitor exists, with the latter typically being as massive as $19.8 M_{\odot}$ on average, considering stars within a range from 8 to $120 M_{\odot}$.

We assume that stars in all our model galaxies form in accordance to a local Kennicutt-

Schmidt law [Kennicutt, 1998], given by

$$\Sigma_{\text{SFR}} = 2.5 \cdot 10^{-4} \left(\frac{\Sigma_{\text{gas}}}{M_{\odot} \text{ pc}^{-2}} \right)^{1.4} M_{\odot} \text{ kpc}^{-2} \text{ yr}^{-1}, \quad (3.7)$$

where Σ denotes the respective surface densities for star formation and gas mass. The gas surface density Σ_{gas} is calculated for every time step δt and every grid point within the r - ϕ -plane by integration of all disc cell masses along θ and dividing by the surface area $\delta r \cdot r \delta \phi$ of the respective column. Integrating along θ instead of the normal in respect to the disc midplane is a sufficient approximation since the disc extends only across a small angle $\delta \theta$. Moreover, constraining star formation by limiting the maximum column height to one fourth of the θ -range of the simulation domain will ensure that the angle of integration is sufficiently small.

The SNe in simulations featuring star formation by the Kennicutt-Schmidt law come in events of order 20 to 200 SNe at one time. Thus we can calculate a probability value for every disc cell and each time step, giving the likelihood for a SN event comprising ζ_0 SNe,

$$P_{\text{SN}} = \frac{\Sigma_{\text{SFR}} \delta r \cdot r \delta \phi \delta t}{100 M_{\odot} \zeta_0 n_{r,\phi}}, \quad (3.8)$$

with $n_{r,\phi}$ being the number of disc cells in the respective range of integration along θ . ζ_0 , referred to as the “event size” herein, is a preset parameter which will be kept constant during each single simulation. A random number is then drawn for each disc cell at every time step. The occurrence of a SN event is then triggered according to the local probability. Note that any altering of the resolution has to come with an appropriate change in the event size range; too high event sizes will require a manifold of the gas mass available in the cell, too small event sizes may produce unresolved bubbles.

3.5 Blast wave implementation

In this section we provide details of our blast wave implementation and follow the evolution of a single superbubble in a test simulation. If a SN event is determined for a specific cell, the following modifications in mass and energy will immediately take place: An amount of $100 \zeta_0 M_{\odot}$ is regarded to be no longer available in gaseous form since it is bound in stars, and henceforth removed from the cell. This amount can, in case of large ζ_0 's, exceed the cell mass, however, within our range of event sizes the total mass deficit due to this error is below a five per cent threshold for the entire disc, and hence considered negligible as it will insignificantly alter the disc dynamics. 25 per cent

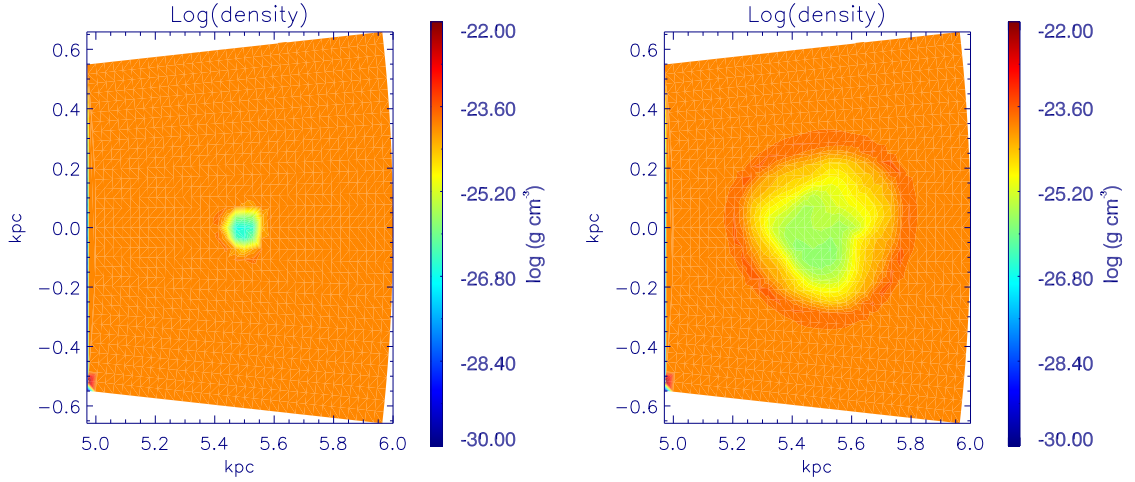


Figure 3.1: Mass density 0.1 Myr (*left*) and 2.0 Myr (*right*) after energy release.

of the newly formed stellar mass is returned to the gas phase due to stellar winds and SN ejecta. So, essentially, our code removes $75 \zeta_0 M_\odot$ of gas from the SN-triggering cell. The remaining mass is distributed equally among the six neighbouring cells except for a small remainder of $10^{-28} \text{ g cm}^{-3}$ within the central cell, so that the density increase is the same in all six adjacent cells. As mentioned before, we assume an energy injection of 10^{51} erg per SN, which will be implemented in accordance to a superbubble model assuming instantaneous energy injection and constant ambient density: 60 per cent of this energy is released as internal energy, fed into the SN cell and thus building up an overpressure with respect to the surroundings. The remaining 40 per cent of the energy total is kinetic energy, added as an extra velocity component to the neighbour cells. This velocity of the SN ejecta, v_{ex} , is typically greater than 10 km s^{-1} upon release, and therefore supersonic with respect to the sound speed inside the dense disc material, in agreement to SN superbubble observations.

To check the behaviour of our blast wave implementation, we have modelled a box of 35^3 cells on a spherical grid section of $5 \text{ kpc} < r < 6 \text{ kpc}$, and 0.07π in each θ and ϕ direction. There is neither an external potential, nor does any other force (e.g. centrifugal) apply. The overall density is set to $\rho = 10^{-24} \text{ g cm}^{-3}$, and the temperature to 10^4 K which is a common value for disk material in the models presented below. An energy equivalent of 100 SNe, or 10^{53} erg, is released at $t = 0$ right in the centre of the box as described above, forming an over-pressured, expanding hot gas bubble within a few 10,000 years (Figure 3.1). There is no cooling taking place in this test run. We follow the bubble

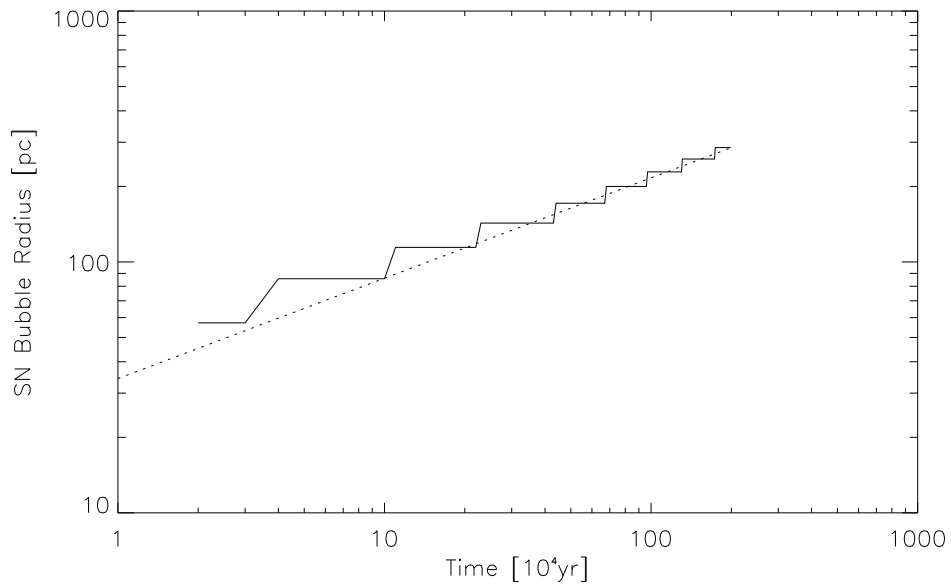


Figure 3.2: SN blast wave expansion of a 10^{53} erg event in a homogeneous $10^{-24} \text{ g cm}^{-3}$ medium. As expected, the blast wave expands in good agreement to a $r \sim t^{0.4}$ law (dotted line).

expansion over 2 Myr, tracing the distance between the shock front and the centre of explosion (Figure 3.2) as well as the energy decrease with time. The shock front in the underlying model is found to expand with a $r(t) \sim t^{0.4}$ law, as expected. Note however, that this is the expansion behaviour as expected from a bubble produced by one single SN. Superbubbles powered by many SNe spread out in time should rather expand with $r(t) \sim t^{0.6}$ [Oey, 2009]. This is because all of our bubble-producing SNe are triggered in one cell within one time step, as resolution prevents us from spreading SNe reasonably in space and time, in order to produce more realistic superbubbles. We estimate that this effect increases our bubble sizes artificially by about 25 per cent despite the smaller expansion rate, as we start out with a much higher energy. On the other hand, we find that about 10 per cent of the initially released energy are lost on the grid by numerical effects within the first 100,000 years, however, any further loss thereafter is comparatively small. Because the advection step of our code conserves only the thermal and not the kinetic energy exactly, preferably the kinetic energy component will be lost on the grid. Hence, the percentage of thermal and kinetic amounts will shift from an initial 60–40 to a ratio close to 72–28 in the long term. Figure 3.1 shows two snapshots of the SN bubble evolution, respectively 0.1 and 2 Myr after the event was triggered; the inner, rarefied region carries the internal energy which is steadily converted into kinetic energy as the over-pressured bubble expands. The kinetic energy resides within the compressed high-density region surrounding the bubble. Its slightly asymmetric form and initial imbalances in the kinetic/thermal energy distribution are a result of the coarse implementation. Figure 3.3 shows observations of four bubbles produced by single stars for comparison. Each of the bubbles has a more or less pronounced shell of compressed gas and a hot rarefied interior, and is about 10 pc in radius.

3.6 Boundary and initial conditions

We run our simulations on a 3D spherical grid. The values denoted here represent our typical simulation domain, which will be mostly used in the following chapters. Exceptions from this pattern will be denoted in the specific setup sections in Chapter 4. The simulation box is defined by a radial dimension r extending from 0.4 to 10.2 kpc, a polar angle θ covering a section between 0.04π and 0.96π , and an azimuth angle ϕ covering only a narrow “wedge” of the disc within -0.04π and 0.04π in range. Note that the space close to $\theta = 0$ and $\theta = \pi$ as well as the one at $r < 0.4\text{pc}$ must be omitted, as due to the spherical geometry grid cells within this space would become increasingly narrow. This in turn would lower their crossing timescales significantly,

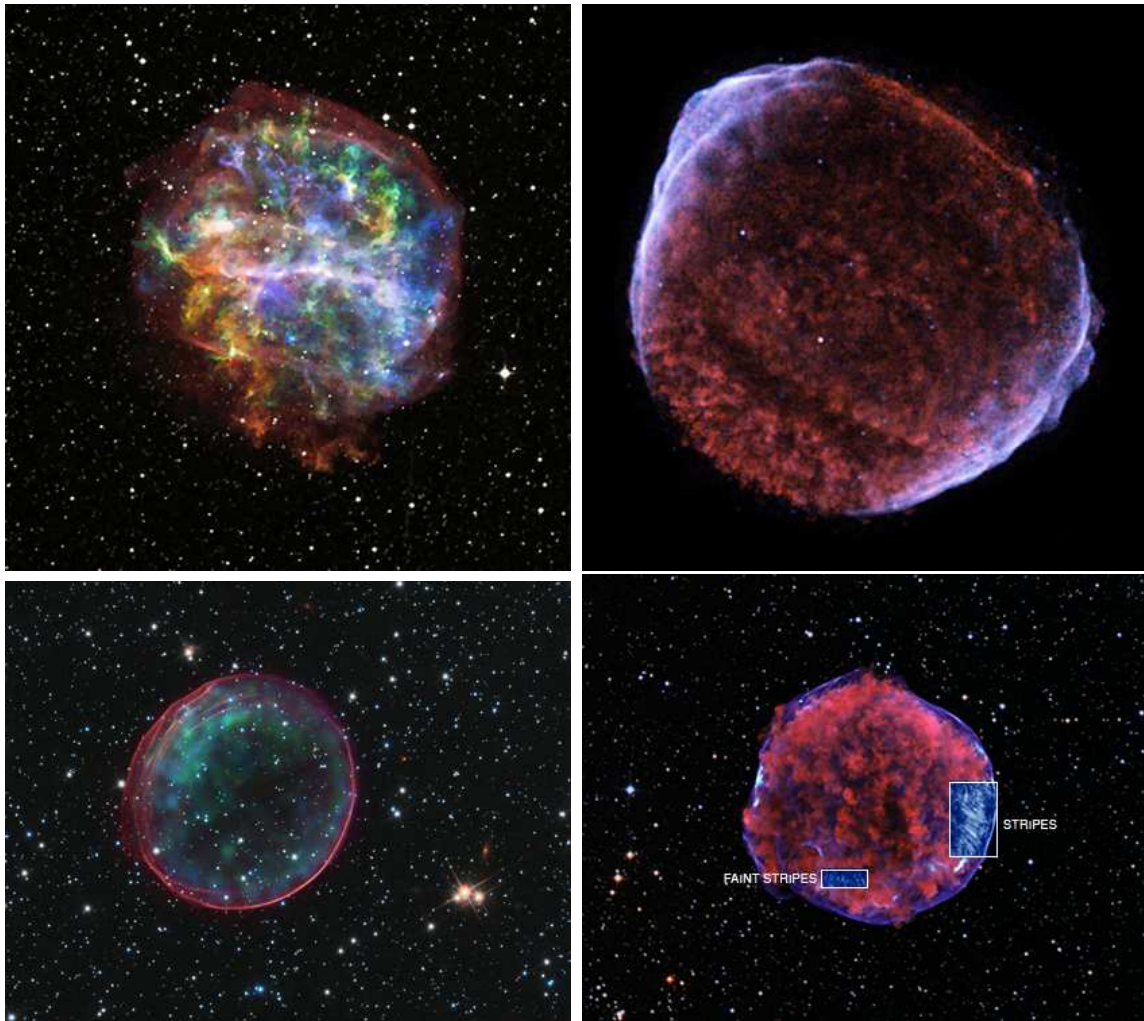


Figure 3.3: Various SN remnants in false colours. *Top left:* G292.0+1.8; *top right:* SN1006; *bottom left:* SNR0509-67.5; *bottom right:* Tycho's SN. Each bubble has a dimension of ≈ 20 pc across. *Source:* Chandra homepage.

requiring high computing times for the innermost zones. The simulation of just a small azimuthal sector of the disc instead of the whole ϕ -range is justified by assuming large-scale rotational symmetry and has been invoked to save additional computing time. For the main runs, the simulation domain is divided into $300 \times 96 \times 10$ grid cells in r -, θ - and ϕ -directions, respectively. Thus, a region near the disc midplane at $r = 1$ kpc is spatially resolved to ~ 33 pc. Our choice made here concerning the resolution will be explained in more detail at the end of this section. We choose reflective boundary conditions for the lower r boundary and the upper and lower θ boundaries each, whereas on the outer boundary in r -direction inflow and outflow of material shall be permitted. The boundary conditions to the boundaries in azimuthal direction (ϕ) are chosen to be periodical.

The total set of simulations performed in the frame of this work with their respective potential configurations and star formation prescriptions are listed in Table 9.1 in the Appendix. Further adjustments and the exact choice of parameters can be looked up in Chapter 4, and in Tables 5.1 and 6.1 in Chapters 5 and 6, respectively.

3.7 Basic setup

Halo

We assume that the initial halo is in hydrostatic equilibrium, and isothermal, suggesting a radially exponential distribution of baryonic matter (see equation (2.59)):

$$\rho_b(r, \theta) = \rho_{\text{crit,b}} \exp\left(-\Phi_{\text{tot}}(r, \theta) \frac{0.59 M_{\text{P}}}{k_{\text{B}} T}\right) \quad (3.9)$$

where M_{P} is the proton mass, and

$$\Phi_{\text{tot}}(r, \theta) = \Phi_{\text{disc}}(r, \theta) + \Phi_{\text{cent}}(r) + \Phi_{\text{H}}(r), \quad (3.10)$$

with Φ_{H} being either a dark halo potential according to Flynn et al. [1996] or a NFW profile dominating at larger radii. The other two potential components are due to the disc and the central bulge, respectively, and will be explained below. Note that the density in the inner parts of the halo remains within reasonable bounds due to our simulation domain being cut off a few 100 pc away from the centre. Since the halo shall be isothermal, we can vary T thus that the density ρ_b at the inner edge is not higher than typical disc density values, which are at least of order $10^{-24} \text{ g cm}^{-3}$. With the halo

density ρ_b given for all radii, the halo pressure p can be obtained from the ideal gas equation (2.61),

$$p = n_b k_B T, \quad (3.11)$$

where $n_b = 2\rho_b/M_P$, due to ionisation. The initial equilibrium state for the halo will only hold as long as the temperature is kept constant. Yet since in some of our runs radiative cooling is permitted for the model halo, the subsequent temperature decrease will provide a slight contraction of the halo with time. This in some sense accommodates for the fact that galaxies at the given redshift are still accreting halo material in significant amounts. However, the interaction between (filamentary) infall of material into a galactic disc and the onsetting wind is beyond the scope of this work and is studied thoroughly by Powell et al. [2011].

Disc

Several approaches to establish a stable disc-halo system are tested in this work. A detailed description for a possible setup can be found in Cooper et al. [2008]. In general, the following issues have to be kept in mind: Firstly, we want the gaseous disc to be rotationally supported (i.e. in hydrodynamic equilibrium), whereas the halo shall be pressure-supported (i.e. in hydrostatic equilibrium), which inevitably causes friction and shear effects in the transition zone. In addition, the halo cannot be truly set up in a pressure equilibrium with the disc, as the halo isobars are geometrically not parallel to those of the disc, which inevitably causes some motion in the halo. Therefore, we allow the system to relax for one Myr. The resulting setup is then sufficiently close to an equilibrium configuration to allow for the development of relatively stationary outflow solutions (compare below). As mentioned above in equation (3.9), the total potential is built up of three components, whereas the disc component $\Phi_{\text{disc}}(r, \theta)$ is a combined form of a Miyamoto-Nagai potential [Miyamoto and Nagai, 1975]:

$$\begin{aligned} \Phi_{\text{disc}} = & -\frac{G M_{D_1}}{\sqrt{R^2 + (a_1 + \sqrt{z^2 + b^2})^2}} \\ & -\frac{G M_{D_2}}{\sqrt{R^2 + (a_2 + \sqrt{z^2 + b^2})^2}} \\ & -\frac{G M_{D_3}}{\sqrt{R^2 + (a_3 + \sqrt{z^2 + b^2})^2}}. \end{aligned} \quad (3.12)$$

The bulge component $\Phi_{\text{cent}}(r)$ is basically a central potential,

$$\Phi_{\text{cent}} = -\frac{G M_{C_1}}{\sqrt{r^2 + r_{C_1}^2}} - \frac{G M_{C_2}}{\sqrt{r^2 + r_{C_2}^2}}. \quad (3.13)$$

These two components are further described in Flynn et al. [1996], which we will use as the basic prescription for our disc setup. In the setup configurations of Chapter 5 and 6 the mass-related parameters therein (M_{D_1} , M_{D_2} , M_{D_3} , M_{C_1} and M_{C_2}) are scaled down to match the residual disc mass, which we assume to have settled into the disc. The length-related sizes (a_1 , a_2 , a_3 , b , r_{C_1} and r_{C_2}) are also scaled down in these setups, effectively shrinking the scale radius of our disc.

We have followed the evolution of the disc in several test models, finding the gas density distribution of the disc $\rho_d(r)$ to be insensitive to inward and outward flow movements for a wide range of variations, as long as the pressure gradient and rotational velocity of the disc material account for the hydrodynamic equilibrium. We use a density profile exponential in radius for most simulations, with a specified cutoff radius, which is vertically non-stratified. This latter fact is unproblematic since the disc will be given enough time for relaxation, so stratification will develop in the early course of the respective models (~ 1 Myr). The disc density thus reads

$$\rho_{\text{disc}}(r, z) = \rho_{\text{disc}}(r) = \rho_{\text{disc},0} \exp\left(-\frac{r}{r_{s,D}}\right), \quad (3.14)$$

with $\rho_{\text{disc},0}$ being the gas density in the disc centre, and $r_{s,D}$ the scale radius.

As an alternative to the exponential distribution, one could use a constant gas density profile, which has been observed e.g. by Bendo et al. [2010] for NGC 2403; this is to be examined more closely in Section 5.4. Our gaseous disc will be non-stratified in z -direction initially, but will relax into a stratified state within the first Myr of the simulation. The disc gas pressure follows from the ideal gas equation (2.61), just as for the halo gas pressure. The gravitational force will be accounted for by the implementation of $\Phi_{\text{tot}}(r, \theta)$ as an external potential.

Chapter 4

Galactic winds with a logarithmic halo density profile

The models presented in this chapter mainly have been used as test models to ensure the overall stability of the disc-halo system and the correct setup of the supernova implementation routine. Nevertheless, we can already obtain some valuable intermediate results from these models, which will allow us later to refine the current setup step by step.

Our first set of simulations is carried out on a spherical grid $600 \times 100 \times 6$ cells in size. The dimensions of the grid, however, initially differ from those mentioned in Section 3.6: the radial dimension r extends from 1 kpc to 20 kpc, the polar angle θ from 0.1π to 0.9π and the azimuthal angle ϕ from $-1/6\pi$ to $1/6\pi$, or one sixth of a full disc. We use the local star formation recipe as explained in Subsection 3.4.1, with the blast wave implementation from Section 3.5.

4.1 Preconsiderations

4.1.1 Multiphase interstellar medium

As detailed in Section 3 above, we allow radiative cooling only in between a certain range of temperatures. Below the lower temperature threshold for the cooling function, background radiation is assumed to keep the disc temperature stable at an overall value close to 10^4 K. The upper temperature threshold is a necessary tool in order to establish a resolved multiphase ISM. In reality, the ISM exhibits a filamentary structure, comprising

cold ($T < 200$ K), dense filaments of molecular gas capable of producing stars, but only having a small volume filling factor of about 5 per cent [de Avillez and Breitschwerdt, 2004]. The rest consists mainly of hot, rarefied gas with long cooling time, filling the large spaces in between the filaments. SN bubbles forming in this multiphase medium can expand to large radii, since the cooling process of their shock fronts, which would otherwise provide an efficient energy drain, cannot effectively take place within the hot, thin gas phase. In our numerical model we face a certain discrepancy in resolution: On the one hand, we are interested in a large-scale phenomenon (some kpc), inevitably meaning that the simulated domain, and therefore cell size has to be sufficiently large, on the other, a resolution of the multiphase gas disc structure would be desirable, calling for a cell size of order a parsec in order to resolve the cold, dense filaments, as is used by de Avillez and Breitschwerdt [2005]. This is in particular important for shock fronts: The existence of a volume-filling low density component means that some part of the bubble expansion happens adiabatically. All these issues enforce a compromise on our simulations to combine the key attributes of both phases; i.e. providing the cells of a few dozen pc in length with the average gas density of the ISM, but still not allowing the cooling rate to be too efficient, which would be the case in rarefied, warm ISM regions represented by average-density cells. Note that with a standard cooling rate, a shock front within our isotropic disc can cool down to the environment value within even less than a time step, removing large quantities of energy from the SN bubble interior. A feasible solution is here to forbid cooling completely above a threshold temperature higher than the initial halo temperature but lower than the temperatures typically found in the SN bubble shock fronts. This procedure allows the bubbles to acquire a diameter well above the resolution limit before shell cooling sets in.

4.1.2 Global kinetic energy

Among other effects, a galactic wind could be launched by the sheer amount of kinetic energy which accumulates within a gas-rich galactic disc over time. Let us therefore consider a galactic gas disc with a mass of the order $10^{10} M_{\odot}$, as commonly found for Lyman-break systems. Let us further assume the SFR to be around $10 M_{\odot}/\text{yr}$, which means in turn that we are going to encounter about one SN every 10 years. Normalised to the entire mass of the system this would mean a SN rate 10 times as high as in the Milky Way, which too has a gas mass of order $10^{10} M_{\odot}$ (the larger part of its mass is locked in stars) at a SFR of $1 M_{\odot}/\text{yr}$. Our model system may therefore be regarded to be in a starburst phase. SNe are known to give rise to considerable turbulent motions

within a disc [Dib, Bell and Burkert, 2006], each yielding a contribution of $\sim 10^{51}$ erg at a presumed efficiency $\epsilon = 0.1$ to the overall kinetic energy stored within the gas phase of its host galaxy. Unlike internal energy, kinetic energy has the advantage that substantial fractions will not be radiated away immediately, but rather dissipate on the dynamical timescale [Mac Low et al., 1998, Burkert, 2006]. Allowing the turbulent energy to pile up for ~ 100 Myr would result in an energy reservoir of order 10^{57} erg for the disc as a whole. Since the gravitational binding energy is known to be of the same order for a $10^{10} M_{\odot}$ system of 5 kpc radial extent, material ejections from the disc into its surrounding galactic halo indeed becomes plausible at a certain point in time. The approach of launching a turbulence-driven outflow has been investigated by Scannapieco and Brüggén [2010]. In their models SN feedback was simulated by injecting unresolved kinetic energy, which is described by an isotropic pressure term in the Euler equation. Here, we also investigate kinetic energy driving, studying models where we inject only kinetic energy, instead of a combination of thermal and kinetic energy (compare below). We will however resolve the kinetic energy.

4.1.3 Resolution

Since the main focus of this work lies on galactic outflows, which constitute a large-scale phenomenon, it is unnecessary to resolve the disc at high resolution levels. The resolution of single SNe would require a cell size around one pc [Powell et al., 2011], which would lead to unreasonably high computing times in our case. As our SNe are clustered in superbubbles of several SNe, we can tackle this problem by allowing larger typical cell sizes for our model, resulting in common bubble sizes of several hundred. For the first series of simulations presented in this chapter, the typical disc cell at 1 kpc radius is resolved at 33 pc.

4.2 Setup and initial conditions

4.2.1 Halo setup

The overall external potential is described by equation (3.10), where $\Phi_{\text{H}} = \Phi_{\text{FSC}}$ is given by equation (2.58), with $r_0 = 8.5$ kpc. For large radii, the rotational velocity will converge against a value of 220 km s^{-1} . Equation (2.59) describes the setup of the baryonic density distribution in the halo,

$$\rho_b(r, \theta) = \rho_0 \exp\left(-\Phi_{\text{tot}}(r, \theta) \frac{0.59 M_{\text{P}}}{k_{\text{B}} T}\right), \quad (4.1)$$

where ρ_0 has a value of $1.67 \times 10^{-28} \text{ g cm}^{-3}$, or 10^{-4} gas particles per cm^3 . The initial temperature of the halo gas is at $2 \times 10^6 \text{ K}$, which leads to a long cooling time. Note that for the simulations in this chapter there is no upper temperature threshold for cooling, however, the halo density is of order $10^{-29} - 10^{-30} \text{ g cm}^{-1}$, which, in combination with the high temperature leads to a very long cooling time, so cooling is effectively negligible. The halo pressure results immediately from its density via the ideal gas equation,

$$p = n_b k_{\text{B}} T. \quad (4.2)$$

Rotation does not occur in the halo, however, there will inevitably be some shearing at the contact surface between halo and disc.

4.2.2 Disc setup

Since the model by Flynn et al. [1996] is based on milky-way data, we will first examine the evolution of galactic outflows for a milky way like system, and thus use the disc parameters described in their work to obtain the disc potential (compare equation (3.12)). Table 4.1 gives an overview over the respective parameters. This potential accounts for both stellar and gaseous disc components.

Further, the disc has an exponential gas density profile, reading

$$\Sigma_{\text{D}} = \Sigma_{\text{D},0} \exp\left(-\frac{r}{r_{\text{s,D}}}\right), \quad (4.3)$$

where $\Sigma_{\text{D},0}$ is the gas density at zero radius, and has a value of $7.8 \times 10^3 M_{\odot} \text{ pc}^{-2}$, and $r_{\text{s,D}} = 3 \text{ kpc}$ is the disc scale radius. There is no stratification in z -direction, however; instead, the system will relax into equilibrium during the first Myr of the simulation. The initial vertical extent of the disc will be 0.75 kpc both above and below the disc midplane, thus resulting in a central gas volume density $\rho_{\text{D},0} = 3.5 \times 10^{-22} \text{ g cm}^{-3}$. We assume the gas disc to be constantly kept at a temperature of 10^4 K due to background radiation, which is realised in the simulations by switching off radiative cooling beneath this value. Again, with the temperature and volume density known, we can obtain the gas pressure inside the disc through the ideal gas equation (see above). Our disc is cut off at an outer radius of 10 kpc . The gas mass in the disc can then be fixed to

Table 4.1: External potential parameters for simulation set 1 (F-ST and F-KE).

Component	Parameter	Value
Dark Matter Halo	r_0	8.5 kpc
	v_H	220 km s ⁻¹
Bulge	r_{C_1}	2.7 kpc
	M_{C_1}	$3.0 \times 10^9 M_\odot$
	r_{C_2}	0.42 kpc
	M_{C_2}	$1.6 \times 10^{10} M_\odot$
Disc	b	0.3 kpc
	a_1	5.81 kpc
	M_{D_1}	$6.6 \times 10^{10} M_\odot$
	a_2	17.43 kpc
	M_{D_2}	$-2.9 \times 10^{10} M_\odot$
	a_3	34.86 kpc
	M_{D_3}	$3.3 \times 10^9 M_\odot$

$3.71 \times 10^{11} M_{\odot}$, which is little over 60 per cent of the total baryonic disc mass. The setup thus resembles a gas-rich analogue of the Milky Way.

4.3 Test models

We have performed two simulations including the logarithmic halo density profile described by Flynn et al. [1996]. The first model named “F-ST” injects SN energy in form of a thermal and a kinetic component, whereas the second model “F-KE” omits the thermal component, and injects only the kinetic part. These, and all simulations following in later chapters, are tabulated in the Appendix.

4.3.1 Thermal and kinetic energy injection

As mentioned above, the mass of a given cell determines the likelihood of a SN event on the one hand, and the size of the event on the other. Typical disc cells have a density of up to several $10^{-21} \text{ g cm}^{-3}$, implying a mass of several million M_{\odot} . At a star formation efficiency of $\epsilon_{\text{SF}} = 0.03$ and one SN per $100 M_{\odot}$, typical event sizes will be in the range around 1000 SNe each. In our first model (F-ST) an event is represented by a superbubble which has already reached its Sedov expansion phase, where the inner hot and rarefied gas region with its enormous pressure accounts for the accelerated expansion of the overlying compressed and shock-heated layer of gas. We inject 60 per cent of the total SN energy released (10^{51} erg per SN) as thermal, and the remaining 40 per cent as kinetic energy.

Figure (4.1) shows three different snapshots of the gas mass density at 30, 70 and 250 Myr, respectively. We can already discern the emergence of an outflow-like structure, with a superbubble escaping from the disc on its upper side at 30 Myr. This outgoing bubble sweeps a path of rarefied material through the denser halo, entraining high-density disc material on its outer limb. The path forms a conical structure until 70 Myr, where we also find another bubble attempting to escape the disc on its lower side. However, the outflow is not continuous as most bubbles are forced back into the disc by thermal halo pressure. The outflow ceases completely until 250 Myr, yet still seems capable of opposing the ambient halo pressure. Since the halo density is very low with an order of magnitude in between 10^{-29} and $10^{-30} \text{ g cm}^{-3}$, the high temperature implies a long cooling time; halo ram pressure due to cooling flow movements is therefore too

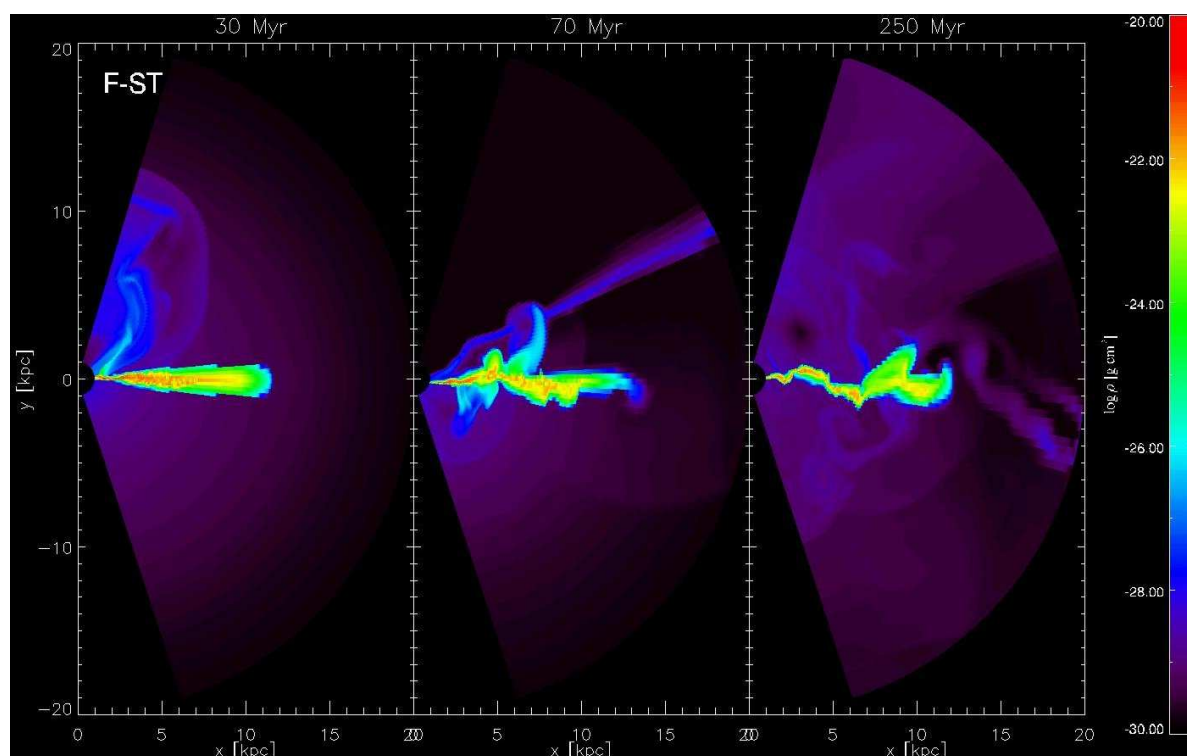


Figure 4.1: Simulation F-ST with each SN releasing 4.0×10^{50} erg as kinetic, and 6.0×10^{50} erg as thermal energy. The elapsed time is denoted above each snapshot. Shown is the logarithm of mass density in meridional midplanes.

small to suppress outflows effectively. It is also worth noting that the bubbles escaping, and in one case provoking an outflow, emerge very close to the disc centre.

One might argue that the halo potential, which accounts for a continuously decreasing density with radius, should be a supporting factor for galactic outflows. Since the halo is isothermal, its pressure also decreases with radius, thus presenting ever less resistance to an outgoing shock front. This however requires that a superbubble leaves the disc at all in the first place, at which point the disc mass constitutes a limiting factor. Due to the high density and hence pressure within the disc, even a presumably strong event may prove too weak to build up enough bubble pressure to finally break free from the disc. This becomes clear by the fact that until 70 Myr only two bubbles leave the disc, ultimately resulting in an asymmetric appearance.

We will now gradually refine the methods used and vary certain parameters in order to reproduce continuous outflows and reliably describe their actual triggers.

4.3.2 Kinetic energy injection only

For the last model one key method was the implementation of a Sedov-Taylor blast wave model. However, it has also been proposed that turbulence from SN feedback may give rise to a galactic outflow [Scannapieco and Brüggen, 2010]. We examine this more closely in our second model (F-KE), where we inject only 40 per cent of the 10^{51} erg per SN as kinetic energy, omitting the other 60 per cent. Apart from this, no further changes from model F-ST were implied on the setup.

The snapshots in Figure 4.2 show the gas density at 20, 250 and 600 Myr, respectively. Kinetic energy feedback quickly builds up a high amount of turbulence in the disc, and changes its overall density profile into a more clumpy structure. This can be seen clearly in Figure 4.3 (left box), showing the mass density against radius in the inner regions of the disc. The density graph represents a cut through the disc midplane. The difference between peaks and dips can extend well over one order of magnitude, whereas the dense clumps are separated by several 100 pc at least, and about one kpc at most. The overall turbulent energy stored within the disc is visualised in the right box of Figure 4.3; the mass-averaged random motion speed is plotted against time. It can be seen that the turbulent motion quickly stabilises in a timespan between 20 and 250 Myr, persisting at a level of 40 km s^{-1} , but showing some increase towards 250 Myr. Eventually, the increasing storage of kinetic energy inside the disc will no longer be sustainable, at which point the disc will lose integrity and be torn apart. The last snapshot in Figure 4.2

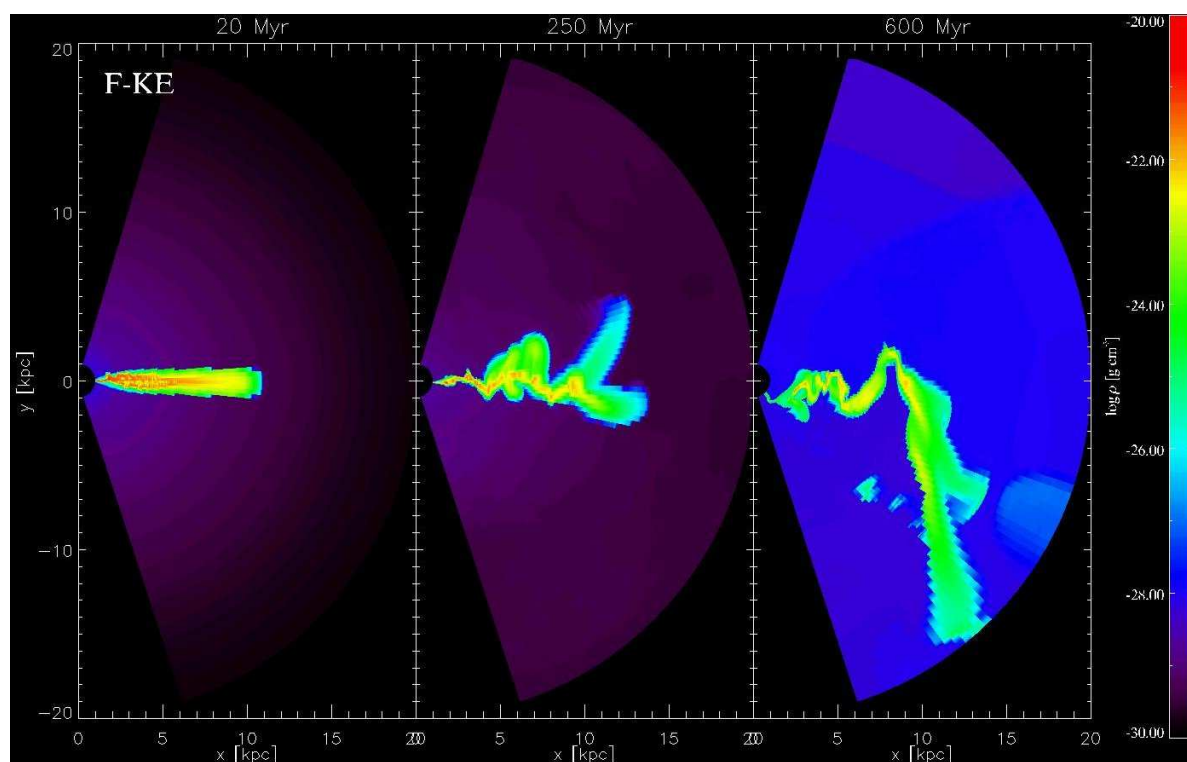


Figure 4.2: Simulation F-KE with each SN releasing 4.0×10^{50} erg as kinetic energy only. The elapsed time is denoted above each snapshot. Shown is the logarithm of mass density in meridional midplanes.

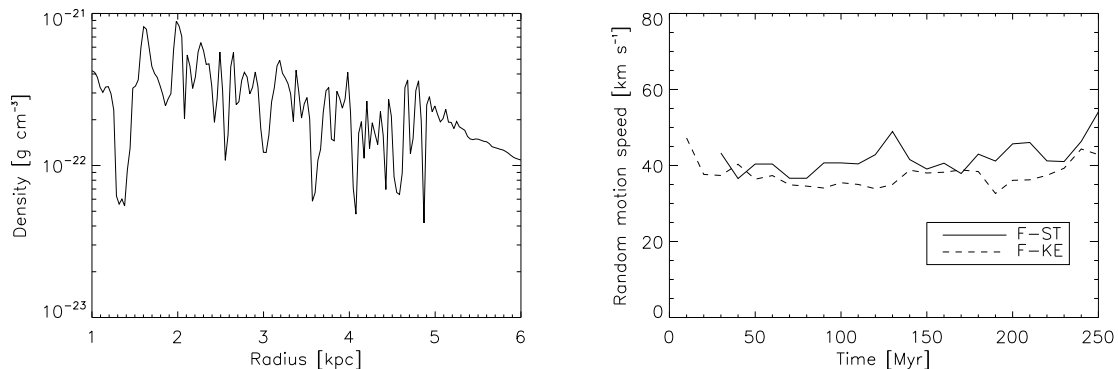


Figure 4.3: *Left:* Density plotted in the equatorial midplane against radius in a range of $1 \text{ kpc} < r < 6 \text{ kpc}$. *Right:* Mass-averaged random motion speed of disc material against time.

shows the disc just prior to its ultimate dissolution; the halo meanwhile has undergone significant contraction due to cooling, which may be another factor encumbering the emergence of an outflow.

We find in this model that kinetic feedback alone does not suffice to launch an outflow of any kind; instead, the disc as a whole is ripped apart after several 100 Myr. The sound waves caused by turbulence in the disc do not show any interaction with the halo, while superbubbles driven by thermal and kinetic energy are capable of heating the halo. Comparison of the two graphs in the right panel of Figure 4.3 shows that turbulence in both F-ST and F-KE stabilises at the same level; hence the respective snapshots at 250 Myr for both runs do not differ significantly from each other. Figure 4.4 confirms that in F-ST the halo is successfully heated up by an outbound bubble, leaving behind an extended region of gas as hot as 10^7 K . F-KE however shows only small temperature fluctuations within the halo.

Though, it has to be taken into account that already in run F-ST outflows could hardly escape the disc at all. Therefore it cannot be excluded yet that kinetically driven winds can arise; we shall examine this issue again in Section 6.2 with a different set of parameters.

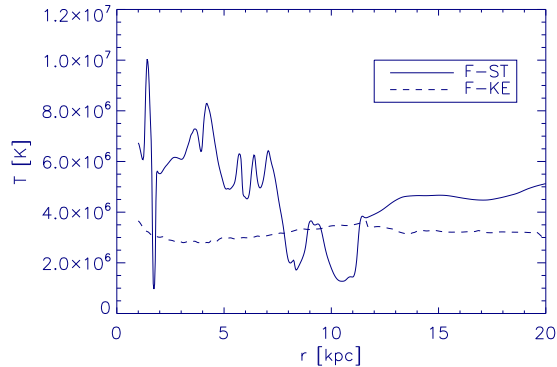


Figure 4.4: Halo temperature is plotted against radius r at a polar angle $\theta = 0.27\pi$, for runs F-ST (solid line) and F-KE (dashed line), respectively.

4.4 Implications

In summary, we can conclude this chapter with a number of valuable implications on the current setup. We can reproduce at least a temporary outflow by injecting both thermal and kinetic energy, but not with kinetic energy alone. This points to the possibility of a resolved multiphase ISM playing a greater role in the emergence of galactic outflows. In order to conduct further studies on the subject, however, it seems reasonable to adapt some modifications on the current model regarding the methods and setup parameters: Firstly, the disc-halo system is exceptionally massive, coming close in weight to the mass of the Milky Way. As galactic winds are a phenomenon known to occur with the much lighter Lyman-break galaxies at high redshift [e.g. Pettini et al., 2000], disc masses of order $10^9 M_{\odot}$ to only a few $10^{10} M_{\odot}$ seem more plausible. The high disc mass likely also oppresses the entrainment of gas filaments from the disc body. Secondly, the current SN implementation allows for very powerful events of 1000 SNe to occur. This is also due to the large cell mass, which, due to the spherical grid, is relatively large in the outer disc cells. We therefore attempt resolve this bias in the next chapter, so local star formation will no longer depend on the size of the respective grid cell. Since bubbles more close to the centre of the disc were the only ones we found escaping from the disc, it seems likely that with more SN events taking place in the inner disc, a more continuous outflow can be triggered. Keeping a given SFR and shifting the spatial dispersion of SN events to the inner cells also means going from a few large events to more smaller events. The effects of the event size will once more be addressed in Section 6.4. Thirdly, the halo profile may have an impact on the outflow velocity once it has developed, as the

rapidly declining pressure in outward direction allows outflowing material to proceed unhindered. It is thus necessary to implement a halo profile which allows the baryonic halo density, and hence pressure, to converge at large radii.

However, the radially constantly declining baryonic halo density combined with a massive, gas-rich disc are favourable conditions for emerging winds due to the radially declining thermal halo pressure and the high SFR. Still, a strong supersonic wind did not emerge in our models, which suggests that galaxies comparable in mass to the Milky Way generally favour a subsonic, or “fountain” solution (for the exact distinction between winds and fountains, see Chapter 6). Our results here therefore compare e.g. to the large SINS galaxies [Genzel et al., 2008] with their high SFRs.

Supersonic winds would furthermore produce coherent velocity fields on both sides of the disc. The magnetic field vectors would then correspond to the velocity vectors, since magnetic fields would be shaped by entrained material. Mao et al. [2010] could prove through Faraday rotation that the Milky Way lacks a galactic dipole magnetic field in relative vicinity to the Sun, suggesting the absence of a large-scale galactic wind. This absence of winds in Milky Way-like systems is in agreement to our simulations: our simulated discs are rich in gas compared to the Milky Way, implying more efficient star formation and hence SN feedback. In turn, one would not expect stronger outflow activities in the Milky Way than in our models.

Chapter 5

Galactic winds with a converging halo density profile

5.1 Preconsiderations

This chapter is focussed onto two aspects that have an influence on the strength and geometry of galactic outflows: Firstly, we aim to investigate the effect of clustering SN events in time, causing stronger but less frequent superbubbles to occur, and further shifting the radial spreading of powerful events towards the inner disc cells, which we assume to represent the part of the galaxy where star formation is most intense. Secondly, we compare two different gas discs of equal mass to probe the effects of different radial gas density distributions. All of our simulations have been updated with respect to the setup in Chapter 4; this concerns the gas density distribution in the halo, the shape of the external halo potential, and the significantly reduced disc mass. Details are given below.

5.1.1 Resolution

We have run several simulations, resolving typical disc cells at 1 kpc radius to respective resolutions of 12, 16, 30, 33, 36 and 65 pc, using local star formation criteria (see Subsection 3.4.1). The results are shown in Figure 5.1. It can be seen immediately that the presented approach only allows for a small range of variation in the resolution. Finely resolved discs imply smaller individual cell masses, which result in a lower number of cells qualifying for star formation, as the Jeans mass does not change with increasing

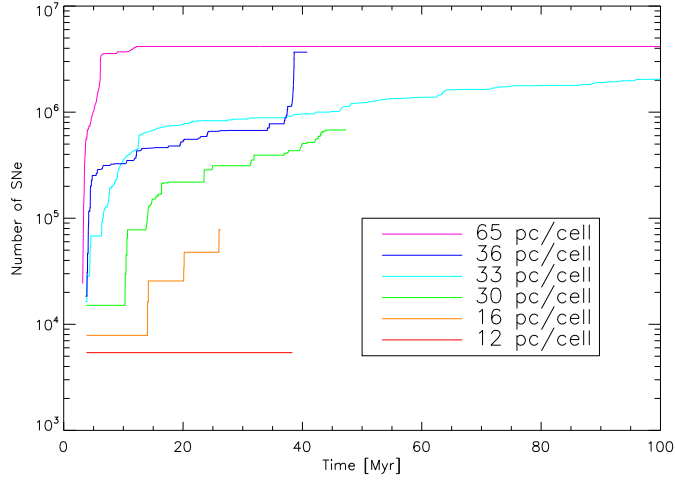


Figure 5.1: Supernova rates at different resolutions.

resolution and is the minimum mass for star formation. At 12 pc resolution, no stars form at all over several 10 Myr, meaning that cells hardly ever overgo the Jeans mass. Conversely, at the lowest resolution, high cell masses lead to a massive outbreak of SNe, which soon thereafter stops entirely as a result of complete disruption of the disc structure. Reasonable results can be found only within a resolution range of 30 – 36 pc, where the overall star formation rate of the system lies within a range one would expect for a system of comparable mass undergoing a starburst phase. Simulations with the current setup will thus be carried out exclusively at 33 pc resolution.

5.2 Setup and initial conditions

As we have established in the previous chapter, the external halo potential according to equation (2.58) leads to a density which continuously decreases with radius. This allows escaping material from the disc to proceed very far out, since pressure resistance too decreases with radius. On the other hand, outflows are encumbered by the large total mass of the disc-halo system. We now improve the model by firstly setting up a converging halo density profile, and secondly reducing the total mass of the system in order to assess the constraints on the onset of galactic outflows more accurately. In addition, the boundaries of the simulation box are adapted to $0.4 \text{ kpc} < r < 10.2 \text{ kpc}$, $0.04\pi < \theta < 0.96\pi$ and $-0.04\pi < \phi < 0.04\pi$. The simulation domain comprises $300 \times 96 \times 10$ cells, keeping a 33 pc resolution of the typical disc cell at $r = 1 \text{ kpc}$. Table

Table 5.1: Simulation setup parameters for the set of simulations presented in Chapter 5.

Run	Resolution	Clustering function $\zeta(r)$	Disc density profile
Res12	12 pc	$\zeta(r) = 3 r^{-2}$	$\rho_{\text{disc}} = \text{const}$
Res16	16 pc	$\zeta(r) = 3 r^{-2}$	$\rho_{\text{disc}} = \text{const}$
Res30	30 pc	$\zeta(r) = 3 r^{-2}$	$\rho_{\text{disc}} = \text{const}$
Res33 ^a	33 pc	$\zeta(r) = 3 r^{-2}$	$\rho_{\text{disc}} = \text{const}$
Res36	36 pc	$\zeta(r) = 3 r^{-2}$	$\rho_{\text{disc}} = \text{const}$
Res65	65 pc	$\zeta(r) = 3 r^{-2}$	$\rho_{\text{disc}} = \text{const}$
CD-1	33 pc	$\zeta(r) = \zeta = 1$	$\rho_{\text{disc}} = \text{const}$
CD-1R	33 pc	$\zeta(r) = r^{-2}$	$\rho_{\text{disc}} = \text{const}$
CD-3	33 pc	$\zeta(r) = \zeta = 3$	$\rho_{\text{disc}} = \text{const}$
CD-3R	33 pc	$\zeta(r) = 3 r^{-2}$	$\rho_{\text{disc}} = \text{const}$
CD-4	33 pc	$\zeta(r) = \zeta = 4$	$\rho_{\text{disc}} = \text{const}$
CD-4R	33 pc	$\zeta(r) = 4 r^{-2}$	$\rho_{\text{disc}} = \text{const}$
ED-3	33 pc	$\zeta(r) = \zeta = 3$	$\rho_{\text{disc}}(r) \propto e^{-r/r_{\text{s,D}}}$
ED-4	33 pc	$\zeta(r) = \zeta = 4$	$\rho_{\text{disc}}(r) \propto e^{-r/r_{\text{s,D}}}$

^a“Res33” and “CD-3R” are two denotations for the same run.

9.1 in the Appendix contains the SF prescription, and the most important halo and disc setup adjustments for all simulations.

5.2.1 Halo setup

The constant rotational velocity at large radii, which the halo model by Flynn et al. [1996] is based on, ensures in a certain way, that the potential and hence the halo gas density does not flatten outwards. We therefore use an alternative potential description for the next set of simulations: primarily, we want to ensure the convergence of baryonic density to a preset background value. Further, the largest baryonic density decrease in radius shall be within the simulation domain, followed by an outer region with comparatively little change in density over radius. A density profile like this is expected to allow

outflows still to escape from the disc, but opposing significant pressure to outbound shock fronts at higher radii, occasionally causing them to stop and fall back onto the disc. The exact shape of our potential is chosen such that it converges against the NFW profile with radius, but in the inner region allows the baryon density to decrease significantly. This implies a relative steep potential slope close to the centre, which actually encumbers the emergence of outflows. It is hence suggestive to investigate the effects of SN clustering (see Section 5.3 below) using this specific setup.

It is known from Navarro et al. [1996], that the *total* density in a standard halo can be described by

$$\rho_{\text{tot}}(r) = \frac{\rho_{0,\text{DM}} R_s^3}{r (r + R_s)^2}, \quad (5.1)$$

where $\rho_{0,\text{DM}}$ is the background density of dark matter, and R_s is the scale radius of the halo. We can now calculate the cumulative halo mass M_{cum} from the density by integration over the radius r :

$$M_{\text{cum}}(r) = 4\pi \int \frac{\rho_{0,\text{DM}} R_s^3}{r (r + R_s)^2} r dr = 4\pi \rho_{0,\text{DM}} R_s^3 \left[\frac{R_s}{r + R_s} + \ln(r + R_s) \right], \quad (5.2)$$

which, trivially assuming a potential

$$\Phi(r) = -\frac{G M_{\text{cum}}}{r}, \quad (5.3)$$

leads to a form of potential which allows the baryonic density and pressure to converge at high radii:

$$\Phi_{\text{conv}}(r) = -\frac{4\pi G \rho_{0,\text{DM}} R_s^3}{r} \left(\frac{R_s}{r + R_s} + \ln(r + R_s) \right). \quad (5.4)$$

Our system comprises only a low mass; assuming a dark matter background density $\rho_{0,\text{DM}} = 1 M_{\text{P}} \text{ cm}^{-3} = 1.7 \times 10^{-24} \text{ g cm}^{-3}$, and a scale radius of $R_s = 2.5 \text{ kpc}$, the cumulative mass at 25 kpc radius amounts to a total of $7.3 \times 10^9 M_{\odot}$. This includes the mass of the disc, of which we calculate the gas density distribution below. The baryonic density distribution in the halo is now obtained using equation (4.1),

$$\rho_{\text{b}}(r, \theta) = \rho_0 \exp \left(-\Phi_{\text{tot}}(r, \theta) \frac{0.59 M_{\text{P}}}{\text{k}_B \text{ T}} \right), \quad (5.5)$$

Table 5.2: External potential parameters for simulation set 2 (CD and ED runs).

Component	Parameter	Value
Bulge	r_{C_1}	0.9 kpc
	M_{C_1}	$7.59 \times 10^7 M_\odot$
	r_{C_2}	0.14 kpc
	M_{C_2}	$4.05 \times 10^8 M_\odot$
Disc	b	0.1 kpc
	a_1	1.94 kpc
	M_{D_1}	$1.67 \times 10^9 M_\odot$
	a_2	5.81 kpc
	M_{D_2}	$-7.34 \times 10^8 M_\odot$
	a_3	11.62 kpc
	M_{D_3}	$8.35 \times 10^7 M_\odot$

with Φ_{tot} now being $\Phi_{\text{disc}} + \Phi_{\text{cent}} + \Phi_{\text{conv}}$. We now choose the values $\rho_0 = 3.4 \times 10^{-30} \text{ g cm}^{-3}$ for the convergence value of the gas density, and $4.8 \times 10^5 \text{ K}$ for the overall halo temperature. The pressure, finally, is obtained again from the ideal gas equation (2.61).

5.2.2 Disc setup

The disc setup is basically the same as described in Subsection 4.2.2, however, with different parameters. Our intention is to simulate a low-mass disc galaxy, comparable in mass to the LBGs observed at redshift $z = 3 - 4$. We scale down the length-related parameters used by Flynn et al. [1996] by a factor of 1/3, and the mass-related ones by a factor of 0.025. The exact values are given in Table 5.2.

The gas density in the disc is obtained via

$$\rho_{\text{disc}}(r) = \rho_{\text{disc},0} \exp\left(-\frac{r}{r_{\text{s,D}}}\right), \quad (5.6)$$

with $r_{\text{s,D}}$ being the disc scale radius, and $\rho_{\text{disc},0} = 3.5 \times 10^{-23} \text{ g cm}^{-3}$. The density profile

is cut off at an outer radius of 3.3 kpc. The disc has a vertical height of 250 pc, giving it a total gas mass of $1.38 \times 10^9 M_{\odot}$, which is about 90 per cent of the mass implied by the disc potential. The disc gas pressure follows from the ideal gas equation (2.61), just as for the halo gas pressure.

As an alternative to the exponential distribution, one could use a constant gas density profile. This special type of gas disc profile has been observed e.g. by Bendo et al. [2010] in NGC 2403, and is investigated here in Section 5.4. If we choose the disc gas density to be constant for all radii and keep its total gas mass, we obtain an overall value of $\rho_{\text{disc}}(r) = \rho_{\text{disc}} = 5.5 \times 10^{-24} \text{ g cm}^{-3}$. In particular, this setup is used exclusively in simulations CD-1, CD-3, CD-4, CD-1R, CD-3R and CD-4R. By comparing exponential gas distributions to constant ones, we attempt to capture the extreme cases of gas-rich galactic discs.

5.3 Clustering of SN events

We found in the last chapter, that due to the spherical grid geometry, the outer disc cells tend to enclose higher masses of gas, which imposes a bias on the local star formation recipe we use. It is e.g. possible that a number of smaller cells close to the disc centre release several events spread out in time but each event being too weak to contribute significantly to an outflow; on the other side, a contiguous region of smaller cells as a whole could release an event powerful enough to escape the disc. These circumstances call for modifications in the probability function calculating the likelihood of each cell to trigger SNe. To reduce the spreading in time from a multitude of small to fewer and larger ones, we need to introduce a factor, which, on the one hand, reduces the SN event probability for a cell, but on the other increases the event strength by the same amount. A further option to resolve the cell size bias would be to expand the factor by a r^{-2} -term that accounts for the cell volume increase with radius, essentially making it a function inversely proportional to the square of the radius r , given in kpc, which we call the clustering function $\zeta(r) = \text{const} \cdot (r/\text{kpc})^{-2}$. The probability for one cell to release a SN event thus becomes

$$P_{\text{SN,loc}} = \frac{\rho_{\text{cell}} V_{\text{cell}}}{100 M_{\odot}} \cdot \epsilon_{\text{SF}} \cdot \frac{\delta t}{t_{\text{dyn}}} \cdot \zeta(r), \quad (5.7)$$

whereas the number of SNe per event, the total energy released and the mass converted

into stars are each multiplied by the factor $\zeta(r)$. This may occasionally lead to a lack of mass available especially in the innermost cells. However, since we assume a star formation efficiency $\epsilon_{\text{SFR}} = 0.3$, $\zeta(r) < 3.3$ is generally unproblematic. For a constant $\zeta = 4$, the SN events would require a 1.2 times higher local gas mass. In the course of one run, we have counted roughly 400 SN events, which is one in 40 disc cells triggering SNe. The disc will hence face a gas deficit of 0.5 per cent only, which should not significantly change the disc dynamics. In case of $\zeta \propto r^{-2}$, the inner cells would require several times higher gas masses. On the other hand, the excessive gas mass in the outer disc (i.e. > 1.1 kpc for $\zeta = 4r^{-2}$ and $\epsilon_{\text{SFR}} = 0.3$) will easily over-compensate the deficit to the total disc mass budget. Our simulation set includes the following runs: a gas disc with constant density profile and without the factor ζ in the probability function (i.e. $\zeta = 1$; denoted “CD-1”), is compared to two runs with identical disc setup (denoted “CD-3” and “CD-4”), in which ζ is a constant factor of 3 and 4, respectively, in order to study the effects of a temporal SN event clustering alone. Further, it encompasses three runs CD-1R, CD-3R and CD-4R, where we then cancel out the cell bias by setting $\zeta = \zeta(r)$ to r^{-2} , $3r^{-2}$ and $4r^{-2}$, respectively (see Table 5.1).

Our first point of interest is the effect of feedback on the shape of the disc-halo system. Simulation CD-1 features no modification of the star formation recipe, however, due to the constant density distribution of disc gas, violent star formation and hence feedback occurs in the outer disc parts. As a result, the disc becomes highly turbulent and unstable in the outer region (compare Figure 5.2, upper panel) after 25 Myr. Early on, an outflow evolves on only one side of the disc, which is strong enough to cross the outer boundary of the simulation domain at 10 kpc. The asymmetric nature of the outflow indicates that the system is just on the brink of being capable to exhibit outflows. This assumption is supported by comparison to simulation CD-1R (Figure 5.2, lower panel), where star formation is shifted toward the inner disc regions by the clustering function $\zeta = r^{-2}$. Star formation in both simulations are within the same order of magnitude, however, in run CD-1R the notably weaker feedback in the outer disc does not affect the disc stability. On the other hand, even a slightly higher feedback in disc regions at $r < 1$ kpc does not trigger an outflow. We find weak shock fronts expanding into the halo, but substantial outflows or even a constantly blowing wind are absent. Figure 5.3 shows the outflow velocities in both runs, compared to the local sound speed. None of the outflows are supersonic, and regions where material falls back into the disc are common.

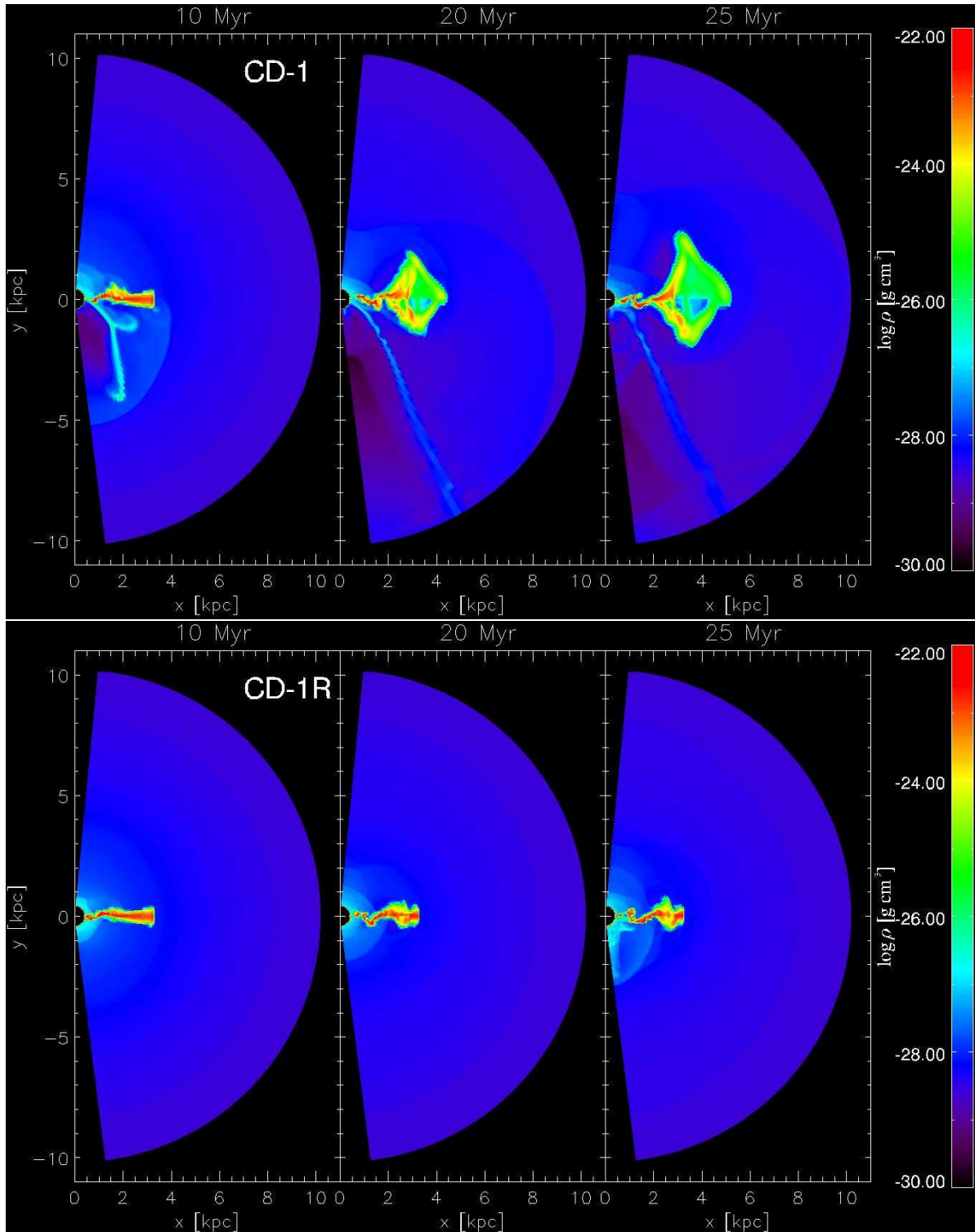


Figure 5.2: Simulations CD-1 (*top row*) and CD-1R (*bottom row*). The elapsed time is denoted above each snapshot. Shown is the logarithm of mass density in meridional midplanes.

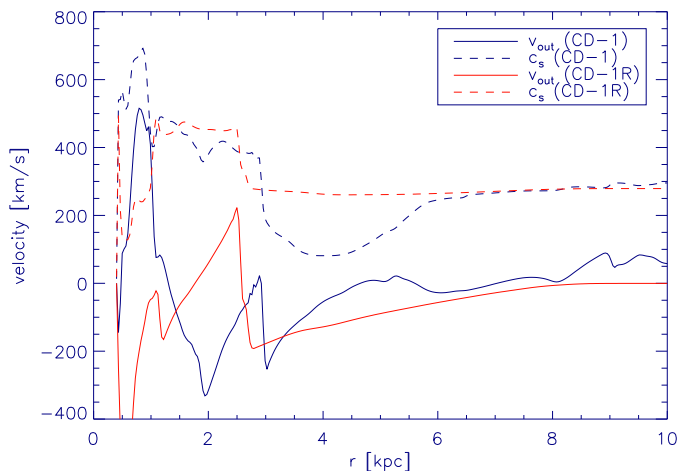


Figure 5.3: Outflow velocities v_{out} (solid lines) compared to local sound speed c_s (dashed lines) in simulations CD-1 (blue) and CD-1R (red), respectively. The plot shows a radial cut through the profile at $\theta = 0.91\pi$, after 25 Myr.

Run CD-3 reduces SN probability for every cell by a factor of 3, while increasing event strength by the same amount. In Figure 5.4 we can see that the outer disc is violently blown apart by massive forces due to feedback early on. The inner disc gives rise to stellar feedback strong enough to set up considerable outflows, initiated by two superbubbles expanding into the halo on both sides of the disc and sweeping a path through the halo. They leave behind a rarefied region of conical shape, which gives less resistance to subsequent bubbles than the initial halo gas. Other than in CD-1 and CD-1R, the first bubbles are followed by several others of comparable strength. CD-3R shows the same result, however the outer disc remains intact. This is due to the clustering function $\zeta = 3r^{-2}$; cells at radii larger than $\sqrt{3}$ kpc now face a larger probability of a SN event, while the event strength is reduced accordingly. Therefore, the outer disc in CD-3R is turbulent, but not disrupted. Figure (5.5) reveals that the outflows are exceeding the sound speed by a large factor in both CD-3 and CD-3R, meaning that the outflowing material likely reaches the escape velocity.

Runs CD-4 and CD-4R are displayed in Figure (5.6). The respective clustering functions are $\zeta = 4$ for CD-4, and $\zeta = 4r^{-2}$ for CD-4R. The geometry of the outflows and the stability of the discs compare to those found for CD-3 and CD-3R, respectively. Again, strong SN bubbles in the inner disc give rise to subsequent shock waves escaping the disc, and in CD-4R the disc is widely destroyed due to the efficient feedback in

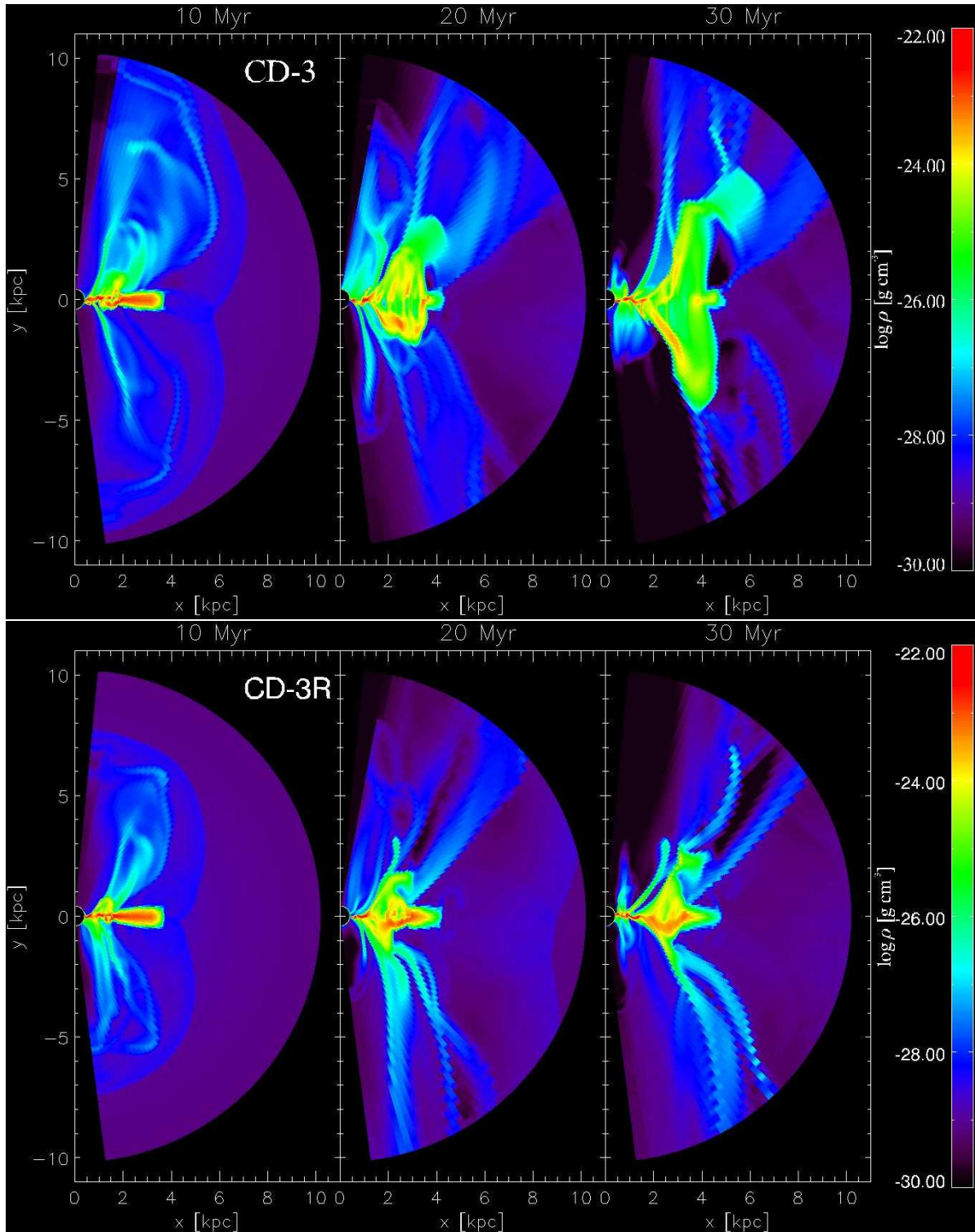


Figure 5.4: Simulations CD-3 (*top row*) and CD-3R (*bottom row*). The elapsed time is denoted above each snapshot. Shown is the logarithm of mass density in meridional midplanes.

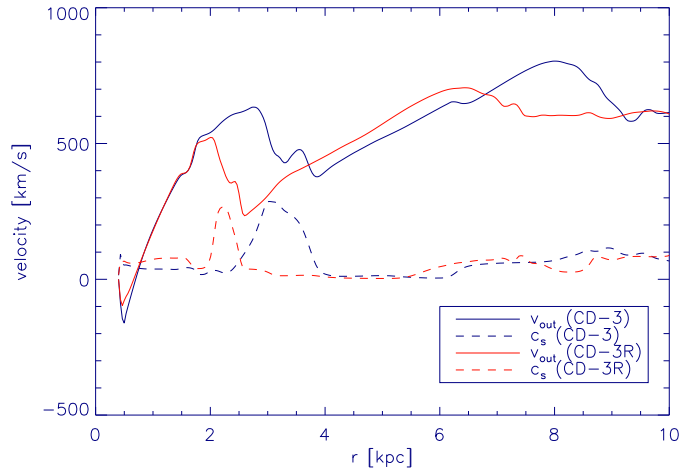


Figure 5.5: Outflow velocities v_{out} (solid lines) compared to local sound speed c_s (dashed lines) in simulations CD-3 (blue) and CD-3R (red), respectively. The plot shows a radial cut through the profile at $\theta = 0.91\pi$, after 30 Myr.

its outer regions. However, the velocity of the outbound material (Figure 5.7) points out some difference to simulations CD-3 and CD-3R: Here, only CD-4R shows a clearly supersonic outflow, which, in the outermost parts of the simulation domain, comes close to 1000 km s^{-1} . CD-4 exhibits both regions where outflow is subsonic and regions of supersonic outflow velocity. In CD-4R, star formation from 1 kpc inwards increases to higher values compared to CD-4. Since both discs share the same density profile, we would indeed expect faster outflow velocities in CD-4R (compare also Section 5.5)

We can hence outline some clear trends from all six CD runs. First of all, more clustered energy input, which occurs for values of $\zeta > 1$, proves beneficial for the emergence of an outflow, which can be seen by comparing CD-1 and CD-3. On the other hand, the reduction of superbubbles in size, which happens in the outer disc where $\zeta < 1$, prevents feedback from being too efficient. Especially in CD-3 and CD-4, disc stability is heavily disturbed as a result of the massive SN events arising in the larger, outer disc cells. Secondly, stronger SN events likely account for stronger and faster outflows, as is affirmed by the velocity profiles of CD-1R, CD-3R and CD-4R. A certain amount of clustering of SN events is however required to allow the bubbles to escape the disc, since in CD-1R there is not even a continuous outflow, indicating that escaping bubbles develop only occasionally if provoked by a large number of comparatively small events. Since the clustering function does not affect the averaged total of SN events in the disc over a

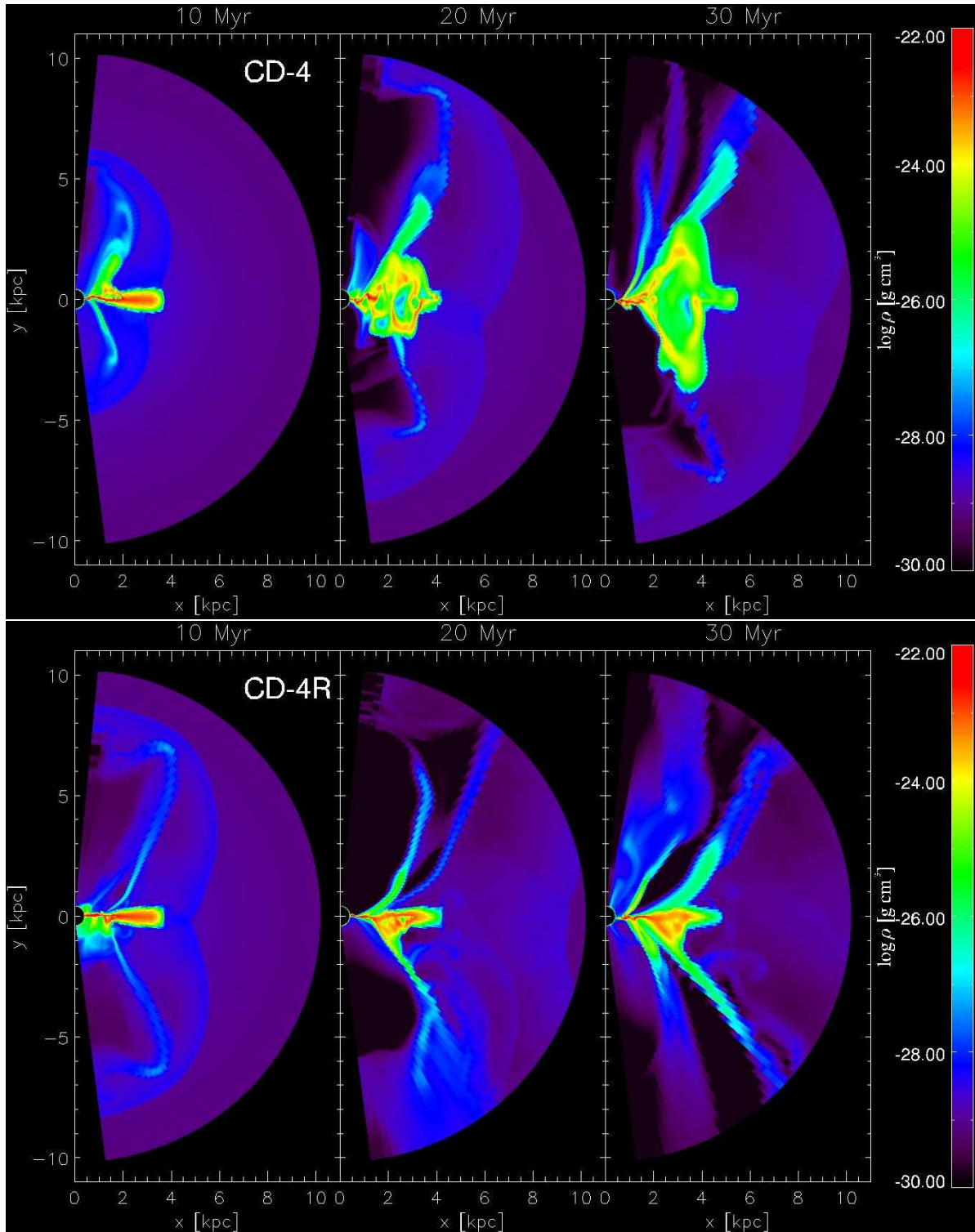


Figure 5.6: Simulations CD-4 (*top row*) and CD-4R (*bottom row*). The elapsed time is denoted above each snapshot. Shown is the logarithm of mass density in meridional midplanes.

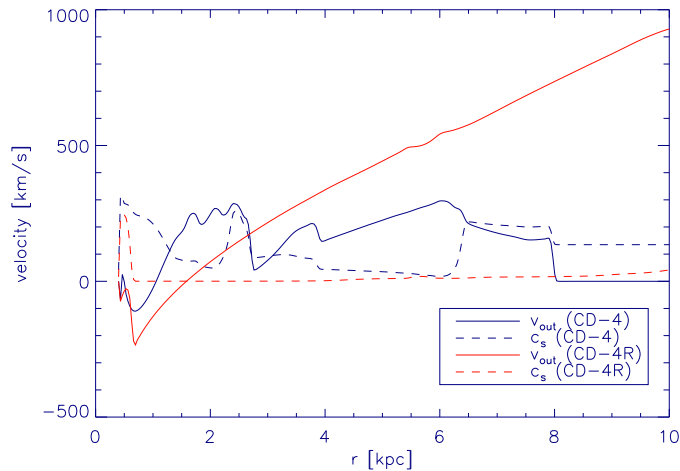


Figure 5.7: Outflow velocities v_{out} (solid lines) compared to local sound speed c_s (dashed lines) in simulations CD-4 (blue) and CD-4R (red), respectively. The plot shows a radial cut through the profile at $\theta = 0.91\pi$, after 30 Myr.

given time span, we expect outflows to be stronger in those runs where the disc remains intact: If less energy is dissipated into the outer disc, more energy will be released close to the centre, where larger bubbles will give rise to a faster outflow. This expectation is met in the runs CD-4 and CD-4R, while CD-3 and CD-3R show no clear difference in their outflow velocity.

It should be made clear however, that the clustering function does only alter the average number of SNe per bubble. By shifting the trend from smaller and more frequent to larger and less frequent events if larger than unity, and vice versa if less, the average bubble becomes larger towards the disc centre and smaller outwards. The effects provoked by the bubble size on the outflow are again discussed in Section 6.6, where bubble sizes are a preset number for every simulation.

5.4 The disc density profile

We have seen in the previous section that efficient feedback, especially in the outer limb of the disc, can disturb disc stability enough to cause partial disruption of the system. Temporally spreading the SN events can avert this effect, but in the first place our SN event sizes are determined by cell mass and hence gas density. It seems possible that the disc must not necessarily dissolve as a result to strongly clustered SN events,

but that a reduced density of the outer disc regions may suffice to keep the system stable.

The simulations with $\zeta = 3$ and $\zeta = 4$ have both been repeated with an exponential density distribution, as is described in Section 5.2. Figure 5.8 displays the runs ED-3 and ED-4 at different simulated times, respectively. Interestingly, we find that in ED-3 large portions of gas from the disc are shifted away from the midplane in both directions due to feedback at 20 Myr, but the gas partially settles back into its original position at 30 Myr. This may be the limiting case where feedback is just barely insufficient to disrupt the disc. The system also features a highly supersonic outflow (compare Figure 5.9), whereas the entrained filaments are fewer and larger as e.g. in CD-3R. Run ED-4 does not feature an outflow on the other hand, which is an indicator for the large superbubbles capable of first launching the outflow to occur only occasionally. Only a small region in between 4 and 5 kpc shows supersonic outflow movement. Instead, the disc in ED-4 is blown apart again, as a result of stronger clustering in comparison to ED-3.

If we compare the runs ED-3 and ED-4 to CD-3 and CD-4, we actually find, that the exponential density distribution reduces the instability in the outer disc, but if clustering is strong enough, the effect becomes too weak at some point. Stronger temporal clustering of SN events still has a negative effect on disc stability in the outer parts. On the contrary, in the inner parts, stronger clustering should lead to faster, more violent outflows, independent of the inner disc gas density (note that higher density and hence mass results in larger SN events, but outflow velocity remains constant due to $E \propto M$). The absence of such outflows in ED-4 may be a statistical effect and might set in at a later point in time. Supersonic outflows nevertheless appear in ED-3, at a notably higher velocity than in CD-3, which confirms our assumption. Conclusively, we find that the disc density profile does not affect the overall outflow dynamics as much as the clustering function. Since an exponential gas disc contains more mass in its innermost kpc than a disc of constant density and equal mass, large events should happen more frequently in an exponential disc. However, as we have seen from the simulations in this chapter, it seems to be of more importance that large bubbles comprising many SNe develop at all; a high value for the clustering function ζ can hence well compensate a lower density.

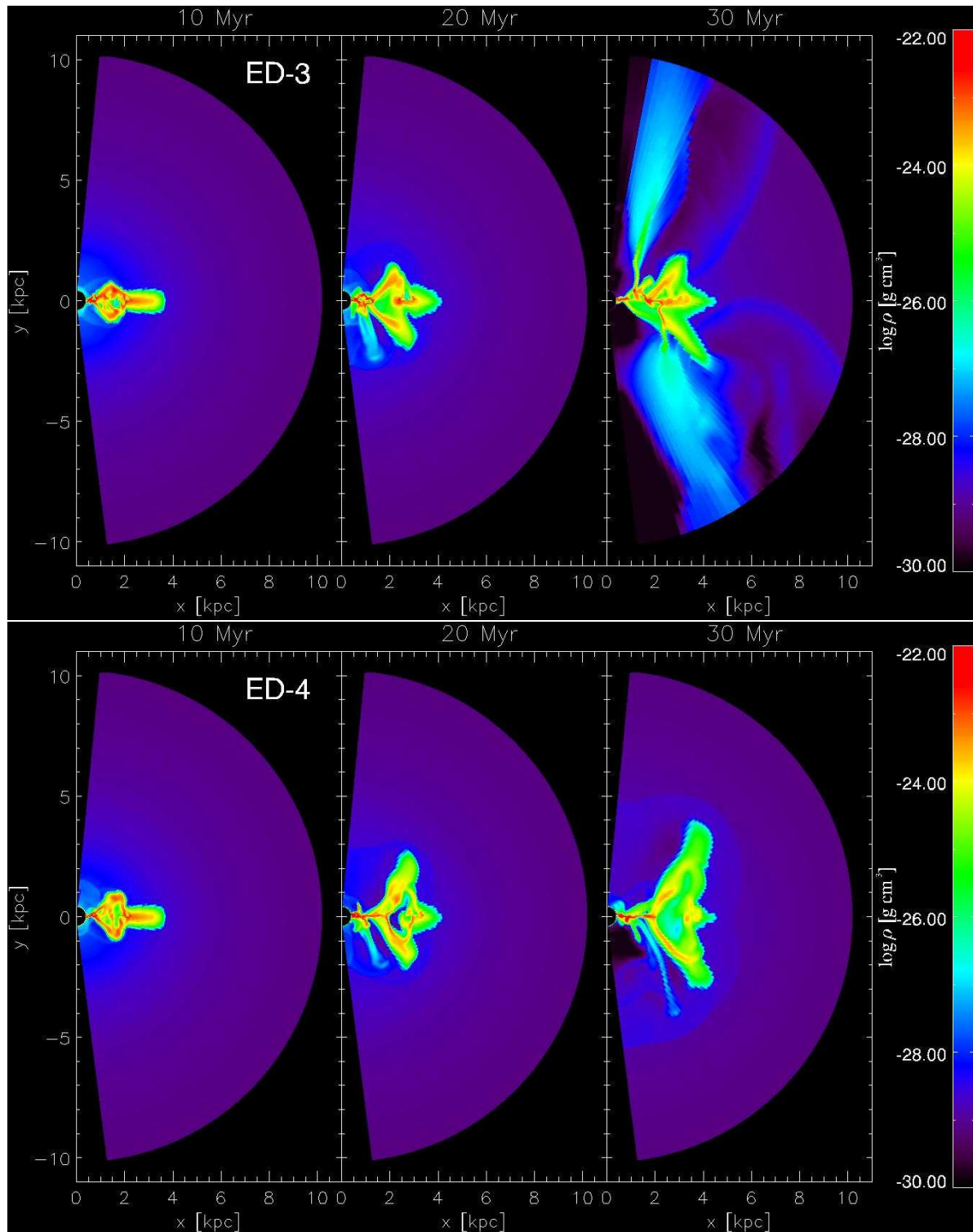


Figure 5.8: Simulations ED-3 (*top row*) and ED-4 (*bottom row*). The elapsed time is denoted above each snapshot. Shown is the logarithm of mass density in meridional midplanes.

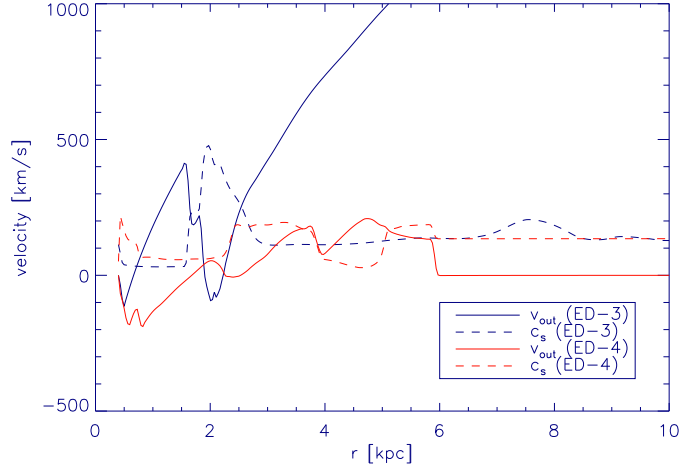


Figure 5.9: Outflow velocities v_{out} (solid lines) compared to local sound speed c_s (dashed lines) in simulations ED-3 (blue) and ED-4 (red), respectively. The plot shows a radial cut through the profile at $\theta = 0.91\pi$, after 30 Myr.

5.5 Implications

The presented simulations so far have proven capable not only of launching strong, supersonic outflows; in some cases even a continuous flow of material from the disc far into the halo could be established. This vigorous outflow is likely facilitated by the chosen system setup; we have a low-mass disc which is very rich in gas, making up about 90 per cent of the total disc mass. High-density regions, like filaments entrained by outflowing bubbles, or even disc fragments can easily escape the potential. Our potential was chosen in a way that, though generally shallow due to the low-mass disc, it has a steep slope close to its centre, but flattens out quickly towards higher radii.

As expected, the initially steep halo profile proves to be an inhibitor for outflows in several cases. Run ED-4 and CD-1 show no signs of superbubbles entirely escaping the disc, whereas in run CD-1R not even substantial SN clustering can overcome the steep potential slope. However, on the other hand, we see winds in the other simulations (CD-3, CD-3R, CD-4, CD-4R and ED-3) which do not only reach supersonic velocities, but also cross the edge of our simulation box. There is no case in which bubbles escaping from the disc are eventually stopped as a result of thermal halo pressure, which converges at larger radii, providing a near-constant opposing force. However, comparison to run F-ST in the previous chapter yields some information: The more shallow potential slope at low radii in the logarithmic halo suggested by Flynn et al. [1996] did

not lead to a continuous outflow in the case of F-ST; the initially steep profile chosen in this chapter however allowed strong outflows with numerous filaments in several runs. Steep potential slopes should in fact oppose the dense filaments in escaping the gravity of the system. It is therefore thinkable that not only the potential of the halo, but also the disc mass is crucial to outflows. The setup in Chapter 4 featured a mass-rich Milky Way-like disc, whereas the current setup comprises just a low-mass disc. In the next setup we will investigate a configuration where disc mass is of order $10^{10} M_{\odot}$. We should then be able to witness the limiting case where bubbles and filaments escape the disc, but are not powerful enough to be blown away entirely, and eventually fall back.

By implementing the function ζ , we could study the effect provoked by different degrees of SN event clustering on the outflows. Higher clustering at all disc radii has been found to result in higher feedback activity for most cases; in the disc centre this feedback causes a strong, continuous wind, whereas the outer disc is at least partially disrupted. If clustering is dependent on the radius, and $\zeta(r)$ strongly clusters SN events at low radii but essentially has the opposite effect of spreading out SN events at high radii, the outer disc will remain stable, while at the centre winds still form.

The disc density profile, however, proved to have only little influence on the results. This can easily be shown as follows: Increasing disc density by a given factor in a large region leads to larger SN events providing a higher amount feedback energy by just that same factor. If we further assume that most large bubbles originate deep within the disc, the overlying, more massive material will also require more energy to be driven out and form the characteristic filaments. Due to the feedback energy E being proportional to mass M , the outflow velocity $v = \sqrt{2E/M}$ will stay just the same as for a comparable region of lower density. Our simulations with exponential disc density profiles confirm that there is no systematic deviation from those with constant disc density profile.

However, our resolution tests have shown that reasonable star formation rates are only possible for a narrow range of resolutions, which is a consequence of the locally determined SF recipe used here. We will investigate in Chapter 6 how to implement a SF law that avoids resolution dependence and in fact resembles a Kennicutt-Schmidt like prescription, which is commonly found in disc galaxies.

Chapter 6

Galactic winds in a NFW halo

6.1 Preconsiderations

We have already considered two possible launching mechanisms for galactic outflows in Chapter 4. Their presumable effects have been explained thoroughly in Section 4.1. Firstly, we argued that overpressured SN superbubbles may be capable of expanding out of the disc and expanding far into the halo, thus sweeping a path for later bubbles which will then continuously drive a galactic wind. An investigation of this theory involves the resolution of a multiphase ISM in our models. Secondly, we considered kinetic feedback from SNe alone to play a key role, as it might be just providing enough energy to drive a galactic wind kinetically. However, the high disc mass in the corresponding simulation F-KE proved to be a major obstacle to drawing a definite conclusion on this matter. In this chapter we hence modify the setup once more to achieve more reliable results. The details on the setup are explained in the following section. Furthermore, we make use of the star formation recipe explained in subsection 3.4.2, which is based on the Kennicutt-Schmidt law, since local star formation criteria have proven to result in different SFRs for different resolutions.

Additional candidates for wind driving mechanisms are also taken into consideration. The development of buoyant SN bubbles, in reality as well as in our models, will be subject to discussion in this chapter. Since the new star formation recipe involves a preset size of single events (i.e. the number of single SNe forming one superbubble), we also examine the question if this bubble size makes a difference to the outcome. In Chapter 5 we provided the clustering function $\zeta(r)$, which essentially increased the average bubble size while reducing their probability. We found that temporally clustering

several small bubbles into fewer large ones proves effective in triggering outflows. In order to cross-check this result, several additional simulations with various bubble sizes involving star formation with the Kennicutt-Schmidt-based prescription are conducted in this chapter.

We begin with an investigation how the method of SN energy injection affects the emerging wind. For this purpose, we have run a set of simulations with $\zeta_0 = 100$. One simulation uses the Sedov-Taylor blast wave model, and hence both kinetic and thermal energy are injected with every SN event (denoted “ST100”). In addition, two more models injecting a purely thermal energy fraction of 40 per cent (denoted “TE0.4”), and 60 per cent (“TE0.6”) of the total SN energy yield, respectively, and another one, injecting a purely kinetic energy fraction of 40 per cent (“KE0.4”), have been made. The characteristics of the pressure-driven and the kinetic energy driven cases are discussed in the first two subsections, respectively.

The third subsection includes an analysis about the contribution of buoyancy to the wind energy in ST100, which will be compared to our theoretical consideration in Subsection 6.1.1.

All the runs presented in Sections 6.3, 6.4 and 6.5 include a cooling halo. Since halo pressure is reduced by cooling, winds will arise comparatively easily in this case, allowing for more prominent effects more suitable for later comparison. Section 6.6 investigates the question how the sizes of SN bubbles can affect the strength of galactic winds; for this we have run another set of three simulations featuring Sedov-Taylor blast wave models and different event sizes each. In contrast to the previous runs, the runs in subsection 6.6 are each performed twice, with both a cooling and a non-cooling halo, respectively, to investigate the limiting cases of the possible effects of varying metallicities in such objects. We show that the different halo pressure has a significant effect on the wind. All of our results herein will then be compared in the final section.

6.1.1 Buoyancy of supernova bubbles

An interesting physical quantity is the entropy index S . Here, we calculate S at relevant locations within the underlying NFW halo at redshift $z = 3.5$. The entropy index is defined as

$$S = \frac{p}{n^\gamma}, \quad (6.1)$$

where n is the number density of particles, the units of S being given in keV cm^2 . Generally, a bubble with an entropy index higher than its environment will experience a buoyant force, meaning that with S being known everywhere, we can easily determine the height a buoyant bubble can reach.

With the pressure expression from equation (2.61), the entropy index S transforms into

$$S = \frac{k_{\text{B}} T}{n^{\gamma-1}}. \quad (6.2)$$

Let us consider a bubble produced by a single SN in an early state of evolution. The entropy index is highest within the central hot gas phase of the bubble, and this is the region most relevant regarding buoyancy. Note that S is defined such that during the process of adiabatic expansion it is not going to change over time. For the hot bubble interior, S may decrease due to mixing and cooling. Cooling times are long compared to the simulation time, and mixing shall be neglected here in the first instance. This in turn means that the phase of evolution in which we investigate a bubble does not matter all too much. Since the rarefied, hot bubble interior has a very long cooling timescale, cooling is not significant here. A typical SN will release about 10^{51} erg of energy. From the equation of motion for a blast wave in the thin shell approximation, it follows that 60 per cent of this energy will be in the form of thermal energy. Implying an ejecta mass of $8 M_{\odot}$ and a bubble in an advanced state, e.g. with a radius of 10 pc to start with, the density will be of order $0.1 M_{\text{p}} \text{cm}^{-3}$. It follows then, assuming a temperature of 10^8 K, that the entropy index from equation (6.2) reaches several 10 keV cm^2 . Given a typical entropy index for the gas disc of order 10^{-4} keV cm^2 , the former value is certainly enough to raise the bubble away from the disc midplane into the disc-halo transition region. In our example, the values for $S(r_{\text{s}})$ and $S(r_{\text{vir}})$ in the halo amount to 9.1 keV cm^2 and 21.2 keV cm^2 , respectively. Hence S inside a bubble formed by several SNe will be typically high enough to exhibit buoyancy effects within the halo at least at low radii. This conclusion might however be affected by the (unknown) mixing of the different ISM phases. In our simulations, we include the buoyancy effect of the superbubbles. We inject the bubbles with even higher entropy index (compare Section 6.5 below), because numerical mixing - we have to inject the superbubble on a scale of a few grid cells - strongly reduces the entropy index. The energetic effect of buoyancy is however likely minor: While ascending, the bubble will vastly increase in size due to the radially exponentially decreasing environment pressure, thus allowing for its density to drop to negligible values compared to the inner halo environment. Because of the latter, buoyancy in the halo will likely affect only superbubbles in an advanced state of evolution, where their diameter has already grown up to the order of 100 pc. In that

case, the acquired energy during ascension will be

$$E_{\text{asc}} = \rho_{\text{halo}} V_{\text{bubble}} g_{\text{halo}} h, \quad (6.3)$$

where ρ_{halo} is the halo density, g_{halo} its gravitational acceleration, V_{bubble} the bubble volume and h the height of ascension. In particular, a 100 pc-bubble will acquire some 10^{47} erg of energy while ascending 1 kpc. We shall keep these interim results in mind for comparison with our simulations.

6.1.2 Resolution

We have again investigated the resolution dependence of the SFR (see Chapter 7 below for a discussion of the dependence of the outflow rates on resolution), varying the reference resolution at $r = 1$ kpc radius from 16 pc to 65 pc (R16 - R65, compare Table 6.1) for a standard simulation.

Assuming one SN in $100 M_{\odot}$ of stars formed, we find the SFR in our $10^{10} M_{\odot}$ system at all resolutions to be about $10 M_{\odot} \text{yr}^{-1}$, yielding an SFR per unit mass of 10^{-9}yr^{-1} . As a comparison, this is several ten times the SFR per unit mass in the Milky Way, which would be of a few 10^{-11}yr^{-1} . Our SFR is therefore in the relevant range; e.g. Pettini et al. [2001] observe values of about $10 - 70 M_{\odot} \text{yr}^{-1}$ for their sample of $10^{10} M_{\odot}$ -LBG's at redshift $z \sim 3$, which, accordingly, would result in an SFR several 10^{-9}yr^{-1} per unit mass (or a few 10^{-1} SNe per year). The overall SN rates of our model galaxy are displayed in Figure 6.1 for all resolutions. The graph for 65 pc resolution shows the strongest deviation, indicating that too coarse resolutions will notably affect the star formation rate. All graphs agree within 26 per cent, however, if we regard only resolutions of 36 pc and finer, the error reduces to nine per cent.

6.2 Setup and initial conditions

6.2.1 Halo setup

LBGs with winds typically occur at redshifts between 3 and 4 (compare Chapter 1). Let us therefore consider a NFW halo in hydrostatic equilibrium at redshift $z = 3.5$. The

Table 6.1: Simulation parameters for simulation set 3 (ST, KE, TE, B and NC runs).

Run	Resolution	SN energy ^a		Event size ζ_0	Residual density ^b	Halo cooling
		E_{kin}	E_{therm}			
R16	16 pc	40 %	60%	100 SNe	$10^{-28} \text{ g cm}^{-3}$	yes
R30	30 pc	40 %	60%	100 SNe	$10^{-28} \text{ g cm}^{-3}$	yes
R33 ^c	33 pc	40 %	60%	100 SNe	$10^{-28} \text{ g cm}^{-3}$	yes
R36	36 pc	40 %	60%	100 SNe	$10^{-28} \text{ g cm}^{-3}$	yes
R65	65 pc	40 %	60%	100 SNe	$10^{-28} \text{ g cm}^{-3}$	yes
ST20	33 pc	40 %	60%	20 SNe	$10^{-28} \text{ g cm}^{-3}$	yes
ST50	33 pc	40 %	60%	50 SNe	$10^{-28} \text{ g cm}^{-3}$	yes
ST100	33 pc	40 %	60%	100 SNe	$10^{-28} \text{ g cm}^{-3}$	yes
ST200	33 pc	40 %	60%	200 SNe	$10^{-28} \text{ g cm}^{-3}$	yes
KE0.4	33 pc	40 %	0%	100 SNe	$10^{-28} \text{ g cm}^{-3}$	yes
TE0.6	33 pc	0 %	60%	100 SNe	$10^{-28} \text{ g cm}^{-3}$	yes
TE0.4	33 pc	0 %	40%	100 SNe	$10^{-28} \text{ g cm}^{-3}$	yes
B100	33 pc	40 %	60%	100 SNe	$10^{-27} \text{ g cm}^{-3}$	yes
NC20	33 pc	40 %	60%	20 SNe	$10^{-28} \text{ g cm}^{-3}$	no
NC50	33 pc	40 %	60%	50 SNe	$10^{-28} \text{ g cm}^{-3}$	no
NC100	33 pc	40 %	60%	100 SNe	$10^{-28} \text{ g cm}^{-3}$	no
NC200	33 pc	40 %	60%	200 SNe	$10^{-28} \text{ g cm}^{-3}$	no

^aThe energy released by a SN event is subdivided into a kinetic and a thermal component.

^bThe term 'Residual density' refers to the density left over in a cell after being subject to a SN event.

^c"R33" and "ST100" are two denotations for the same run.

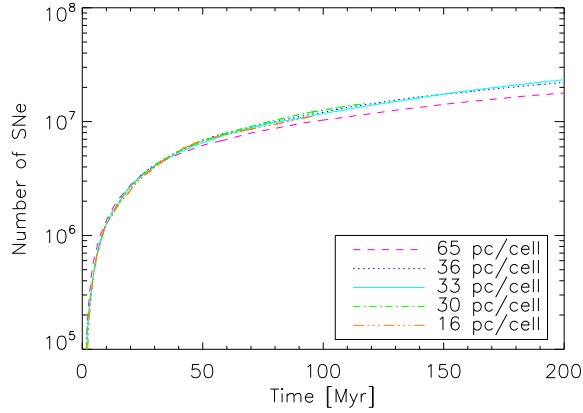


Figure 6.1: Cumulative supernova rate at a given time for our standard run at different resolutions (R16 - R65, compare Table 6.1).

critical background density of baryons in the intergalactic medium (IGM), $\rho_{\text{crit,b}}$, can be obtained via

$$\rho_{\text{crit,b}} = \frac{3\Omega_{\text{B}}H(z)^2}{8\pi G} \quad (6.4)$$

[Ohta, Kayo and Taruya 2003], where

$$H(z)^2 = H_0^2 (\Omega_{\text{M}}(1+z)^3 + \Omega_{\text{k}}(1+z)^2 + \Omega_{\Lambda}), \quad (6.5)$$

with $\Omega_{\text{k}} = -0.02$. For a flat Lambda Universe it follows from the Friedmann equations that

$$\Omega_{\text{M}}(z) = \frac{\Omega_{\text{M},0}}{\Omega_{\text{M},0} + \frac{1-\Omega_{\text{M},0}}{(1+z)^3}}. \quad (6.6)$$

Using the present-day parameters of $\Omega_{\text{b},0} = 0.044$ and $\Omega_{\text{M},0} = 0.27$ one obtains $\Omega_{\text{M}}(z = 3.5) = 0.97$ and $\Omega_{\text{b}}(z = 3.5) = 0.16$, which, by combining equations (6.4) and (6.5), yields $\rho_{\text{crit,b}} = 1.4 \times 10^{-28} \text{ g cm}^{-3}$.

By choice, the model system shall have a virial radius $r_{\text{s}} = 25 \text{ kpc}$. With $r_{200} = 0.94 r_{\text{vir}}$ at $z = 3.5$, this immediately yields a scale radius $r_{\text{vir}} = 4r_{\text{s}} = 5.9 \text{ kpc}$ by invoking a value for the concentration parameter $c_{200} = r_{200}/r_{\text{s}} = 4$, which is verified by Zhao et al. [2009] for our underlying redshift. The baryonic mass confined within r_{200} may be pinned down via the critical baryon density, $\rho_{\text{crit,b}}$, to a value of $M_{200,\text{b}} = 2.2 \times 10^{10} M_{\odot}$. As mentioned above, we assume that the initial halo is in hydrostatic equilibrium, and isothermal, suggesting a radially exponential distribution of baryonic matter (equation (2.59)):

$$\rho_{\text{b}}(r, \theta) = \rho_{\text{crit,b}} \exp\left(-\Phi_{\text{tot}}(r, \theta) \frac{0.59 M_{\text{P}}}{k_{\text{B}} T}\right) \quad (6.7)$$

where M_{P} is the proton mass, and

$$\Phi_{\text{tot}}(r, \theta) = \Phi_{\text{disc}}(r, \theta) + \Phi_{\text{cent}}(r) + \Phi_{\text{NFW}}(r), \quad (6.8)$$

with

$$\Phi_{\text{NFW}} = -\frac{G M_{200}}{r_{\text{s}} f(c_{200})} \frac{\ln(1 + r/r_{\text{s}})}{r/r_{\text{s}}} \quad (6.9)$$

being the NFW potential dominating at large radii. Both the disc and the central bulge potential components have already been explained in Section 3.7. The density distribution according to equation (6.7) is visualised in Figure 6.3. The isothermal halo has a temperature $T = 6.0 \times 10^5$ K, the density ρ_{b} at the inner edge $r = 0.4$ kpc does not exceed typical disc density values, which are of order 10^{-24} g cm $^{-3}$. By integrating the now well-defined baryonic density profile, we obtain a baryonic mass of $1.0 \times 10^9 M_{\odot}$ being situated in the hot halo. The larger part of $M_{200,\text{b}}$, still amounting to $2.1 \times 10^{10} M_{\odot}$, must therefore be considered to have settled into the disc. With the halo density ρ_{b} given for all radii, the halo pressure p results from the ideal gas equation (2.61)

$$p = n_{\text{b}} k_{\text{B}} T. \quad (6.10)$$

The task of constructing an isothermal halo in hydrostatic equilibrium is encumbered by the condition that its density should converge against a certain background value as described above. A halo potential of the form

$$\Phi_{\text{DM}} = \frac{v_{\text{rot}}^2}{2} \ln \left(\left(\frac{r}{\text{kpc}} \right)^2 + \left(\frac{r_{\text{s}}}{\text{kpc}} \right)^2 \right) \quad (6.11)$$

given by a constant rotational velocity v_{rot} for large r , as described by Flynn et al. [1996] has been tested in Chapter 4, however, this model entails the fact that the halo pressure will not converge. This means first of all that shock fronts could theoretically proceed to infinity as due to the resistant pressure decreasing strongly with r they will accelerate forever. Furthermore, the density would have to drop adequately in order to maintain a constant temperature all over the halo, and would soon reach unreasonable values below the cosmic background (compare Figure 6.2). We hence adapted the NFW potential to overcome the described problems, and to achieve a more realistic setup than the one used in Chapter 5.

6.2.2 Disc setup

Several approaches to establish a stable disc-halo system have been tested previously. Another detailed description for a possible setup can be found in Cooper et al. [2008]. In

Table 6.2: External bulge and disc potential parameters for simulation set 3 (ST, KE, TE, B and NC runs).

Component	Parameter	Value
Bulge	r_{C_1}	1.35 kpc
	M_{C_1}	$1.11 \times 10^9 M_\odot$
	r_{C_2}	0.21 kpc
	M_{C_2}	$5.92 \times 10^9 M_\odot$
Disc	b	0.15 kpc
	a_1	2.905 kpc
	M_{D_1}	$2.442 \times 10^{10} M_\odot$
	a_2	8.715 kpc
	M_{D_2}	$-1.073 \times 10^{10} M_\odot$
	a_3	17.43 kpc
	M_{D_3}	$1.221 \times 10^9 M_\odot$
	$r_{s,D}$	2.05 kpc

general, the following issues have to be kept in mind: Firstly, we want the gaseous disc to be rotationally supported (i.e. in hydrodynamic equilibrium), whereas the halo shall be pressure-supported (i.e. in hydrostatic equilibrium), which inevitably causes friction and shear effects in the transition zone. This problem will be mitigated automatically while we allow the system to settle into an overall equilibrium within a few Myr. As stated above in eq. (2.59), the total potential is built up of three components, whereas the disc component $\Phi_{\text{disc}}(r, \theta)$ is a combined form of a Miyamoto-Nagai potential [Miyamoto and Nagai, 1975]:

$$\begin{aligned} \Phi_{\text{disc}} = & -\frac{G M_{D_1}}{\sqrt{R^2 + (a_1 + \sqrt{z^2 + b^2})^2}} \\ & -\frac{G M_{D_2}}{\sqrt{R^2 + (a_2 + \sqrt{z^2 + b^2})^2}} \\ & -\frac{G M_{D_3}}{\sqrt{R^2 + (a_3 + \sqrt{z^2 + b^2})^2}}. \end{aligned} \quad (6.12)$$

The bulge component $\Phi_{\text{cent}}(r)$ is basically a central potential,

$$\Phi_{\text{cent}} = -\frac{G M_{C_1}}{\sqrt{r^2 + r_{C_1}^2}} - \frac{G M_{C_2}}{\sqrt{r^2 + r_{C_2}^2}}. \quad (6.13)$$

We have scaled down the mass-related parameters from Flynn et al. [1996] (M_{D_1} , M_{D_2} , M_{D_3} , M_{C_1} and M_{C_2}) by a factor of 0.37 to match the residual disc mass (gas and stars) of $2.1 \times 10^{10} M_{\odot}$. The length-related sizes (a_1 , a_2 , a_3 , b , r_{C_1} and r_{C_2}) in the description by Flynn et al. [1996] have been scaled down by a factor of 0.5 for our purpose, leaving our disc at a scale radius of 2.05 kpc. An overview of all the values related to the bulge and disc potentials is given in Table 6.2. For comparison, a typical LBG is assumed to have comparatively small size, and a mass probably an order of magnitude smaller (a few $10^{10} M_{\odot}$) than the more massive SINS galaxies [Genzel et al., 2008]. They form stars dominantly in a steady mode at a range of star formation rates, tens of solar masses per year not being uncommon [Pettini et al., 2001, Shapley et al., 2003].

We assume here that 50 per cent of the disc mass are already locked inside its stars, which gives us some freedom of choice for the gas density distribution, since that the disc potential is made up by the combined mass of gas and stars. We use an exponential (in radius) gas density profile with a cutoff at $r = 5$ kpc, that is vertically nonstratified. The disc density is known from equation 3.14, whereas $\rho_{\text{disc},0} = 1.0 \cdot 10^{-22} \text{ g cm}^{-3}$. The disc has a vertical height of 500 pc, and thus the total gas mass is $1.1 \times 10^{10} M_{\odot}$, i.e.

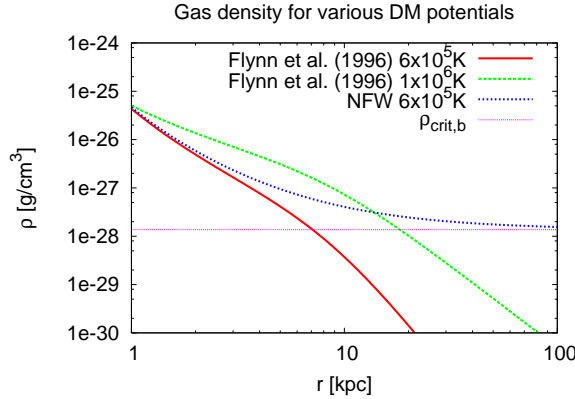


Figure 6.2: Hydrostatic gas mass density in g cm^{-3} for three NFW haloes and two DM haloes with a $\ln(r)$ -profile as is described in Flynn et al. [1996], at different equilibrium temperatures, respectively. For the NFW profiles, density and therefore pressure converge against the cosmic background value quickly for every temperature, whereas this is not the case for the $\ln(r)$ -profiles. The polar angle for all curves is $\theta = \pi$.

about 50 per cent of the mass implied by the disc potential. The disc gas pressure follows from the ideal gas equation (2.61), just as for the halo gas pressure. In Figure 6.3, the resulting density for our disc-halo system is shown as a contour plot; the initial and boundary conditions are further explained above. This setup condition applies to the complete set of simulations presented in this chapter (see Table 6.1).

6.3 Pressure-driven winds

We begin with an investigation of how the method of SN energy injection affects the emerging wind. For this purpose, we have run a set of simulations with $\zeta_0 = 100$. One simulation uses the Sedov-Taylor blast wave model, and hence both kinetic and thermal energy are injected with every SN event (denoted 'ST100'). In addition, two models were calculated, injecting a purely thermal energy fraction of 40 per cent (denoted 'TE0.4'), and 60 per cent ('TE0.6') of the total SN energy yield, respectively, and another one, injecting a purely kinetic energy fraction of 40 per cent ('KE0.4'). The characteristics of the pressure-driven and the kinetic energy driven cases are discussed in the first two subsections, respectively.

The third subsection includes an analysis of the contribution of buoyancy to the wind

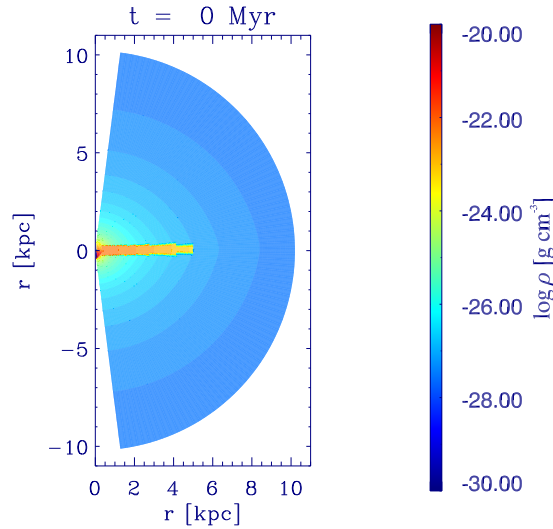


Figure 6.3: Initial mass density in g cm^{-3} at zero time. All simulations described in Chapter 6 are based on this setup. The disc is set up exponentially with $\rho_{\text{disc}}(r) \propto \exp(-r)$, whereas the halo gas features an exponential-like distribution of $\rho_{\text{b}}(r, \theta) \propto \exp(-\Phi(r, \theta))$. Note the slight deviation from spherical symmetry of the halo density due to the gravitational potential of the disc component.

energy in ST100, which will be compared to our theoretical consideration in section 2.2. All the runs presented in subsections 4.1, 4.2 and 4.3 include a cooling halo. Since halo pressure is reduced by cooling, winds will arise comparatively easily in this case, allowing for more prominent effects more suitable for later comparison. Subsection 4.4 investigates the question how the sizes of SN bubbles can affect the strength of galactic winds; for this we have run another set of three simulations featuring Sedov-Taylor blast wave models and different event sizes each. In contrast to the previous runs, the runs in subsection 4.4 are each performed twice, with both, a cooling and a non-cooling halo, respectively, to investigate the limiting cases of the possible effects of varying metallicities in such objects. We show that the different halo pressures have a significant effect on the wind. All of our results herein will then be compared in the final subsection.

In Figure 6.4 we show the mass density distribution of simulation ST100 at times of 10, 20, 40, 60, 120 and 180 Myr. We can clearly discern individual superbubbles expanding already at 10 Myr beyond a height of 1 kpc above and below the disc. These bubbles keep expanding, driven by their overpressure against the radially quickly declining halo pressure. At 40 Myr the superbubbles unite creating a low density funnel close to the

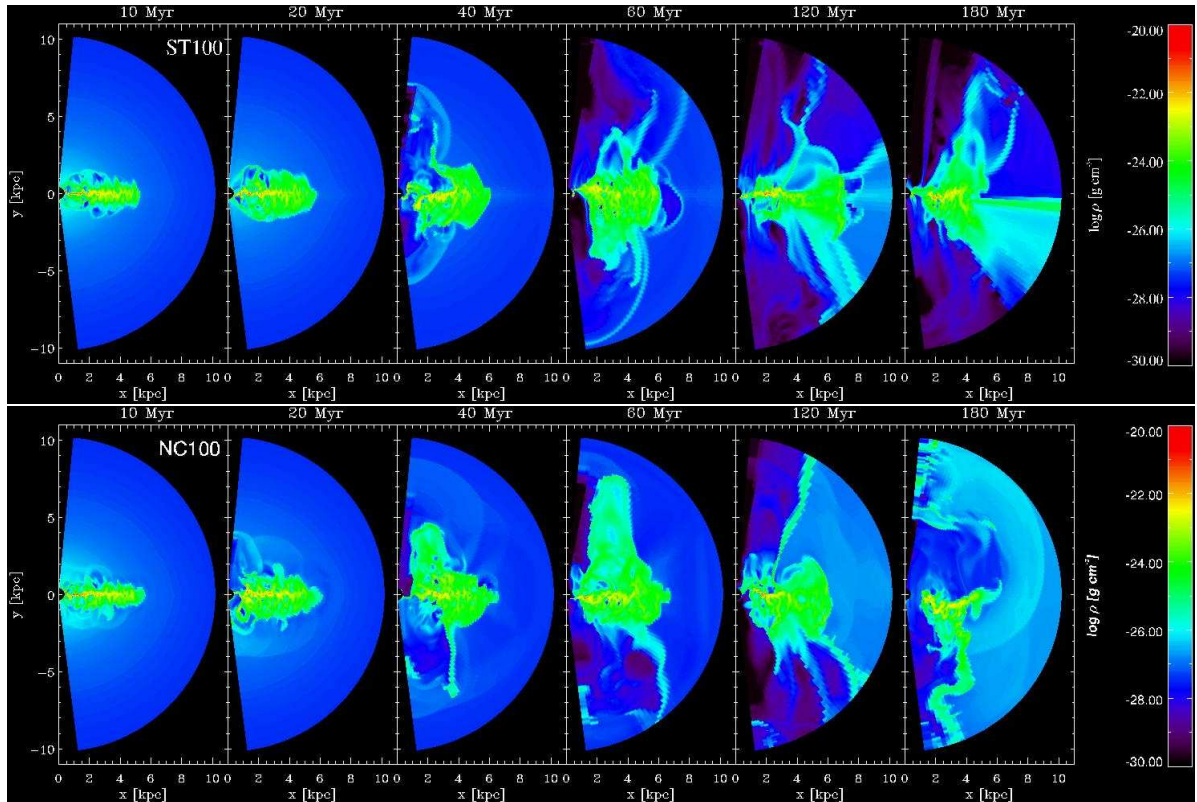


Figure 6.4: *Top:* Simulation ST100 with each SN releasing 4.0×10^{50} erg as kinetic, and 6.0×10^{50} erg as thermal energy. Note that the time span between two snapshots is not always the same; the elapsed time is denoted above each snapshot. Shown is the logarithm of the density in meridional midplanes. *Bottom:* Simulation NC100 with a non-cooling halo; see subsection 4.4. for details

axis of symmetry. Since the gas inside this structure provides less resistance to subsequently escaping superbubbles than the rest of the halo region, material from succeeding bubbles will continue to flow at ease through the funnel. The latter is surrounded by a conical structure of notably denser material which was originally entrained from the dense disc by outgoing shock fronts and hence continues to move outwards. Over time, enormous amounts of SN energy are fed into the disc, which in turn becomes extremely turbulent: large portions of gas are torn out of the disc midplane, partially due to entrainment by the wind, but eventually fall back into the former. The shape of the disc gets highly irregular and clumpy but the disc remains overall intact.

Since we are dealing with a rather massive system, it might seem likely, regarding the studies by Dubois and Teyssier [2008], that outflows appear preferably in the form of galactic fountains. These would exhibit velocities below the local sound speed c_s , notably slower than the supersonic galactic winds. Regarding their morphology, convections would be discernable by a widely spherical shell of compressed halo gas all around the overall turbulent disc, whereas the wind emerges mainly from the central part of the disc, showing a conical outflow structure. Despite the fact that there are traces of outflowing material in the outer disc parts in Figure 6.4, the conus structure is still the more dominant. It can be further made sure by measuring the outflow velocity in units of c_s , that large portions of the outflowing material is well beyond sound speed. Figure 6.5 shows the outflow velocities with respect to the local sound speed at 100 Myr; the velocities are capped at 0 and $10 c_s$. We have hence made sure that the presented model indeed produces a true galactic wind.

We make here the usual distinction [compare e.g. Dubois and Teyssier, 2008] between the two common types of outflow solutions: A wind is defined to be supersonic with respect to its internal sound speed. A fountain, on the other hand, is subsonic. Galactic fountains are therefore much more susceptible to the Kelvin-Helmholtz instability and usually turbulent. Both types of solutions may in principal be bound to the galaxy or reach escape velocity. The smaller bulk velocity of the fountain solution usually prevents it from escaping the galaxy and the flow becomes convective, lead by a roughly spherical weak shock or sound wave around the whole system. In contrast, the bulk velocities in the wind gas may easily reach escape velocity. Due to the geometrical constraint from the galactic gas disc, the outflow becomes conical. Figures 6.4 and 6.5 demonstrate that the outflow which has emerged in run ST100 has developed all the usual characteristics for a wind solution. The escape velocity at 10 kpc distance from the disc amounts to $v_{\text{esc}} = 426 \text{ km s}^{-1}$, which is well below the typical wind velocities close to 10^3 km s^{-1} . The difference to Dubois and Teyssier [2008] is mainly the size of the disc. Dubois

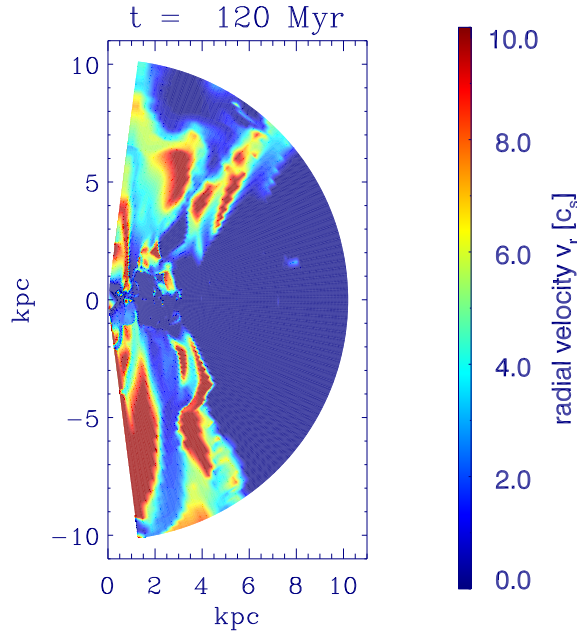


Figure 6.5: Radial velocity of outflowing gas regions in units of their respective local sound speed c_s . The velocities are capped at $0 c_s$ and $10 c_s$.

and Teyssier [2008] have chosen a much larger disc and therefore might not reach the required SN density to drive the outflow.

6.3.1 Mass outflow

For a quantitative analysis of our models, we will calculate the net mass flux across a spherical shell of inner radius r_i and outer radius r_o first, averaged over time. We start with

$$l_M(r, t) = k_\phi \frac{1}{\Delta r} \int_{0.04\pi}^{0.92\pi} \int_{-0.04\pi}^{0.04\pi} \int_{r_i}^{r_o} \rho(r, \theta, \phi, t) v_r(r, \theta, \phi, t) d\theta d\phi r^2 \sin\theta dr, \quad (6.14)$$

which is the net mass flux at any point t in time for a spherical layer of grid cells at a given radius r . The factor $k_\phi = 25$ is a correction term which accounts for the fact that our simulation box covers only 1/25 of the total ϕ range. Due to the box limits in θ range, a part of the wind at the poles is neglected. Due to the small surface area, this error is not significant. The average mass flux for all layers at radii $r_i < r < r_o$ is determined every 1 Myr, and then averaged over 10 Myr, yielding the total net mass

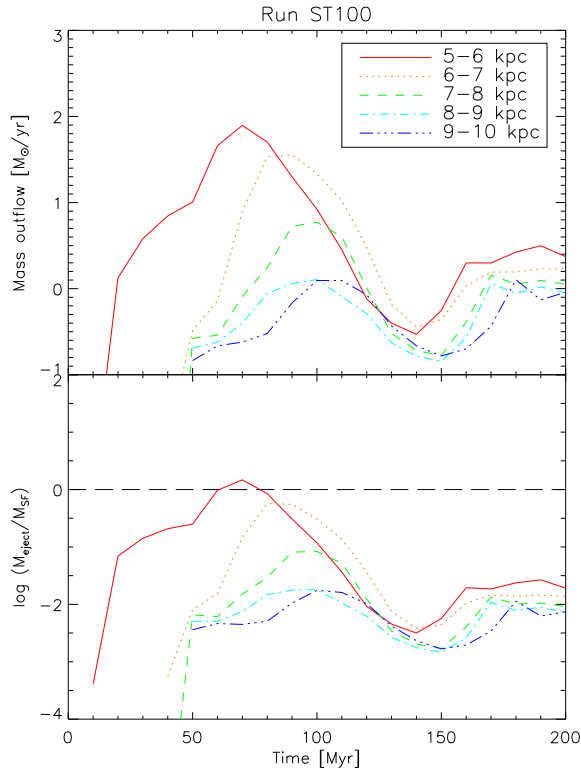


Figure 6.6: *Top:* Mass flux rates through different shells of respective thickness 1 kpc. *Bottom:* Efficiency of mass output, defined as the ratio of outflowing mass M_{eject} to star-producing mass M_{SF} . The dashed black line marks unity.

flux $L_M = \langle l_M(r, t) \rangle$. Figure 6.6 shows mass flux rates from 0-200 Myr for run ST100 across shells of respective thickness of $\Delta r = 1$ kpc for various shell positions. In the innermost shells, winds will show up earlier and stronger, however, a large fraction of the outflowing mass in these inner shells is likely to represent entrained disc material. This material might, in some cases, fall back soon after its ejection from the host disc, and actually not contribute to the mass carried away by the wind.

6.3.2 Energy outflow

To obtain the net energy flux, we assume the same shells as before, however, the energy flux for a given radius at any point in time comprises both a kinetic and a thermal energy component of the wind, and can hence be written as

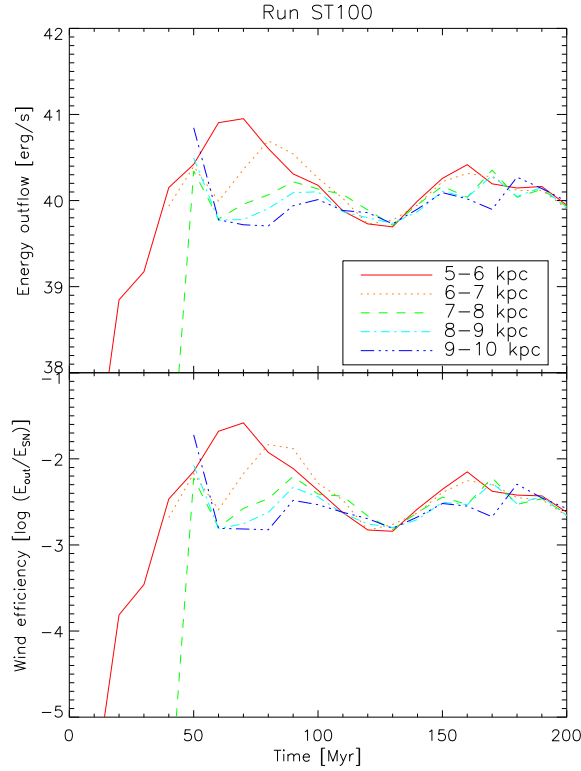


Figure 6.7: Analysis of simulation ST100. *Top:* Energy flux rates through different shells of respective thickness 1 kpc. *Bottom:* Efficiency of energy conversion, defined as the ratio of thermal plus kinetic energy carried by the wind E_{out} to bulk energy released by supernovae E_{SN} .

$$\begin{aligned}
 l_E(r, t) = & k_\phi \frac{1}{\Delta r} \int_{0.04\pi - 0.04\pi}^{0.92\pi} \int_{-0.04\pi}^{0.04\pi} \int_{r_i}^{r_o} \left(\frac{\rho(r, \theta, \phi, t) v(r, \theta, \phi, t)^2}{2} + \frac{p(r, \theta, \phi, t)}{\gamma - 1} \right) \\
 & \cdot v_r(r, \theta, \phi, t) d\theta d\phi r^2 \sin\theta dr.
 \end{aligned} \tag{6.15}$$

The mean value for the net energy flux is averaged in the same way as the net mass flux, namely $L_E = \langle l_E(r, t) \rangle$. Again, the energy flux rates displayed in Figure 6.7 represent different shells of 1 kpc thickness each, for different shell positions.

Comparing the respective shells of measurement in Figures 6.6 and 6.7, we can clearly see a convergence of the graphs with increasing shell radius. Measurements closer than 7 kpc exhibit more pronounced extrema, and, in case of strong turbulent feedback or

irregularities in the disc, may be prone to notable perturbations arising from the disc. If too close to the box boundary at 10.2 kpc, interactions with the boundary itself might distort the actual result in a few cases. Therefore, we choose the range in between $8 \text{ kpc} < r < 9 \text{ kpc}$ as the most reliable one.

All plots exhibit one more or less strong peak, which is the first shock front clearing the path for the wind yet to come. Any further peaks are a result of local and temporal concentrations of SN events; yet these anomalies will be mitigated as the energy outflow will stabilise over time. The basic level of energy carried by the wind is several $10^{47} \text{ erg s}^{-1}$. So, with an average input of some $10^{50} \text{ erg s}^{-1}$ in our models, we can define a wind efficiency as the ratio of wind energy to injected energy. The latter is stable on a level around $10^{-2.5}$, as is shown in the lower panel in Figure 6.7.

6.4 Kinetic energy-driven winds

In order to compare directly the respective importance of the thermal and kinetic forms of energy injection, we have performed three simulations, where we inject only thermal energy or only kinetic energy (Figure 6.8). Note that these simulations permit cooling in the halo, which subsequently reduces the environment pressure the wind has to overcome. The cooling halo is particularly necessary for the sake of the comparison in this section; without it a wind may not be strong enough to leave the disc at all in some of the presented cases. In run TE0.6, we inject the thermal energy component, only, using the standard fraction of $0.6 \times 10^{51} \text{ erg}$ per injected SN. This run has a slightly slower wind start, but later on is statistically indistinguishable from run ST100 regarding mass and energy outflow rates (Figures 6.9 and 6.10). Using only the 40 per cent kinetic energy (KE0.4), the wind is much weaker: It has now a much harder time to get out of the disc. The part in the hemisphere with negative z values is even dragged back by the ram pressure of the infalling halo (120 Myr). The wind stalls completely between 110 and 120 Myr (compare Figures 6.9 and 6.10). These results seem to indicate that the thermal energy part is the more important one for wind driving. We have also performed a run (TE0.4) with the thermal energy injection being reduced to the level of KE0.4. Here, the wind is also noticeably weaker, and the downwards going bubble also comes back. The statistics indicate a stronger outflow for TE0.4. However, the system is evidently just around the threshold, where it can drive a wind at all. Therefore, small changes might affect the result strongly. Remembering that our numerical scheme conserves the thermal energy better than the kinetic one (compare Section 3.5), we conclude that the differences between KE0.4 and TE0.4 are not significant.

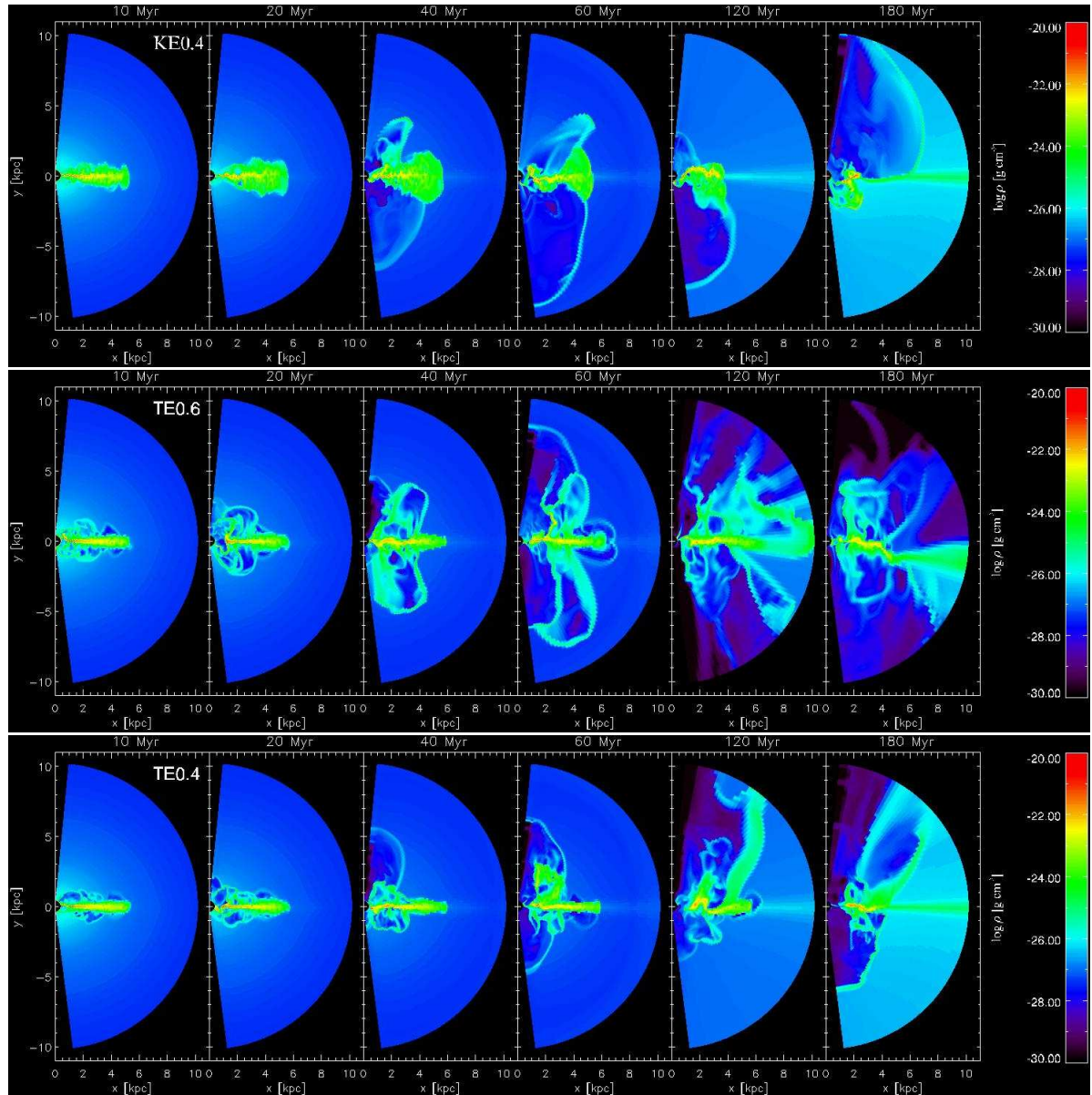


Figure 6.8: *Top:* Simulation KE0.4 with each SN releasing 4.0×10^{50} erg as kinetic energy only. *Middle:* Simulation TE0.6 with each SN releasing 6.0×10^{50} erg as thermal energy only. *Bottom:* Simulation TE0.4 with each SN releasing 4.0×10^{50} erg as thermal energy only. Snapshot times are identical to Figure 6.4

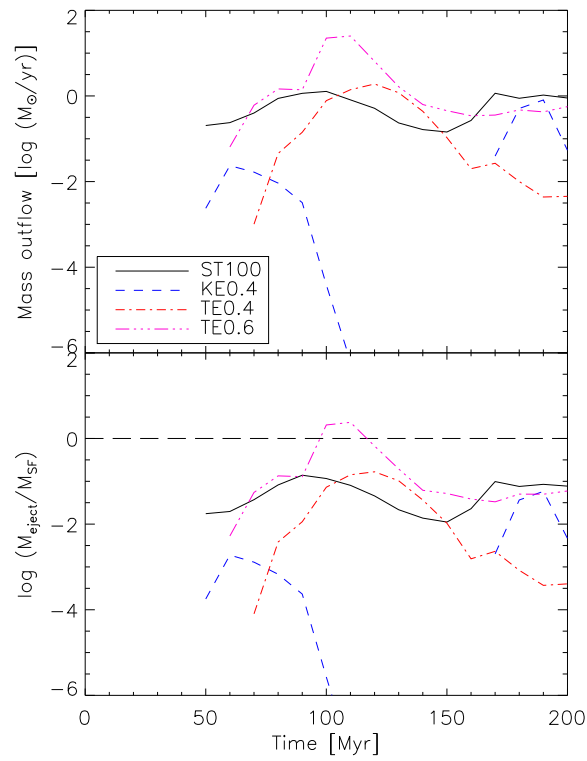


Figure 6.9: Absolute (*top*) and relative (*bottom*) mass flux rates, for different types and quantities of feedback energy. The solid black line represents model ST100 with a normal Sedov-Taylor energy distribution for comparison. The dashed blue, dash-dotted red and triple-dot-dashed purple line are the models KE0.4, TE0.4 and TE0.6, respectively.

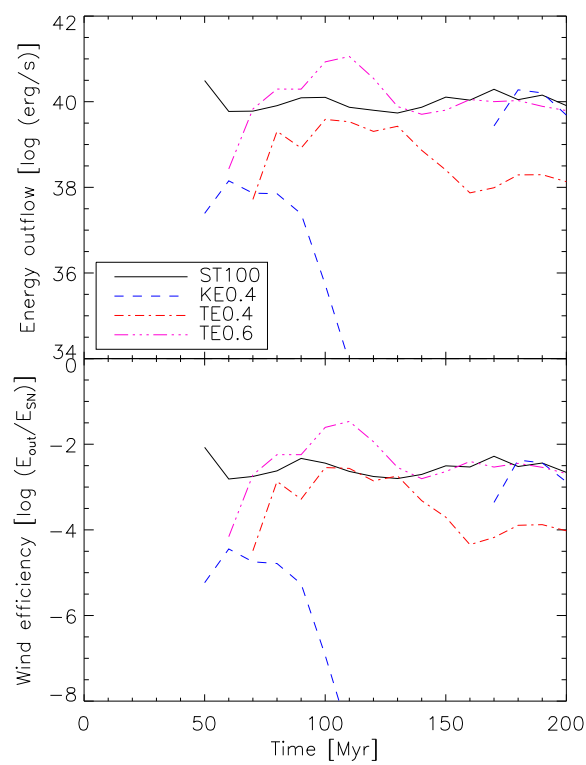


Figure 6.10: Absolute (*top*) and relative (*bottom*) energy flux rates, for different types and quantities of feedback energy. The linestyles and colours are the same as in Figure 6.9.

6.5 Buoyancy

We have shown in Subsection 6.1.1 above that SN bubbles in reality would typically exhibit entropy index values of order 10 keV cm^2 . For an event releasing $6 \cdot 10^{52} \text{ erg}$ in thermal energy, i.e. 100 SNe, the entropy index from equation (6.2) calculates to $1.7 \cdot 10^8 \text{ keV cm}^2$. Mixing reduces this value quickly to about $10^4 - 10^5 \text{ keV cm}^2$ (compare Figure 6.11), but this is still a significant number. This enormous value dramatically increases the likelihood of buoyant superbubbles contributing notably to the wind in our models. We shall hence have a closer look at the energy which is released only by the ascendance of a SN bubble.

The gravitational acceleration is generally given by

$$g = \frac{GM}{R^2}, \quad (6.16)$$

with $M = 7.7 \cdot 10^9 M_\odot$ being the total baryonic and dark matter mass and 3.3 kpc being the disc radius, which yields $g = 10^{-8} \text{ cm s}^{-2}$. If the gas density in the bubble is much smaller than the surrounding it will be accelerated upwards with g . Allowing a bubble to ascend through the halo for 79 Myr would hence lead to an ascension height of 10 kpc, at which the bubble would have obtained a velocity of 249 km s^{-1} . Since the winds in run ST will quickly reach peak velocities well above 1000 km s^{-1} , this would be a contribution of less than about 6 per cent to the total outflow energy by buoyancy, regardless of ongoing mixing processes.

The entropy index for run ST100 is shown in the upper box in Figure 6.11, after 100 Myr runtime. Since we do not allow radiative cooling below 10^4 K , there is only one way for the gas to reach lower temperatures than this, which is adiabatic expansion. The latter occurs when material is entrained by the wind from the disc and begins forming filamentary structures, assembled in a cone-shape around the main wind channel. The disc and original halo gas is both smeared out to some extent in the course of the simulation, whereas the white shape represents the system at 1 Myr, just before the onset of SN feedback. The resulting SN bubbles form at the highest temperatures, whereas during bubble expansion the entropy index S stays constant. Any bubble would thus follow a horizontal path toward the left-hand side of the plot until the point when mixing processes start playing a role, eventually dissolving the bubble. If we compare the entropy index of the original halo at 1 Myr to the bubble region, we find that a large number of bubbles could theoretically ascend above the highest halo regions by buoyancy, and thus contribute to the arising wind. However, the energy released that

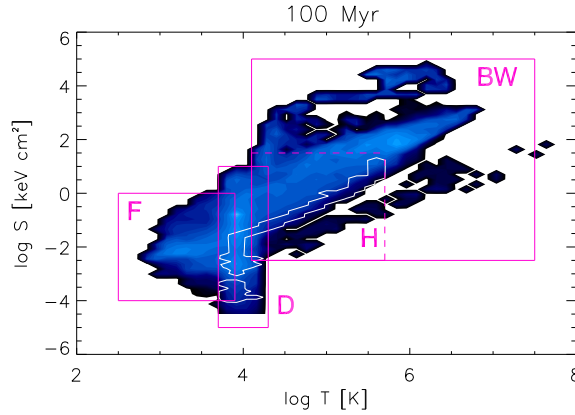


Figure 6.11: Entropy against temperature after 100 Myr, for different regions of the disc-halo system. Shown is the logarithmic volume at given values for the logarithms of temperature and entropy index. Light blue means high, and dark blue means low. Filaments (F) and disc (D) can be clearly discerned. The transition between halo (H) and bubbles/wind (BW) is fluent, indicated by a dashed line. The white shape is the initial disc-halo distribution just prior to the first SN.

way contributes only a small part to the total wind energy, which has been shown above. We have run a comparison simulation (B100) with a ten times higher density inside the bubbles upon injection, with very similar results, showing that our results are insensitive to the exact choice of this parameter.

6.6 Bubble size

The last set of simulations presented in this study features a variation of the event size ζ_0 introduced above in Section 3.4.2. The event size specifies the number of SNe comprised in one single bubble. On average, for $100 M_\odot$ of newly formed stars, we inject one SN and a gas mass return through stellar winds and SN ejecta of $25 M_\odot$. This in turn requires a minimum available mass of $7.5 \times 10^4 M_\odot$ per cell for $\zeta_0 = 100$. However, there is a chance for a mass deficit to occur, typically in the outmost parts of the disc where the defined minimum density of 10^{-24} g cm^3 is just reached, or in cells close to the inner radial boundary which exhibit small absolute angular diameters. On the other hand, the average cell mass will be $4.4 \times 10^4 M_\odot$, which is well above the requirement for a 200-SN event. The mass deficit is not a severe issue, since in reality, the mass would come from neighbouring cells, and because the global error on the mass budget is small, no significant effect on the dynamics is expected. Locally, one might expect

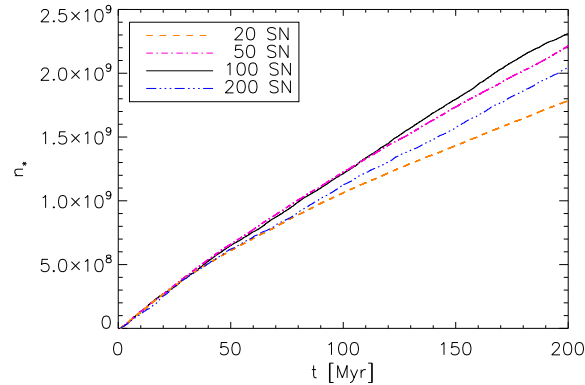


Figure 6.12: Total number of stars formed n_* for different respective amounts of SNe per bubble ζ_0 , indicated in the inset legend.

that we might artificially somewhat damp the kinematics in the large bubble simulations because of the slightly higher inertia in these runs. Yet, as we show below, we find that large bubble simulations exhibit the strongest winds.

Note that in some of the following simulations (NC20, NC50, NC100 and NC200) the threshold above which we inhibit radiative cooling is reduced below the halo equilibrium temperature of 600,000 K. We include these non-cooling simulations in addition to the ones with cooling at solar metallicity, in order to investigate possible effects of metallicity: For metal poor gas halos, the cooling time is prolonged. Such galaxies will therefore likely have a hydrostatic halo as we describe it. For increasing metallicity, the thermal pressure will drop due to cooling but at the same time ram pressure due to the inflowing gas will increase [compare Dubois and Teyssier, 2008]. With the approximations of solar metallicity cooling (ST) and non-cooling (NC) haloes, we try to capture the extreme cases, keeping in mind that a full parameter study in a Cosmological setup is clearly beyond the scope of this work. The values chosen for ζ_0 in these simulations are 20, 50, 100 and 200 SNe, respectively (see Table 6.1). In the following, the total SFR, the onset of the wind and its temporal development will be of particular interest. We will further investigate the mass and energy efficiencies in the same manner as above. It may seem reasonable to assume that, since smaller bubbles are situated much closer to each other than large ones, dense material in between will be further compressed until star formation sets in, thus providing a positive feedback to the SFR. Yet, large bubbles may prove more powerful when it comes to triggering the wind, and thus we could find that a larger ζ_0 , though providing little less energy input, results in a slightly more efficient wind.

6.6.1 Star formation

A look at Figure 6.12 immediately reveals that the cumulative SFR for different bubble sizes undergoes little change within 8 per cent, until just before 50 Myr. This difference grows, being already around 24 per cent at 200 Myr. An explanation for this could be that large bubbles result in a violent blow-away of large gas portions, whereas small bubbles, due to their numerous occurrence, smear out the disc material over a comparatively large volume, reducing the chances for the gas to pile up in high amounts on any single spot. Both effects can result in a visible reduction of star formation, and hence the optimum range for star formation comes to lie in between 50 and 100 SNe per event. In Figure 6.13 we plotted the mass-weighted height h_M of the gas above the disc mid-plane, which calculates as

$$h_M = \frac{\int r |\cos \theta| dm}{\int dm}. \quad (6.17)$$

The resulting value for h_M indicates the average height of all gas portions in kpc above the disc plane at any given time. We find that for NC200 h_M is significantly larger as for NC100, but only between 40 and 100 Myr, while NC20 and NC50 show comparatively little difference. NC100 and NC20 however increase strongly in the last 30 Myr. Increasing values mean that during this time much of the gas is torn out of the disc forming filaments, which constitute large quantities of gas unavailable for star formation. But if this were to be the reason for the lower SFR in NC200, we would expect the NC200 graph to dominate clearly from about 50 Myr onwards. This possibility can hence be excluded.

In contrast, small bubbles of 20 SNe should have a smoothing effect on the overall density profile of the disc. The number of columns with respect to their density is visualised in Figure 6.14, whereas the total column number n_c includes all columns within $r < 5$ kpc and is integrated over the total simulated time span of 200 Myr. The curve for NC20 should exhibit more moderate values than its NC200 counterpart, whereas extreme values below $10 M_\odot \text{pc}^{-2}$ and above about $60 M_\odot \text{pc}^{-2}$ should be less present in the former. Columns of high density contribute most of all to the global SFR, and should be most present in the NC50 and NC100 curves. We find however, that neither of the four curves matches any of the expectations. Therefore, we can also exclude smoothening effects inside the disc from large numbers of small bubbles to be of notable effect to the SFR. This means that the SFRs in our simulations are set by a more complex interplay of processes.

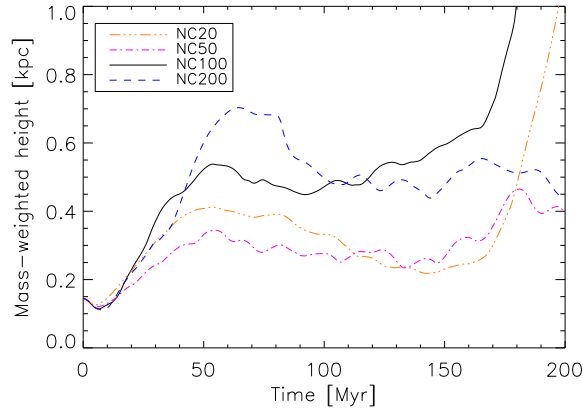


Figure 6.13: Mass-weighted height h_M of gas above the disc midplane.

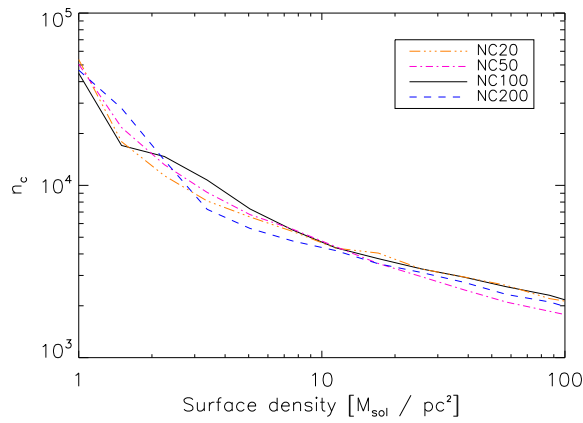


Figure 6.14: Surface density histograms for simulations NC20 - NC200, as indicated in the legend. We only take into account the region at radii $r < 5$ kpc and sum up the columns of all the 200 snapshots of each simulation over the entire simulation time of 200 Myr.

6.6.2 Mass and energy flux

Figures 6.15 and 6.16 show the absolute and relative mass flux, and the absolute and relative energy flux, respectively, for the different bubble sizes. It has to be borne in mind, that after 100 Myr the differences in the SFR become somewhat stronger (compare Section 7.1 below). There is no doubt that the mass flow curve for NC200 starts earliest, and much higher than the others. Early starting curves are a clear indicator that the wind developed fast; in the case of NC200 it takes 20 Myr for the wind to reach the radius of measurement at 8 kpc, giving it an average speed of nearly 400 km s^{-1} . Curves starting late suggest that the wind is setting in at a later point in time, but could also indicate a slower wind. The former case however applies to our simulations. The wind in NC100 starts early and still carries comparatively large mass. Of the two remaining ones, NC50 exhibits a stronger wind at a late start, whereas NC20 starts with little mass at an earlier time. When looking at Figure 6.16, it becomes more obvious, that large SN bubbles show a tendency to start blowing a wind in a powerful way. The NC200 and ST100 energy curves stay roughly constant in time, whereas NC20 exhibits a more chaotic behaviour after the onset of the wind. While the order is not strictly maintained throughout the simulation time, there is a clear general trend for larger bubbles to produce higher mass outflow rates. This is also generally confirmed from the cumulative numbers (Table 6.3): The two large superbubble simulations have a mass outflow rate which exceeds the one of the two small superbubble simulations by about an order of magnitude. Run NC200 has formed 11 per cent less stars than run NC100, and still ejects 34 per cent more mass. Only for run NC 50, we find a 21 per cent smaller outflow rate in comparison to NC20, while the star formation rate is 24 per cent higher. The trend is even more evident in the cumulative energy outflow rate (also in Table 6.3): For all the NC simulations, they increase monotonically with superbubble size, even if normalised to the star formation rate.

6.6.3 Halo pressure

There is however one more circumstance to be taken into account, which is the thermally pressurized halo. In the NC runs, this pressure can strongly inhibit the onset of a continuous galactic wind, as can be seen in Figure 6.4. In contrast to NC100, the ST100 run shows a clearly steady outflow, as the wind therein does not have to overcome such a strong environmental pressure from the halo. In order to study this effect more closely, we varied the bubble size for the cooling halo model to 20, 50 and 200 SNe, respectively.

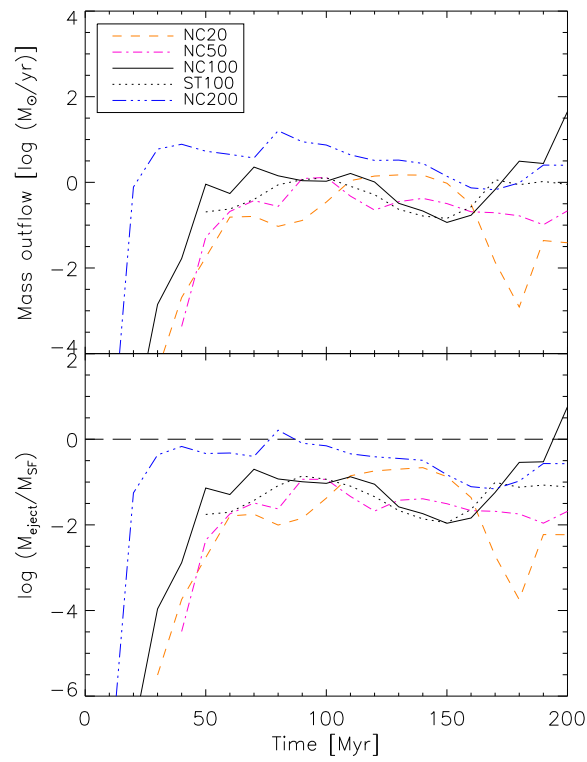


Figure 6.15: Mass flux rates in absolute (*upper*) and relative (*lower*) numbers for all four NC runs and ST100 (black dotted line). The relative values are normalized to the total mass of stars formed within the respective time.

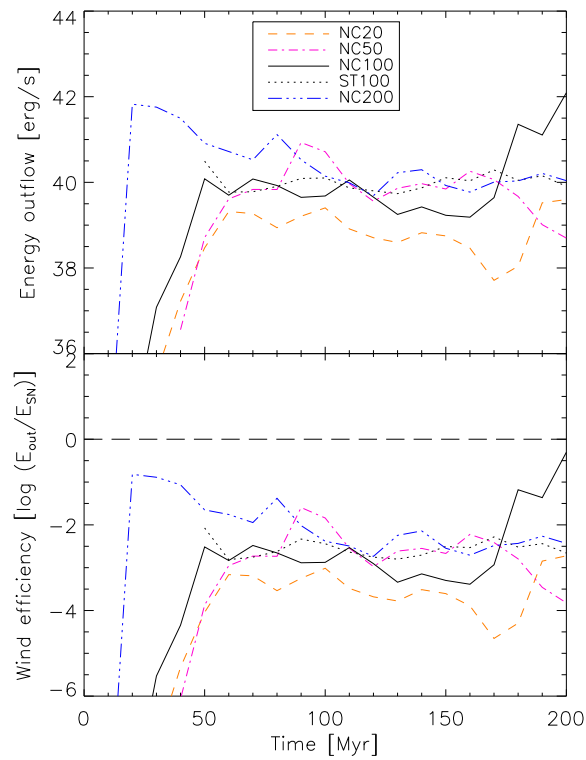


Figure 6.16: Energy flux rates in absolute (*upper*) and relative (*lower*) numbers for all four NC runs and ST100 (black dotted line). The relative values are normalized to the total energy release from SNe within the respective time.

Table 6.3: Cumulative mass and energy flux values after 200 Myr simulation time. The four bottom lines show the values for cooling halo models (ST) relative to non-cooling halo models (NC).

Run	Cumulative mass flux	Cumulative energy flux
ST20	$2.7 \times 10^9 M_{\odot}$	9.3×10^{56} erg
ST50	$3.5 \times 10^8 M_{\odot}$	1.1×10^{57} erg
ST100	$1.0 \times 10^8 M_{\odot}$	5.7×10^{55} erg
ST200	$1.4 \times 10^9 M_{\odot}$	3.5×10^{56} erg
NC20	$7.7 \times 10^7 M_{\odot}$	6.3×10^{54} erg
NC50	$6.1 \times 10^7 M_{\odot}$	7.2×10^{55} erg
NC100	$6.2 \times 10^8 M_{\odot}$	5.2×10^{56} erg
NC200	$8.3 \times 10^8 M_{\odot}$	6.3×10^{56} erg
ST20/NC20	35.1	147.6
ST50/NC50	5.7	15.3
ST100/NC100	0.16	0.11
ST200/NC200	1.7	0.56

In Table 6.3 the complete set of runs ST20, ST50, ST100 and ST200 is compared to their respective NC counterparts. The displayed values are the cumulative mass and energy flux rates until 200 Myr, in absolute numbers, $\int_0^{200 \text{ Myr}} L_M(t) dt$ and $\int_0^{200 \text{ Myr}} L_E(t) dt$, respectively. For each bubble size, the flux value of the respective ST run is normalized by the value for the respective NC run. It is obvious that for the smaller bubble sizes, $\zeta_0 = 20$ and $\zeta_0 = 50$, the outflow is stronger in the absence of thermal halo pressure. Moreover, ST20 and ST50 feature one major outburst each, where massive a local concentration of feedback energy leads to the ejection of a large share of hot gas from the disc. However, if $\zeta_0 = 200$, a steadily blowing wind arises also for the thermally pressurized halo; we find both mass and energy outflow rates for ST200 and NC200 to range in the same orders of magnitude, respectively. $\zeta_0 = 100$ represents a special case, where an exceptionally large filament is torn out of the disc after 170 Myr, which accounts for the bulk of mass and energy (also compare Figure 6.17). If this phenomenon is neglected, the flux values for ST100 and NC 100 would be of comparable magnitude.

Figure 6.17 shows one snapshot from all eight runs at the same time of 200 Myr. We find for $\zeta_0 = 20$ that in both cases the small bubble size only triggers a weak wind. In NC20, filaments bordering the upper and lower wind conus are absent, indicating that the halo pressure has already begun to force the wind conus back into the disc. In ST20 we find the wind to be asymmetric, being at least stable on one side of the disc. The same applies to ST50, where the wind is also dominant on one disc side only. NC50 in contrast developed a biconically stable wind, however, the conus is already in the process of being crushed. The wind in NC100 has ceased entirely; instead we can see the disc being just a few Myr before complete disruption - which also explains the enormous mass and energy outflow rates towards the end of NC100. ST100 on the other hand exhibits a clear biconical wind structure, with a wind steadily blowing in both directions. Stable winds also occur in NC200 and ST200. This supports our assumption that large superbubbles generally seem to boost the overall strength and steadiness of the wind. Furthermore it appears that for smaller bubbles the environment pressure becomes important. If the halo is thermally pressurized, winds arise but cannot overcome the halo pressure in the long term. In case of a cool, less pressurized halo, winds are on the brink of developing towards a stable, steady state; asymmetric developments with at least one of two conus being stable are not unlikely.

In summary, mass and energy outflow rates in the NC runs consistently show the same trend: if the event size ζ_0 is varied, the outflow rates for large ζ_0 's will tend to start comparatively high, and change barely over time. Small ζ_0 's will cause the wind to set

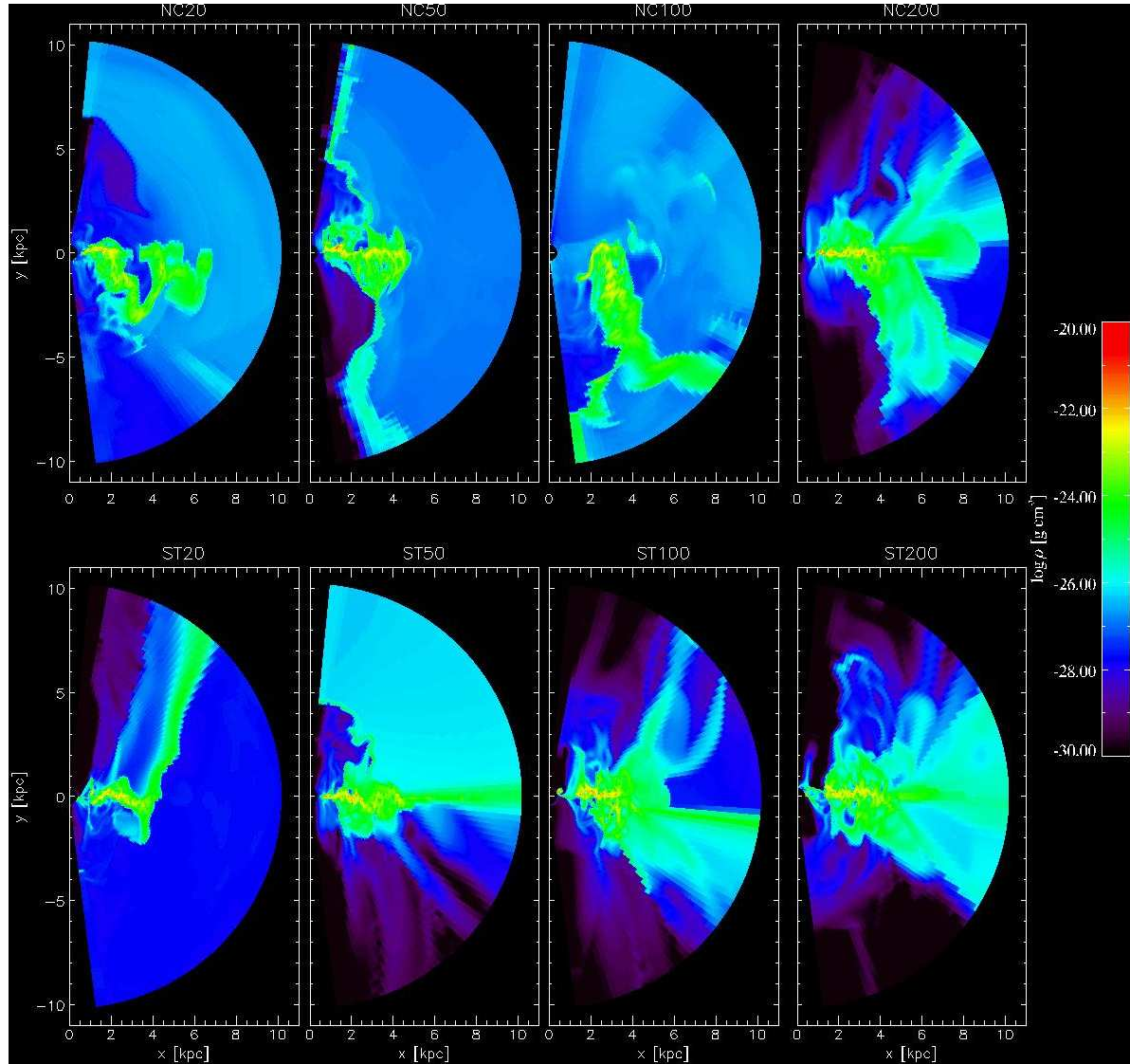


Figure 6.17: *Top row:* Simulation set NC at $t = 200$ Myr for $\zeta_0 = 20, 50, 100$ and 200 , from left to right respectively. *Bottom row:* Simulation set ST at $t = 200$ Myr for the corresponding values of ζ_0 .

in less forcefully, and, as is the case with NC20, undergo occasional drops in strength. The efficiency of mass ejection in our NC models will mostly be between $\sim 10^{-2}$ and unity. The efficiency of feedback energy conversion exhibits a convergence for most runs against $\sim 10^{-3}$, while values of $\sim 10^{-2}$ are still common, and $\sim 10^{-1}$ is already rare. For the ST runs, no clear trend can be discerned. A high halo pressure efficiently pushes smaller bubbles back into the disc, but low halo pressure enables bubbles of all event sizes to enter the halo overpressured and keep expanding. Therefore, the outflow properties do not depend systematically on the bubble size in the latter case. Instead, they tend to be dominated by single events, like the high concentration of SN bubbles leading to a violent ejection of large gas masses in ST20 and ST50.

6.7 Implications

We study four potentially important factors for wind driving, namely the thermal energy contribution, the kinetic energy contribution, buoyancy of SN bubbles and the local concentration of SNe which determines pressure and size of the superbubbles. It could be shown that the main launching mechanism is the thermal energy contribution and the amount of pressure it provides to a bubble. In consequence, we consider a multiphase ISM to be essential for the numerical simulation of galactic winds. The feedback of thermal energy alone is capable of converting up to about a factor of 10^{-2} times the available energy into the outflow. In comparison, kinetic energy can increase the strength of a wind but is very unlikely to be capable of launching a wind by itself. Buoyancy of superbubbles provides only around one per cent of the energy carried by the wind, which alone is insufficient to set up a wind as well. The wind strength grows with the superbubble size, and is significantly affected by the halo pressure.

Chapter 7

Discussion

7.1 Methodic accuracy

We have produced successful models of LBG's launching galactic outflows, in order to shed some light onto the exact mechanisms responsible for the onset of a galactic wind. These models feature a realistic galaxy setup with superbubble events, similar to the setup used by Dubois and Teyssier [2008]. Our equilibrium setup allows us to investigate the reaction of the system to systematic changes of parameters like the halo pressure or the superbubble size. Our methods described in Section 3 comprise the most important physics, however, some simplifications had to be made which require further discussion.

The star formation in our last set of models is determined by a local Kennicutt-Schmidt law, and converges with increasing resolution. It is also sensitive to local events, such as material ejections and the bubble size. The latter is clearly a significant effect: In our resolution study (Figure 6.1), we find that the number of stars formed after 200 Myr agrees within 26 per cent. However, there is a convergence for resolutions finer than 36 pc. If we disregard the 65 pc resolution, the deviation already shrinks to nine per cent. Varying the bubble size yields a change in star formation of about 24 per cent. Larger bubble size leads to stronger star formation, yet very large bubbles seem to lead to such a strong outflow that the star formation gets weaker again. We believe that this feature of the model is realistic.

We have also investigated the dependence of the outflow rates on resolution. Apart from

the 65 pc case (R65), which also shows a stronger deviation in the star formation rate, there is no strong or systematic deviation among all the runs with better resolution.

7.2 Disc and halo mass

The disc mass in our simulations has been varied over two orders of magnitude, whereas all of our discs are very gas-rich, with less than 50 per cent of their respective masses being locked in stars. We find a systematic behaviour in the evolution of galactic winds, which are more likely to emerge from low-mass discs. With increasing disc mass, winds become weaker and less continuous.

Regarding the halo potential, there are some trends which can be lined out: A steep potential slope close to the centre can encumber the development of a wind, as for instance in run F-ST which features a logarithmic potential curve. However, if the potential curve converges for large radii, outgoing bubbles face a counter-pressure nearly constant in radius and might even collapse back onto the disc, as is the case e.g. in NC100, where thermal halo pressure is strong due to the NFW potential shape and also to a lack of cooling. This suggests that a logarithmic potential allows for winds to blow relatively strong once they manage to escape the disc, whereas a NFW potential makes it relatively easy for the wind to escape the disc, but opposes more resistance at high radii.

Another quantity to be taken into account is the baryonic halo component. If the baryonic density is low, cooling time and hence thermal pressure will be high, which is a suppressing factor to the wind. The ST runs, where the halo is relatively dense and quickly cooling, thermal pressure is reduced, which increases the chances for a strong continuous wind. However, ST20 and ST50 with their low SN event sizes do not show continuous winds, which might also be contributed to the disc mass being ten times as massive as e.g. in ED-3 or ED-4. This hints to a more complex interplay of disc mass and halo mass, which ultimately determines the development of a wind.

7.3 Supernova injection mechanisms

Two different injection mechanisms for SNe have been implemented and investigated in the course of this work. The first mechanism is based on the local Jeans mass and mass density. We consider this approach to be physically motivated by the fact that stars form in clouds that are dense compared to their surroundings. These clouds are

often shaped by feedback processes like e.g. stellar winds and turbulence. It is generally realistic to implement SN injection based on local criteria since star formation is a local phenomenon. However, our resolution study has shown that the global star formation rate changes significantly with resolution, which points to more complex physical processes our implementation can only reproduce within a narrow resolution range.

The second mechanism triggers SN bubbles randomly, in accordance to the Kennicutt-Schmidt law for star formation (compare equation (3.8)), which is correlated to the column density Σ , but neglects the volume density of the constituent cells within the column. Local phenomena are hence less well represented in this implementation, however, it is in better accordance to observations of star-forming disc galaxies than the local, Jeans mass-based prescription. The global SFR in the model discs could be shown to converge with increasing resolution. Increasing SN probability with the local mass density could include local physics in the second mechanism. In this case more bubbles would occur deeper within the disc and would thus have a harder time reaching the halo. The net effect would be an overall mitigation of the wind by an unknown factor, which might explain the weakness of the wind in simulations using local SF recipes (F-ST and F-KE). In consequence, energy would be converted even less efficient.

In the second approach, we further had to implement a lower volume density threshold for cells to count as part of the disc and to amount to the surface density of their specific column. Note that the value used for our models, $2 \times 10^{-24} \text{ g cm}^{-3}$, is just a crude estimate for the lowest density regions found in the 10^4 K gas phase of the ISM, and thus allows for some variation. For instance, a lower threshold will open up a regime of rarefied cells surrounding the disc as is currently defined. This will have an effect on the distribution of the SN events, allowing for a bubble to blow out into the halo with less resistance. Though, the change in total will likely be of little effect regarding the wind strength - note that such rarefied cells will likely contain just around $100 M_{\odot}$. This would definitely call for the modification of our probability function, which, if applied, would make an event in these cells extremely unlikely.

7.4 Wind drivers

Our work concentrates on the mechanisms behind galactic outflows. We could show that buoyancy can drive bubbles out of the disc, but by itself is not powerful enough

to trigger fast-flowing galactic winds without any supplementary yield of energy, even not in our present simulations, which if anything overestimate buoyancy. We find that the thermal energy component by itself is sufficient to drive a wind. Whether or not we add the kinetic energy does not significantly change the result. We find a much weaker wind if we use the kinetic energy component, only. Even in simulations with the same overall energy injection, but once thermally and once kinetically injected, we find that the thermally driven wind is much stronger. This has been tested for two different setups, whereas the results are consistent for both. There is a good reason why we should expect such a behaviour: A pressure supported bubble will simply expand into the direction of the strongest pressure decline, i.e. radially outward, once the halo is reached. Gas which just has its kinetic energy may not accelerate as efficiently by this pressure gradient. On the contrary the pressure force works the other way, because the bubble is under-pressured much faster. Moreover, for the non-cooling halo, which maintains a high thermal pressure and thus oppresses wind formation compared to a cooling halo, we find the wind energy to vary by a factor of 100 for different event sizes (Figure 6.16 and Table 6.3). An event size of 200 SNe (NC200) produces a strong wind, and an event size of 100 SNe (NC100) a weak one, just strong enough to enter the thermally pressured halo. These two orders of magnitude make the difference between existence and absence of a wind. For the different feedback energy types however, the wind energy already differs by 10^6 (compare Figure 6.10), with the wind set up by purely kinetic energy (KE-0.4) temporarily coming to a complete breakdown. However, because thermal energy is conserved better by our numerics, we may underestimate the effects of the kinetic energy injection.

It should be pointed out here, that additional kinetic energy inside a disc might generally be provided e.g. by turbulence resulting from filamentary inflow or from magneto-rotational instabilities. These, in addition to the SN feedback might make up for a total kinetic energy supply high enough to trigger significant outflow. However, if we are to deal with solely feedback-driven winds, excluding sources of energy not directly related to SN feedback, our results indicate that thermal energy drives the outflow in a more constant manner than kinetic energy, even if both are injected in equal quantities. Complete suppression of the wind, as is the case with kinetic energy in between 110 – 170 Myr does not occur with thermal energy-driving.

We have found for run KE0.4, that kinetic energy is converted highly inefficiently. Hence, we could argue that, no matter what the actually provided amount of kinetic energy is, the chances of resulting in a continuous outflow are generally small. Even stronger kinetic energy feedback would then, more likely, result in partial or even complete dis-

ruption of the gas disc as such, as is eventually the case with run F-KE. This becomes clear when we take a look at the morphology of our model discs. Our simulations already show heavy distortions of the disc by the injected feedback energy, suggesting that they are close to the kinetic energy level necessary for disruption. If then a comparable amount of additional kinetic energy is spread equally inside the disc, we expect exactly this to happen. Regarding the leading shock fronts in this case, if a shock front made of compressed gas is allowed to expand only by its momentum initially received, it will quickly slow down and collapse again due to over-expansion. To ensure further growth, the shock front needs support by significant overpressure of the underlying rarefied region, which will be continuously provided by further superbubbles strong enough to penetrate the halo. The cool, dense phase of the ISM is torn out of the disc to form the wind's filaments, which feature prominently in optical emission line studies. Whenever a superbubble escapes from the disc, overlying and adjacent regions of disc material are entrained by the fastly expanding bubble interior. Subsequent bubbles produce further filaments, while those from previous bubbles still remain farther outside; eventually, the inner filaments start to merge with the decelerating, outer ones to create the characteristic biconical wind channel. Aside from that, this phase is required for star formation in the first place, making it the key ingredient to trigger the feedback cycle. It therefore seems reasonable to assume that the key to driving a wind lies within the existence of a multiphase ISM, featuring a cool ($< 10,000$ K), dense phase as well as a hot ($> 10^6$ K), rarefied phase at high pressure. Comparing to observations of wind galaxies in general [e.g. Veilleux et al., 2005, Sharp and Bland-Hawthorn, 2010], the steady thermally driven solutions which channel the energy efficiently into the wind and hence enable a comparatively calm disc also seem to be preferred.

Furthermore, in Section 6.6 we have seen that the bubble size matters during the phase where the wind is launched and breaching through the inner halo regions. In reality, bubbles will not be all of the same size but rather occur in a wide range from single, isolated SNe to a few hundred per bubble. Here, we show that the larger superbubbles matter the most for galactic winds. However, for more realistic event size distributions the mass and energy flux in the resulting wind might converge earlier and exhibit fewer and smaller peaks. For the time being, we will leave this matter open for future investigation.

The bubble size has turned out to be relevant firstly for the initial shock wave, and secondly in the steady wind phase. Larger bubbles give a more powerful rise to the wind, and will keep their strength at higher, roughly constant levels for a long time. In LBGs which presumably blow winds continuously at a steady level, the bubble size could be

important. Moreover, during the starburst phase, where the wind is often young and after which star formation will decrease rapidly, the bubble size might play a role.

The thermal halo pressure determines whether or not a stable wind phase develops in the first place. If the pressure is too high, the wind may very well be unable to proceed too far from the disc. How far it can go depends on the bubble size. Winds set up by small bubbles will stop early and in some cases collapse back onto the disc entirely, whereas winds resulting from large superbubbles have a good chance of escaping the halo no matter the halo pressure.

In observations of nearby galactic winds, one frequently finds energy efficiencies of order ten per cent [Veilleux et al., 2005]. We find much less in our simulations. A similar discrepancy is seen in the mass outflow rates. It is well possible that these are different classes of objects. If the high wind efficiencies would also be confirmed for LBGs, it might point to some effect we might still be missing in our simulations. A simplification that might turn out to be crucial could be the superbubble injection. We neglect the stellar winds of the massive stars, which are associated with star formation regions, and inject all the energy at once, whereas in a realistic star formation region, the energy injection is extended over many tens of Myr and a complex function of time [e.g. Voss et al., 2009]. This is clearly a non-negligible timescale in the context of a galactic wind.

Chapter 8

Conclusions and outlook

We have performed hydrodynamic simulations with the grid-based 3D code NIRVANA, setting up a disc-halo system close to hydrodynamic equilibrium. Star formation has been investigated in two different implementations: the first method makes use of a Jeans mass criterion and the local mass density, and the number of SNe per event is determined by cell mass, whereas the second is in agreement to a local Kennicutt-Schmidt law, and star formation is followed by a preset number of instantly occurring SNe. The feedback energy released this way eventually leads to a number of effects considered to play a role in the development of galactic winds.

Chapters 4 and 5 dealt with the circumstances under which it becomes possible to launch a powerful galactic wind at all, whereas in Chapter 6 a number of possible driving mechanism was investigated. In the first set of models we tested our local SN implementation in a galaxy comparable in mass to the Milky Way, but more gas-rich. We found that winds can emerge only in a narrow range of parameters for massive discs; further the reproduction of a multiphase ISM proved to play a significant role. We modified the local SN implementation in Chapter 5, and simultaneously decreased the disc mass to $10^9 M_{\odot}$ and altered the shape of the potential. Galactic winds proved to occur specifically in consequence to a strong clustering of SN events, and were often found to blow continuously. In Chapter 6 we studied the efficiency of various wind drivers, featuring a setup with a $10^{10} M_{\odot}$ disc and a genuine NFW potential. We concluded thermally pressurised bubbles to be the most important ingredient, whereas large bubbles have shown a trend to producing stronger winds than small ones. Buoyancy and kinetic energy provide some additional energy to the outflow, but are by far not as efficient as

thermal energy from SN feedback. We further believe the mass of the galactic disc to play a significant role. Setups including a disc of Milky Way-like mass do not exhibit continuous outflows due to the deep disc potential component, widely preventing filaments from escaping the disc. Discs of about $10^{10} M_{\odot}$ have a good chance of producing considerable supersonic outflows, whereas low-mass discs of $10^9 M_{\odot}$ can give rise to very strong winds, and might even be disrupted due to feedback.

Overall, our wind strengths for the medium-sized discs are rather on the low side, which might point to details of super-bubble physics not yet captured by our simulations. According to our findings however, LBGs of $10^9 - 10^{10} M_{\odot}$ could well be capable of blowing continuous winds over a few Gyr. Eventually, these discs become more massive due to accretion flows and the wind ceases when the disc potential becomes too deep, which may be the case in most of the SINS galaxies; if however the disc gas is widely depleted, like in the Milky Way, a wind can no longer be expected.

Future studies on this subject may include some modifications to the presented work. Since we know the wind to develop through superbubbles, it might prove important to modify their implementation further. In our superbubbles, the total SN energy was injected at one point in time. Instead, if the contributing SNe were triggered one by one, the bubble expansion rate may be altered to match the observations by Oey [2009]. This might lead to more continuous winds with less fluctuation in strength.

One major ingredient not included in this work would be magnetic fields. Since magnetic field lines are advected by gas entrained by the wind, they give an observational hint to the existence of outflowing gas, as mentioned in Section 4.4. Observations of magnetic fields would further allow us to infer the velocity of gaseous outflows in the halo. In addition, the new LOFAR radio telescope array may give information about synchrotron radiation in LBGs. This synchrotron radiation can e.g. be emitted by electrons in shock-heated material, and hence allows to draw conclusions about SN activity in the respective galaxy.

Appendix

9.1 Global setup conditions and implementations

We give an overview here about all simulations with their respective setup that have been performed in the context of this work. Table 9.1 contains the dark matter halo potential profiles, where “ $\propto \ln r$ ” is the logarithmic profile proposed by Flynn et al. [1996], “conv.” refers to our empirically determined profile resulting in a convergent baryonic halo matter density with radius r , and “NFW” is the well-known profile found by Navarro et al. [1996]. The disc parameters include its absolute and relative gas mass (where “gas fraction” means the relation from disc gas mass to total baryonic disc mass), and its cutoff radius r_{cut} . Finally, the star formation criteria that have been implemented in the respective run are shown.

Table 9.1: Global configurations used in all simulations presented in this work.

Run	DM Halo Profile	Disc parameters			SF criteria
		Gas mass	Gas fraction	r_{cut}	
F-ST	$\propto \ln r$	$6.0 \times 10^{10} M_{\odot}$	60%	10.0 kpc	Jeans mass/local density
F-KE	$\propto \ln r$	$6.0 \times 10^{10} M_{\odot}$	60%	10.0 kpc	Jeans mass/local density
Res12	conv.	$1.4 \times 10^9 M_{\odot}$	90%	3.3 kpc	Jeans mass/local density
Res16	conv.	$1.4 \times 10^9 M_{\odot}$	90%	3.3 kpc	Jeans mass/local density
Res30	conv.	$1.4 \times 10^9 M_{\odot}$	90%	3.3 kpc	Jeans mass/local density
Res33	conv.	$1.4 \times 10^9 M_{\odot}$	90%	3.3 kpc	Jeans mass/local density
Res36	conv.	$1.4 \times 10^9 M_{\odot}$	90%	3.3 kpc	Jeans mass/local density
Res65	conv.	$1.4 \times 10^9 M_{\odot}$	90%	3.3 kpc	Jeans mass/local density
CD-1	conv.	$1.4 \times 10^9 M_{\odot}$	90%	3.3 kpc	Jeans mass/local density
CD-1R	conv.	$1.4 \times 10^9 M_{\odot}$	90%	3.3 kpc	Jeans mass/local density
CD-3	conv.	$1.4 \times 10^9 M_{\odot}$	90%	3.3 kpc	Jeans mass/local density
CD-3R	conv.	$1.4 \times 10^9 M_{\odot}$	90%	3.3 kpc	Jeans mass/local density
CD-4	conv.	$1.4 \times 10^9 M_{\odot}$	90%	3.3 kpc	Jeans mass/local density
CD-4R	conv.	$1.4 \times 10^9 M_{\odot}$	90%	3.3 kpc	Jeans mass/local density
ED-3	conv.	$1.4 \times 10^9 M_{\odot}$	90%	3.3 kpc	Jeans mass/local density
ED-4	conv.	$1.4 \times 10^9 M_{\odot}$	90%	3.3 kpc	Jeans mass/local density
R16	NFW	$2.1 \times 10^{10} M_{\odot}$	50%	5.0 kpc	Kennicutt-Schmidt
R30	NFW	$2.1 \times 10^{10} M_{\odot}$	50%	5.0 kpc	Kennicutt-Schmidt
R33	NFW	$2.1 \times 10^{10} M_{\odot}$	50%	5.0 kpc	Kennicutt-Schmidt
R36	NFW	$2.1 \times 10^{10} M_{\odot}$	50%	5.0 kpc	Kennicutt-Schmidt
R65	NFW	$2.1 \times 10^{10} M_{\odot}$	50%	5.0 kpc	Kennicutt-Schmidt
ST20	NFW	$2.1 \times 10^{10} M_{\odot}$	50%	5.0 kpc	Kennicutt-Schmidt
ST50	NFW	$2.1 \times 10^{10} M_{\odot}$	50%	5.0 kpc	Kennicutt-Schmidt
ST100	NFW	$2.1 \times 10^{10} M_{\odot}$	50%	5.0 kpc	Kennicutt-Schmidt
ST200	NFW	$2.1 \times 10^{10} M_{\odot}$	50%	5.0 kpc	Kennicutt-Schmidt
KE0.4	NFW	$2.1 \times 10^{10} M_{\odot}$	50%	5.0 kpc	Kennicutt-Schmidt
TE0.6	NFW	$2.1 \times 10^{10} M_{\odot}$	50%	5.0 kpc	Kennicutt-Schmidt
TE0.4	NFW	$2.1 \times 10^{10} M_{\odot}$	50%	5.0 kpc	Kennicutt-Schmidt
B100	NFW	$2.1 \times 10^{10} M_{\odot}$	50%	5.0 kpc	Kennicutt-Schmidt
NC20	NFW	$2.1 \times 10^{10} M_{\odot}$	50%	5.0 kpc	Kennicutt-Schmidt
NC50	NFW	$2.1 \times 10^{10} M_{\odot}$	50%	5.0 kpc	Kennicutt-Schmidt
NC100	NFW	$2.1 \times 10^{10} M_{\odot}$	50%	5.0 kpc	Kennicutt-Schmidt
NC200	NFW	$2.1 \times 10^{10} M_{\odot}$	50%	5.0 kpc	Kennicutt-Schmidt

Bibliography

- K. L. Adelberger, C. C. Steidel, A. E. Shapley, and M. Pettini. Galaxies and Intergalactic Matter at Redshift $z \sim 3$: Overview. *ApJ*, 584:45–75, February 2003. doi: 10.1086/345660.
- G. J. Bendo, C. D. Wilson, B. E. Warren, E. Brinks, H. M. Butner, P. Chanial, D. L. Clements, S. Courteau, J. Irwin, F. P. Israel, J. H. Knapen, J. Leech, H. E. Matthews, S. Mühle, G. Petitpas, S. Serjeant, B. K. Tan, R. P. J. Tilanus, A. Usero, M. Vaccari, P. van der Werf, C. Vlahakis, T. Wiegert, and M. Zhu. The JCMT Nearby Galaxies Legacy Survey - III. Comparisons of cold dust, polycyclic aromatic hydrocarbons, molecular gas and atomic gas in NGC 2403. *MNRAS*, 402: 1409–1425, March 2010. doi: 10.1111/j.1365-2966.2009.16043.x.
- J. Binney and S. Tremaine. *Galactic dynamics*. Princeton, NJ, Princeton University Press, 1987, 747 p., 1987.
- F. Bournaud, E. Daddi, B. G. Elmegreen, D. M. Elmegreen, N. Nesvadba, E. Vanzella, P. Di Matteo, L. Le Tiran, M. Lehnert, and D. Elbaz. Observations and modeling of a clumpy galaxy at $z = 1.6$. Spectroscopic clues to the origin and evolution of chain galaxies. *A&A*, 486:741–753, August 2008. doi: 10.1051/0004-6361:20079250.
- A. Burkert. The turbulent interstellar medium. *Comptes Rendus Physique*, 7:433–441, April 2006. doi: 10.1016/j.crhy.2006.05.001.
- D. F. Cioffi, C. F. McKee, and E. Bertschinger. Dynamics of radiative supernova remnants. *ApJ*, 334: 252–265, November 1988. doi: 10.1086/166834.
- C. J. Conselice, J. S. Gallagher, III, and R. F. G. Wyse. On the Nature of the NGC 1275 System. *AJ*, 122:2281–2300, November 2001. doi: 10.1086/323534.
- J. L. Cooper, G. V. Bicknell, R. S. Sutherland, and J. Bland-Hawthorn. Three-Dimensional Simulations of a Starburst-driven Galactic Wind. *ApJ*, 674:157–171, February 2008. doi: 10.1086/524918.
- J. L. Cooper, G. V. Bicknell, R. S. Sutherland, and J. Bland-Hawthorn. Starburst-Driven Galactic Winds: Filament Formation and Emission Processes. *ApJ*, 703:330–347, September 2009. doi: 10.1088/0004-637X/703/1/330.
- R. I. Davies, F. Müller Sánchez, R. Genzel, L. J. Tacconi, E. K. S. Hicks, S. Friedrich, and A. Sternberg. A Close Look at Star Formation around Active Galactic Nuclei. *ApJ*, 671:1388–1412, December 2007. doi: 10.1086/523032.

- M. A. de Avillez and D. Breitschwerdt. Volume filling factors of the ISM phases in star forming galaxies. I. The role of the disk-halo interaction. *A&A*, 425:899–911, October 2004. doi: 10.1051/0004-6361:200400025.
- M. A. de Avillez and D. Breitschwerdt. Global dynamical evolution of the ISM in star forming galaxies. I. High resolution 3D simulations: Effect of the magnetic field. *A&A*, 436:585–600, June 2005. doi: 10.1051/0004-6361:20042146.
- S. Dib, E. Bell, and A. Burkert. The Supernova Rate-Velocity Dispersion Relation in the Interstellar Medium. *ApJ*, 638:797–810, February 2006. doi: 10.1086/498857.
- M. Dijkstra and A. Loeb. Acceleration of galactic supershells by Ly α radiation. *MNRAS*, 396:377–384, June 2009. doi: 10.1111/j.1365-2966.2009.14602.x.
- M. A. Dopita and R. S. Sutherland. *Astrophysics of the diffuse universe*. 2003.
- Y. Dubois and R. Teyssier. On the onset of galactic winds in quiescent star forming galaxies. *A&A*, 477:79–94, January 2008. doi: 10.1051/0004-6361:20078326.
- J. E. Dyson, S. A. E. G. Falle, and J. J. Perry. Intrinsic formation of narrow-line absorption systems in QSOs. I - The piston phase. *MNRAS*, 191:785–819, June 1980.
- A. C. Fabian, J. S. Sanders, G. B. Taylor, S. W. Allen, C. S. Crawford, R. M. Johnstone, and K. Iwasawa. A very deep Chandra observation of the Perseus cluster: shocks, ripples and conduction. *MNRAS*, 366:417–428, February 2006. doi: 10.1111/j.1365-2966.2005.09896.x.
- A. C. Fabian, R. M. Johnstone, J. S. Sanders, C. J. Conselice, C. S. Crawford, J. S. Gallagher, III, and E. Zweibel. Magnetic support of the optical emission line filaments in NGC 1275. *Nature*, 454:968–970, August 2008. doi: 10.1038/nature07169.
- A. Ferrara and M. Ricotti. Winds and infalling gas in Lyman break galaxies. *MNRAS*, 373:571–576, December 2006. doi: 10.1111/j.1365-2966.2006.10978.x.
- C. Flynn, J. Sommer-Larsen, and P. R. Christensen. Kinematics of the outer stellar halo. *MNRAS*, 281:1027–1032, August 1996.
- N. M. Förster Schreiber, R. Genzel, D. Lutz, and A. Sternberg. The Nature of Starburst Activity in M82. *ApJ*, 599:193–217, December 2003. doi: 10.1086/379097.
- M. Franx, G. D. Illingworth, D. D. Kelson, P. G. van Dokkum, and K.-V. Tran. A Pair of Lensed Galaxies at $z=4.92$ in the Field of CL 1358+62. *ApJ*, 486:L75+, September 1997. doi: 10.1086/310844.
- B. Frye, T. Broadhurst, and N. Benítez. Spectral Evidence for Widespread Galaxy Outflows at $z > 4$. *ApJ*, 568:558–575, April 2002. doi: 10.1086/338965.
- A. Fujita, C. L. Martin, M.-M. Mac Low, K. C. B. New, and R. Weaver. The Origin and Kinematics of Cold Gas in Galactic Winds: Insight from Numerical Simulations. *ApJ*, 698:693–714, June 2009. doi: 10.1088/0004-637X/698/1/693.

- V. Gaibler, M. Camenzind, and M. Krause. Evolution of the ISM and Galactic Activity. *ArXiv Astrophysics e-prints*, February 2005.
- R. Genzel, A. Burkert, N. Bouché, G. Cresci, N. M. Förster Schreiber, A. Shapley, K. Shapiro, L. J. Tacconi, P. Buschkamp, A. Cimatti, E. Daddi, R. Davies, F. Eisenhauer, D. K. Erb, S. Genel, O. Gerhard, E. Hicks, D. Lutz, T. Naab, T. Ott, S. Rabien, A. Renzini, C. C. Steidel, A. Sternberg, and S. J. Lilly. From Rings to Bulges: Evidence for Rapid Secular Galaxy Evolution at $z \sim 2$ from Integral Field Spectroscopy in the SINS Survey. *ApJ*, 687:59–77, November 2008. doi: 10.1086/591840.
- N. Y. Gnedin. Metal enrichment of the intergalactic medium. *MNRAS*, 294:407–+, March 1998. doi: 10.1046/j.1365-8711.1998.01156.x.
- P. Goldreich and D. Lynden-Bell. I. Gravitational stability of uniformly rotating disks. *MNRAS*, 130: 97, 1965.
- E. Hayashi, J. F. Navarro, and V. Springel. The shape of the gravitational potential in cold dark matter haloes. *MNRAS*, 377:50–62, May 2007. doi: 10.1111/j.1365-2966.2007.11599.x.
- T. M. Heckman, C. Robert, C. Leitherer, D. R. Garnett, and F. van der Rydt. The Ultraviolet Spectroscopic Properties of Local Starbursts: Implications at High Redshift. *ApJ*, 503:646–+, August 1998. doi: 10.1086/306035.
- T. M. Heckman, M. D. Lehnert, D. K. Strickland, and L. Armus. Absorption-Line Probes of Gas and Dust in Galactic Superwinds. *ApJS*, 129:493–516, August 2000. doi: 10.1086/313421.
- L. Hernquist. An analytical model for spherical galaxies and bulges. *ApJ*, 356:359–364, June 1990. doi: 10.1086/168845.
- J. H. Jeans. The Stability of a Spherical Nebula. *Royal Society of London Philosophical Transactions Series A*, 199:1–53, 1902. doi: 10.1098/rsta.1902.0012.
- V. Junk, S. Walch, F. Heitsch, A. Burkert, M. Wetzstein, M. Schartmann, and D. Price. Modelling shear flows with smoothed particle hydrodynamics and grid-based methods. *MNRAS*, 407:1933–1945, September 2010. doi: 10.1111/j.1365-2966.2010.17039.x.
- S. A. Kassin, B. J. Weiner, S. M. Faber, D. C. Koo, J. M. Lotz, J. Diemand, J. J. Harker, K. Bundy, A. J. Metevier, A. C. Phillips, M. C. Cooper, D. J. Croton, N. Konidaris, K. G. Noeske, and C. N. A. Willmer. The Stellar Mass Tully-Fisher Relation to $z = 1.2$ from AEGIS. *ApJ*, 660:L35–L38, May 2007. doi: 10.1086/517932.
- R. C. Kennicutt, Jr. The Global Schmidt Law in Star-forming Galaxies. *ApJ*, 498:541–+, May 1998. doi: 10.1086/305588.
- M. Krause. Galactic wind shells and high redshift radio galaxies. On the nature of associated absorbers. *A&A*, 436:845–851, June 2005. doi: 10.1051/0004-6361:20042450.
- A. Kritsuk, T. Plewa, and E. Müller. Convective cores in galactic cooling flows. *MNRAS*, 326:11–22, September 2001. doi: 10.1046/j.1365-8711.2001.04610.x.

- L. D. Landau and E. M. Lifshitz. *Fluid mechanics*. 1959.
- D. R. Law, C. C. Steidel, D. K. Erb, J. E. Larkin, M. Pettini, A. E. Shapley, and S. A. Wright. Integral Field Spectroscopy of High-Redshift Star-forming Galaxies with Laser-guided Adaptive Optics: Evidence for Dispersion-dominated Kinematics. *ApJ*, 669:929–946, November 2007. doi: 10.1086/521786.
- J. D. Lowenthal, D. C. Koo, R. Guzman, J. Gallego, A. C. Phillips, S. M. Faber, N. P. Vogt, G. D. Illingworth, and C. Gronwall. Keck Spectroscopy of Redshift Z approximately 3 Galaxies in the Hubble Deep Field. *ApJ*, 481:673–+, May 1997. doi: 10.1086/304092.
- M.-M. Mac Low, R. S. Klessen, A. Burkert, and M. D. Smith. Kinetic Energy Decay Rates of Supersonic and Super-Alfvénic Turbulence in Star-Forming Clouds. *Physical Review Letters*, 80:2754–2757, March 1998. doi: 10.1103/PhysRevLett.80.2754.
- S. A. Mao, B. M. Gaensler, M. Haverkorn, E. G. Zweibel, G. J. Madsen, N. M. McClure-Griffiths, A. Shukurov, and P. P. Kronberg. A Survey of Extragalactic Faraday Rotation at High Galactic Latitude: The Vertical Magnetic Field of the Milky Way Toward the Galactic Poles. *ApJ*, 714: 1170–1186, May 2010. doi: 10.1088/0004-637X/714/2/1170.
- C. L. Martin. Mapping Large-Scale Gaseous Outflows in Ultraluminous Galaxies with Keck II ESI Spectra: Variations in Outflow Velocity with Galactic Mass. *ApJ*, 621:227–245, March 2005. doi: 10.1086/427277.
- M. Miyamoto and R. Nagai. Three-dimensional models for the distribution of mass in galaxies. *PASJ*, 27:533–543, 1975.
- B. B. Nath and J. Silk. Starburst-driven galactic outflows. *MNRAS*, 396:L90–L94, June 2009. doi: 10.1111/j.1745-3933.2009.00670.x.
- B. B. Nath and N. Trentham. On the enrichment of the intergalactic medium by galactic winds. *MNRAS*, 291:505–+, November 1997.
- J. F. Navarro, C. S. Frenk, and S. D. M. White. The Structure of Cold Dark Matter Halos. *ApJ*, 462: 563–+, May 1996. doi: 10.1086/177173.
- M. S. Oey. The Power Problem in Superbubbles. In R. K. Smith, S. L. Snowden, & K. D. Kuntz, editor, *American Institute of Physics Conference Series*, volume 1156 of *American Institute of Physics Conference Series*, pages 295–304, August 2009. doi: 10.1063/1.3211829.
- Y. Ohta, I. Kayo, and A. Taruya. Evolution of the Cosmological Density Distribution Function from the Local Collapse Model. *ApJ*, 589:1–16, May 2003. doi: 10.1086/374375.
- Y. Ohya, Y. Taniguchi, K. S. Kawabata, Y. Shioya, T. Murayama, T. Nagao, T. Takata, M. Iye, and M. Yoshida. On the Origin of Ly α Blobs at High Redshift: Kinematic Evidence of a Hyperwind Galaxy at $z = 3.1$. *ApJ*, 591:L9–L12, July 2003. doi: 10.1086/376959.

- M. Pettini, C. C. Steidel, K. L. Adelberger, M. Dickinson, and M. Giavalisco. The Ultraviolet Spectrum of MS 1512-CB58: An Insight into Lyman-Break Galaxies. *ApJ*, 528:96–107, January 2000. doi: 10.1086/308176.
- M. Pettini, A. E. Shapley, C. C. Steidel, J.-G. Cuby, M. Dickinson, A. F. M. Moorwood, K. L. Adelberger, and M. Giavalisco. The Rest-Frame Optical Spectra of Lyman Break Galaxies: Star Formation, Extinction, Abundances, and Kinematics. *ApJ*, 554:981–1000, June 2001. doi: 10.1086/321403.
- M. Pettini, S. A. Rix, C. C. Steidel, K. L. Adelberger, M. P. Hunt, and A. E. Shapley. New Observations of the Interstellar Medium in the Lyman Break Galaxy MS 1512-cB58. *ApJ*, 569:742–757, April 2002. doi: 10.1086/339355.
- L. C. Powell, A. Slyz, and J. Devriendt. The impact of supernova-driven winds on stream-fed proto-galaxies. *MNRAS*, 414:3671–3689, July 2011. doi: 10.1111/j.1365-2966.2011.18668.x.
- Y. Rasera and R. Teyssier. The history of the baryon budget. Cosmic logistics in a hierarchical universe. *A&A*, 445:1–27, January 2006. doi: 10.1051/0004-6361:20053116.
- A. O. Razoumov. Damped Ly α Absorber Kinematics and Outflows from Starburst Galaxies. *ApJ*, 707:738–749, December 2009. doi: 10.1088/0004-637X/707/1/738.
- D. S. Rupke, S. Veilleux, and D. B. Sanders. Keck Absorption-Line Spectroscopy of Galactic Winds in Ultraluminous Infrared Galaxies. *ApJ*, 570:588–609, May 2002. doi: 10.1086/339789.
- D. S. Rupke, S. Veilleux, and D. B. Sanders. Outflows in Infrared-Luminous Starbursts at $z < 0.5$. II. Analysis and Discussion. *ApJS*, 160:115–148, September 2005. doi: 10.1086/432889.
- E. Scannapieco and M. Brüggén. Simulating supersonic turbulence in galaxy outflows. *MNRAS*, 405:1634–1653, July 2010. doi: 10.1111/j.1365-2966.2010.16599.x.
- K. L. Shapiro, R. Genzel, E. Quataert, N. M. Förster Schreiber, R. Davies, L. Tacconi, L. Armus, N. Bouché, P. Buschkamp, A. Cimatti, G. Cresci, E. Daddi, F. Eisenhauer, D. K. Erb, S. Genel, E. K. S. Hicks, S. J. Lilly, D. Lutz, A. Renzini, A. Shapley, C. C. Steidel, and A. Sternberg. The SINS Survey: Broad Emission Lines in High-Redshift Star-Forming Galaxies. *ApJ*, 701:955–963, August 2009. doi: 10.1088/0004-637X/701/2/955.
- A. E. Shapley, C. C. Steidel, M. Pettini, and K. L. Adelberger. Rest-Frame Ultraviolet Spectra of $z \sim 3$ Lyman Break Galaxies. *ApJ*, 588:65–89, May 2003. doi: 10.1086/373922.
- R. G. Sharp and J. Bland-Hawthorn. Three-Dimensional Integral Field Observations of 10 Galactic Winds. I. Extended Phase (gsim10 Myr) of Mass/Energy Injection Before the Wind Blows. *ApJ*, 711:818–852, March 2010. doi: 10.1088/0004-637X/711/2/818.
- I. Smail, S. C. Chapman, R. J. Ivison, A. W. Blain, T. Takata, T. M. Heckman, J. S. Dunlop, and K. Sekiguchi. A vigorous starburst in the SCUBA galaxy N2 850.4. *MNRAS*, 342:1185–1193, July 2003. doi: 10.1046/j.1365-8711.2003.06621.x.

- V. Springel and L. Hernquist. Cosmological smoothed particle hydrodynamics simulations: a hybrid multiphase model for star formation. *MNRAS*, 339:289–311, February 2003. doi: 10.1046/j.1365-8711.2003.06206.x.
- S. W. Stahler and F. Palla. *The Formation of Stars*. The Formation of Stars, by Steven W. Stahler, Francesco Palla, pp. 865. ISBN 3-527-40559-3. Wiley-VCH, January 2005., January 2005.
- C. C. Steidel, K. L. Adelberger, A. E. Shapley, M. Pettini, M. Dickinson, and M. Giavalisco. Lyman Break Galaxies at Redshift $z \sim 3$: Survey Description and Full Data Set. *ApJ*, 592:728–754, August 2003. doi: 10.1086/375772.
- J. Stil, N. Wityk, R. Ouyed, and A. R. Taylor. Three-dimensional Simulations of Magnetized Superbubbles: New Insights into the Importance of MHD Effects on Observed Quantities. *ApJ*, 701:330–347, August 2009. doi: 10.1088/0004-637X/701/1/330.
- G. Stinson, A. Seth, N. Katz, J. Wadsley, F. Governato, and T. Quinn. Star formation and feedback in smoothed particle hydrodynamic simulations - I. Isolated galaxies. *MNRAS*, 373:1074–1090, December 2006. doi: 10.1111/j.1365-2966.2006.11097.x.
- D. K. Strickland and I. R. Stevens. Starburst-driven galactic winds - I. Energetics and intrinsic X-ray emission. *MNRAS*, 314:511–545, May 2000. doi: 10.1046/j.1365-8711.2000.03391.x.
- R. S. Sutherland and M. A. Dopita. Cooling functions for low-density astrophysical plasmas. *ApJS*, 88:253–327, September 1993. doi: 10.1086/191823.
- A. M. Swinbank, I. Smail, R. G. Bower, C. Borys, S. C. Chapman, A. W. Blain, R. J. Ivison, S. R. Howat, W. C. Keel, and A. J. Bunker. Optical and near-infrared integral field spectroscopy of the SCUBA galaxy N2 850.4. *MNRAS*, 359:401–407, May 2005. doi: 10.1111/j.1365-2966.2005.08901.x.
- M. Tegmark, J. Silk, and A. Evrard. Late Reionization by Supernova-driven Winds. *ApJ*, 417:54–+, November 1993. doi: 10.1086/173290.
- A. Toomre. On the gravitational stability of a disk of stars. *ApJ*, 139:1217–1238, May 1964.
- R. van Ojik, H. J. A. Roettgering, G. K. Miley, and R. W. Hunstead. The gaseous environments of radio galaxies in the early Universe: kinematics of the Lyman α emission and spatially resolved H I absorption. *A&A*, 317:358–384, January 1997.
- L. van Starckenburg, P. P. van der Werf, M. Franx, I. Labbé, G. Rudnick, and S. Wuyts. Dynamical properties of a large young disk galaxy at $z = 2.03$. *A&A*, 488:99–112, September 2008. doi: 10.1051/0004-6361:200809632.
- S. Veilleux, G. Cecil, and J. Bland-Hawthorn. Galactic Winds. *ARA&A*, 43:769–826, September 2005. doi: 10.1146/annurev.astro.43.072103.150610.
- R. Voss, R. Diehl, D. H. Hartmann, M. Cerviño, J. S. Vink, G. Meynet, M. Limongi, and A. Chieffi. Using population synthesis of massive stars to study the interstellar medium near OB associations. *A&A*, 504:531–542, September 2009. doi: 10.1051/0004-6361/200912260.

-
- K. Wada and C. A. Norman. Density Structure of the Interstellar Medium and the Star Formation Rate in Galactic Disks. *ApJ*, 660:276–287, May 2007. doi: 10.1086/513002.
- R. Weaver, R. McCray, J. Castor, P. Shapiro, and R. Moore. Interstellar bubbles. II - Structure and evolution. *ApJ*, 218:377–395, December 1977. doi: 10.1086/155692.
- R. J. Wilman, M. J. Jarvis, H. J. A. Röttgering, and L. Binette. HI in the protocluster environment at $z > 2$: absorbing haloes and the Ly α forest. *MNRAS*, 351:1109–1119, July 2004. doi: 10.1111/j.1365-2966.2004.07857.x.
- R. Wunsch, S. Silich, J. Palouš, G. Tenorio-Tagle, and C. Muñoz-Tuñón. Evolution of Super Star Cluster Winds with Strong Cooling. *ApJ*, 740:75, October 2011. doi: 10.1088/0004-637X/740/2/75.
- D. H. Zhao, Y. P. Jing, H. J. Mo, and G. Börner. Accurate Universal Models for the Mass Accretion Histories and Concentrations of Dark Matter Halos. *ApJ*, 707:354–369, December 2009. doi: 10.1088/0004-637X/707/1/354.
- U. Ziegler and H. W. Yorke. A nested grid refinement technique for magnetohydrodynamical flows. *Computer Physics Communications*, 101:54–74, April 1997. doi: 10.1016/S0010-4655(96)00163-4.

Acknowledgement

First of all I would like to thank Martin Krause; this thesis would not have been possible without his excellent guidance and supervision. His skills to encourage me to work on this challenging but nevertheless interesting topic are remarkable and proved invaluable to me. I also would like to express many thanks to the head of the CAST group, Andreas Burkert, whose help has been especially important in the last phase of my studies, and who suggested several issues to perfect the project. I owe a special debt of gratitude to Jesper Sommer-Larsen, who was leading in the setup of this PhD project, for giving me feedback and inspiration especially during the first phase of my thesis.

Further thanks goes to the Excellence Cluster Universe and the German Research Community (DFG) for continuous funding throughout the largest part of the project. I would also like to thank my friends and colleagues from the CAST group for the friendly atmosphere and regular meetings. I am furthermore grateful to Barbara Ercolano, Mark Westmoquette, Ralf-Jürgen Dettmar, Christian Tapken and Matthew Lehnert for helpful comments and fruitful discussions.

My cordial thanks finally goes to my family, friends, and my dear colleague and girlfriend Stephanie Pekruhl, who supported me through all the time, especially during the last year, which imposed some hard strokes of fate on me.

Declaration

I herewith declare that I prepared this PhD thesis independently. Except for the sources listed in the bibliography no further media have been used.

Munich, May 21st, 2012